이학박사학위논문

Cloud and Precipitation Studies using Disdrometer Observations and Models

우적계 관측과 모델을 이용한 구름 및 강수 연구

2023년 8월

서울대학교 대학원

지구환경과학부

이 주 현

Cloud and Precipitation Studies using Disdrometer Observations and Models

우적계 관측과 모델을 이용한 구름 및 강수 연구

지도교수 백 종 진

이 논문을 이학박사 학위논문으로 제출함

2023년 5월

서울대학교 대학원

지구환경과학부

이 주 현

이주현의 박사학위논문을 인준함

2023년 7월

위 원 장	박 성 수	(인)
부위원장	백 종 진	(인)
위 원	박 영 산	(인)
위 원	배 수 야	(인)
위 원	이 현 호	(인)

Cloud and Precipitation Studies using Disdrometer Observations and Models

By

Joohyun Lee

A Dissertation Submitted to the Faculty of the Graduate School of Seoul National University in Partial Fulfillment of the Requirements for the Degree of Doctor of Philosophy

August 2023

Advisory Committee:

Professor Sungsu Park, Chair

Professor Jong-Jin Baik, Advisor

Doctor Young-San Park

Doctor Soo Ya Bae

Professor Hyunho Lee

Abstract

The regional differences in the characteristics of raindrop size distribution (RSD) among three cities (Seoul, Chuncheon, and Jincheon) in South Korea are examined using disdrometer data for the period from 25 July 2018 to 31 July 2021 and their possible causes are investigated. Jincheon, the least populated and southernmost city among the three cities, is characterized by the smallest mean rainfall intensity and a relatively high frequency of light rain. These precipitation characteristics are related to the mass-weighted mean diameter D_m that is smallest and the logarithm of generalized intercept parameter $\log_{10}N_w$ that is largest in this city. In contrast, Chuncheon, a medium-sized city located in a basin, is characterized by the largest mean rainfall intensity and a relatively high frequency of heavy rain, which is related to the largest D_m and smallest $\log_{10}N_w$. Relatively small (large) convective available potential energy, low (high) cloud top, and high (low) cloud base in Jincheon (Chuncheon) can be responsible for the contrasts in RSD characteristics between the two cities. Seoul, the most populated city, is characterized by the intermediate mean rainfall intensity related to the intermediate D_m and $\log_{10}N_w$ between those in Jincheon and Chuncheon. Seoul exhibits the most frequent occurrence of extreme rainfall events and relatively large D_m for very heavy rain, which can be associated with the most

frequent occurrence of large convective available potential energy.

The raindrop size distribution observed from ground-based or airborne disdrometers has been widely used to understand the characteristics of clouds and precipitation. However, its variability needs to be studied further and properly considered for improving precipitation prediction. In this study, using disdrometer data, the diagnostic relations for the intercept parameter of the exponential raindrop size distribution N_0 are derived for different rain types and the impacts of the diagnostic relations on precipitation prediction are examined. The disdrometer data observed at four sites in South Korea show spatiotemporal variations of N_0. Three different derivation methods proposed by previous studies are used to derive the diagnostic relations, and the diagnostic relation that best reproduces the observed N_0 is selected. The diagnostic relation is implemented into the WRF single-moment 6-class microphysics (WSM6) scheme, and its impacts are investigated through the simulations of summertime precipitation events in South Korea. Compared to the simulation using the original WSM6 scheme (WSM6-O) where a constant N_0 is used, the simulation where N_0 is diagnosed by the diagnostic relation using the rainwater content at the lowest level (WSM6-L) yields better precipitation prediction. The WSM6-L simulation represents the variability of N_0. Also, the WSM6-L simulation predicts N_0 that is on average smaller than the prescribed value in the WSM6-O simulation, agreeing with the observation to some extent. The smaller N_0 in the WSM6-L simulation decreases the rainwater production by the accretion of cloud water and the melting of ice hydrometeors, decreasing the rainwater mixing ratio.

Bin microphysics schemes prognose the RSD which can be directly evaluated through comparison with disdrometer observations. This evaluation will provide implications on the reliability of simulated cloud microphysics by bin microphysics schemes. In this study, the RSDs of a precipitation event associated with an extratropical cyclone passing South Korea are simulated using a bin microphysics scheme and compared with those observed by a ground-based disdrometer. The simulated mean RSD overall agrees with the observation, particularly well in the intermediate-diameter range. Notable overestimations appear in the large- and small-diameter ranges, which respectively stem from the biases in two different time periods, one dominated by stratiform rain and the other largely involved with convective rain. In the stratiform-rain dominated period, the melting of snow is the largest contributor to RSDs. The overestimation in the large-diameter range in this period can be associated with overly active ice–ice collection at upper levels, which generates a local maximum in RSD at the diameter of 3.3 mm that is not seen in the observed RSDs. In the convective-rain involved period, the warm-rain collision–coalescence is the largest contributor to RSDs. The overestimation in the small-diameter range and underestimation in the large-diameter range imply that the collisional growth of raindrops is represented to be weaker than that in reality. The findings in this study suggest that the RSDs simulated using a bin microphysics scheme can have some systematic biases that are originated from misrepresentation of some microphysical processes.

The impacts of aerosols on precipitation and RSD in an extratropical cyclone are examined for the two different rain types (stratiform and convective rain). Five simulations with different initial aerosol number concentrations (N_a = 100, 900, 2700, 8100, and 24300 cm^{-3}) are considered. In both stratiform and convective rain, an increase in N_a enhances the nucleation process, resulting in an increase of the number of cloud droplets and a decrease of the mean size of cloud droplets. This leads to the enhancement of accretion, riming, and condensation rates. For convective rain, the enhanced condensation with increasing N_a induces stronger updrafts through the increased latent heat release and depletes more water vapor in the lower levels, making the upper level drier. Due to the drier upper level, Wegener-Bergeron-Findeisen process is more active. Despite the active ice-related microphysical processes, their contribution to precipitation is

relatively weak due to the small melting rates. The more active accretion and riming processes in convective rain result in the increase of rain rate and the increase of raindrop number concentration in the intermediate diameter range. For stratiform rain, melting rates are comparable to those of accretion and riming. This may be due to the substantial amount of snow advected from the convective rain area. The more active melting process in stratiform rain results in the increase of rain rate, together with active accretion and riming processes, and the increase of raindrop number concentration in the large diameter range.

Keywords: raindrop size distribution, disdrometer, bulk microphysics scheme, bin microphysics scheme, precipitation, aerosol-cloud-precipitation interactions

Student Number: 2017-20135

Contents

List of Figures

List of Tables

1 Overview

The raindrop size distribution (RSD) is a valuable piece of information that can help us to understand the microphysical processes related to precipitation, quantitatively estimate precipitation amounts, and improve the precipitation prediction in numerical models. Therefore, understanding the RSD characteristics and representing them well in cloud microphysical parameterization are important in the improvement of precipitation prediction. The method to represent the RSD characteristics in cloud microphysics scheme differs depending on the assumption about RSD. In the bulk microphysics schemes, which assume the RSD to follow a specific distribution such as the exponential, gamma, or lognormal distribution, the variability of RSD characteristics is reflected by how the parameters of the assumed distribution are treated. If we can introduce more flexibility to the parameters, more realistic precipitation prediction can be expected. Unlike the bulk microphysics schemes, the bin microphysics schemes explicitly predict the RSD without making assumptions about the distribution. Because of these characteristics, evaluation of the simulated RSD can provide more insight to the deficiencies in cloud microphysical parameterizations within the numerical model. Examining and understanding these deficiencies can help to improve the precipitation prediction.

Using the disdrometer data observed in three cities in South Korea, the regional differences in the characteristics of RSD are examined in Chapter 2. It is expected that three cities will exhibit different RSD characteristics due to their different environmental conditions despite close proximity to each other. This investigation on the regional differences in RSD characteristics is expected to reveal how significant the RSD variability is among the three cities and which environmental conditions make differences in RSD characteristics.

To reflect the variabilities in RSD characteristics, the diagnostic relations for different rain types are derived and implemented in the single-moment bulk microphysics scheme in Chapter 3. To select the best diagnostic relations for the intercept parameter of the exponential distribution, three derivation methods in previous studies with and without the rain-type classification are evaluated. Then, the impacts of the diagnostic relations on the cloud and precipitation are investigated through the real case simulations of summer precipitation in South Korea.

In Chapter 4, the RSD simulated in the bin microphysics scheme is evaluated by the disdrometer observation. The case for an extratropical cyclone that passed the South Korea is simulated and evaluated to examine whether the bin microphysics scheme can reproduce the RSD variations from different types of clouds and precipitation in this case. Then, the possible sources for the biases revealed in the evaluation are speculated.

In Chapter 5, using the same case and simulation setup in Chapter 4 except for the initial aerosol number concentration, the impacts of aerosols on precipitation and raindrop size distribution are examined. Considering the diverse cloud types in an extratropical cyclone, the impacts of aerosols are investigated depending on the rain type. In addition, it is examined whether the changes in the initial aerosol number concentration can reduce the biases appeared in the evaluation in Chapter 4.

2 Regional differences in raindrop size distribution observed from disdrometers in South Korea and their possible causes

2.1 Introduction

The measurement and analysis of raindrop size distribution (RSD) are important part of cloud physics, and extensive studies have been performed to characterize RSD using disdrometer observations in many regions of the world (Nzeukou et al. 2004; Leinonen et al. 2012; Giangrande et al. 2014; Murata et al. 2020; Zea et al. 2021). Characterizing RSD can greatly help to improve our understanding of cloud and precipitation processes, estimate rainfall, and parameterize cloud microphysical processes in numerical models.

Many studies have shown that there is strong regional variability in RSD characteristics (Bringi et al. 2003; Seela et al. 2017; Dolan et al. 2018). Bringi et al. (2003) collected disdrometer and radar data from regions of various climate regimes, that is, near equator, tropics, subtropics, continental, oceanic, and High Plains, and classified the data into stratiform and convective rain using the rain rate and its standard deviation. The RSD data in each of the regions constitutes a cluster in the RSD-parameter space, which results in the identification of three distinct clusters (stratiform rain, maritime-like convective rain, and continental-like convective rain). Dolan et al. (2018) collected disdrometer data from three latitude bands (lower than 23°, 23°–45°, and higher than 45° in both hemispheres) and performed the principal component analysis. They identified six groups in the space of the logarithm of generalized intercept parameter and the median volume diameter and showed that each group is associated with specific cloud microphysical processes and that the process which is responsible for the RSD depends on the latitude band. Seela et al. (2017) compared the characteristics in RSD between two islands in western Pacific (Palau and Taiwan). The mass-weighted mean diameter (generalized intercept parameter) is larger (smaller) in Taiwan than in Palau. They suggested that this is linked to the relatively strong convective activity, high storm height, high bright band, and high aerosol concentration in Taiwan.

The regional variability in RSD characteristics has been examined also for smaller spatial scales (Loh et al. 2019; Han et al. 2021; Suh et al. 2021). Han et al. (2021) investigated the regional variability of summertime RSD obtained from ten disdrometers in Beijing. The minimum mass-weighted mean diameter and maximum generalized intercept parameter appear in the city center. They speculated that this is related to the urban heat island and aerosol effects. South Korea, located in a peninsula with complex geographical features, shows a regional variability of RSD characteristics within the country. Loh et al. (2019) compared the RSD characteristics between two sites, one in the central region and the other in the southeastern region of South Korea, and showed that the site in the central region tends to receive a relatively large number of small-sized raindrops. Suh et al. (2021) examined how the RSD characteristics change from coastal areas to inland areas in the southern region of South Korea and showed that the coastal areas exhibit multimodal distributions of probability density functions of the mass-weighted mean diameter and logarithm of generalized intercept parameter for stratiform rain while the inland areas do not. They also showed that for convective rain, the RSD parameters have linear relationships with the distance from the coastline.

The studies on disdrometer observation in South Korea has been limited to the southern and central parts of South Korea (Lim et al. 2015; You and Lee 2015; Suh et al. 2016, 2021; Bang et al. 2017; Kim et al. 2019; Loh et al. 2019). Although there is a study in the northwestern part of South Korea (Jwa et al. 2021), about one year of observational period in that study is rather short. This study uses the disdrometer data observed for about three years at Seoul, Chuncheon, and Jincheon, which are at the northwestern, northern, and central parts of South Korea, respectively. From this study, it can be expected to reveal the RSD characteristics of northern part in South Korea. In addition, the direct comparison between Seoul, which is the largest metropolis in South Korea, and other sites will be of great help in understanding how the RSD characteristics of urban areas with different sizes differ.

In this study, we examine the regional differences in RSD characteristics among three different sites in South Korea using disdrometer data and investigate possible causes for the differences. In subchapter 2.2, the data and methodology are given. In subchapter 2.3, the precipitation and RSD characteristics of each of the three sites are characterized and compared. Also, the regional differences in thermodynamic and cloud characteristics that may cause the regional differences in RSD characteristics are investigated. A summary and conclusions are given in Chapter 6.

2.2 Data and methodology

2.2.1 Disdrometer data and RSD parameters

In this study, data from Parsivel^2 disdrometers (Tokay et al. 2014) installed at three different sites (Seoul, Chuncheon, and Jincheon) in South Korea are used to investigate the regional variations in RSD parameters. Figure 2.1 shows the geographical locations of the disdrometers. Seoul is the most populated city in South Korea and manifests the most urban

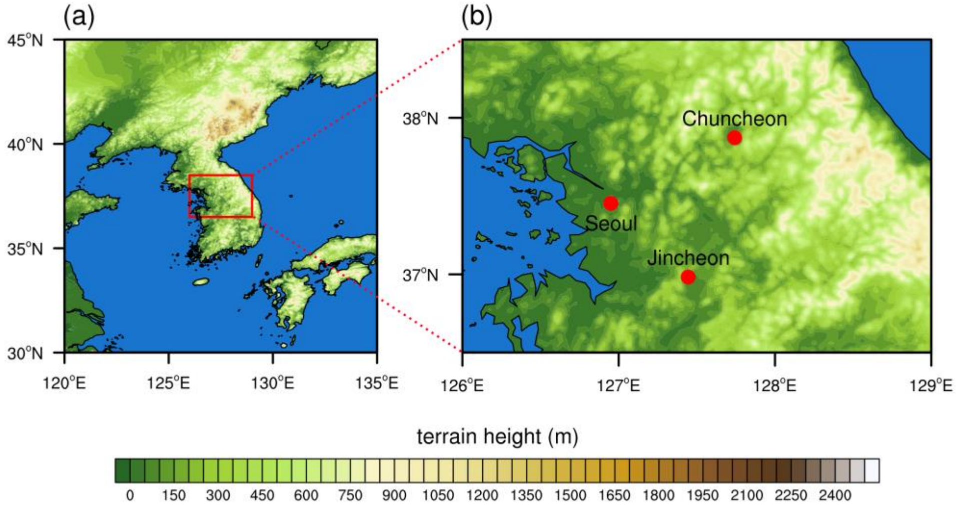

Figure 2.1 (a) Topographic map of South Korea and its surrounding regions and (b) zoomed area with locations of the three disdrometers (red circles).

characteristics among the three sites. Chuncheon is a medium-sized city that is located in a basin and most distant from the coast and thus highly likely to have the continental and orographic characteristics among the three sites. Jincheon is a small city and located at the southernmost latitude among the three cities. The elevations of the three disdrometer sites are similar to each other, which are 142, 136, and 138 m for Seoul, Chuncheon, and Jincheon, respectively.

The Parsivel^2 disdrometer is an optical disdrometer having a transmitter and a receiver of a laser beam of 650-nm wavelength. The sampling volume between them is 5400 mm^3 (180 mm × 30 mm × 1 mm). When a precipitating particle falls through the sampling volume, the diameter and fall velocity of the particle are determined by the maximum reduced voltage and the signal duration, respectively. The determined diameter and fall velocity are classified into 32 × 32 non-uniform bins. The range of particle diameter is 0–26 mm with 32 bins, but the first two bins are not considered due to the low signal-to-noise ratio. For liquid precipitation, which is the main concern of this study, the range is confined to 0.25–8 mm. The range of fall velocity is 0–22.4 m s^{-1} with 32 bins. The sampling interval is 1 min.

Optical disdrometers measure drop size and fall velocity without influencing drop behavior during measurement, significantly reducing measurement errors from drop breakup and splattering, which is a great advantage over impact disdrometers (Kathiravelu et al. 2016). However, there still exist several known measurement error sources for the Parsivel2 disdrometer, such as the effects of strong winds, drops partially passing through the sampling volume, drops splashing on impact with the instrument, multiple drops simultaneously passing through the sampling volume (Angulo-Martínez et al. 2018). Concerning these error sources, the data of drops that fall too fast or too slowly for their sizes (drops with fall velocities 60% larger than or 60% smaller than those from the fall velocity–diameter relationship of Atlas et al. (1973)) are excluded, which is similar to the quality control method of Jaffrain and Berne (2011). In addition, following Thompson et al. (2015), the 1-min disdrometer data with rain rate smaller than 0.05 mm h^{-1} or with total drop counts less than 100 are excluded, and the remaining data are used for analysis if they exist consecutively for three or more minutes.

The observational period is about three years from 25 July 2018 to 31 July 2021. The dates when data from any of the three sites are missing are excluded. As a result, the number of 1-min disdrometer data is 53,340 for Seoul, 52,787 for Chuncheon, and 65,405 for Jincheon.

Each 1-min disdrometer data has the information of the number of raindrops in each diameter and fall velocity bin. From the data, the number concentration of raindrops per unit volume per unit size interval in the *i*th diameter bin $N(D_i)$ (m^{-3} mm^{-1}) is calculated as

$$N(D_i) = \sum_{j=1}^{32} \frac{n_{ij}}{A_i V_j \Delta t \Delta D_i}, \tag{2.1}$$

where n_{ij} is the number of raindrops in the ith diameter and jth fall velocity bin, A_i (m^2) is the effective sampling area for the ith diameter bin, V_j (m s^{-1}) is the fall velocity for the jth fall velocity bin, Δt (s) is the sampling interval, and ΔD_i (mm) is the size interval of the ith diameter bin (here, D_i is the mid-value of the ith diameter bin).

Many RSD parameters can be calculated using $N(D_i)$. The nth-order moment of RSD M_n is defined by

$$M_n = \int D^n N(D) dD. \tag{2.2}$$

For the disdrometer data, Eq. (2.2) is rewritten as

$$M_n = \sum_{i=3}^{23} D_i^n N(D_i) \Delta D_i. \tag{2.3}$$

The first two bins (i = 1, 2) and last nine bins (i = 24–32) are not considered due to the low signal-to-noise ratio and the consideration of liquid precipitation only, respectively. The total number concentration N_t (m^{-3}), rainwater content W (g m^{-3}), and radar reflectivity Z (mm^6 mm^{-3}) are expressed using the moments of RSD as

$$N_t = M_0, \tag{2.4}$$

$$W = \frac{10^{-3}\pi}{6}\rho_w M_3, \tag{2.5}$$

$$Z = M_6, \tag{2.6}$$

where ρ_w (g cm^{-3}) is the liquid water density. The rain rate R (mm h^{-1}) is expressed by

$$R = 6\pi \times 10^{-4} \sum_{i=3}^{23} \sum_{j=1}^{32} D_i^3 \frac{n_{ij}}{A_i \Delta t}. \tag{2.7}$$

Here, to see the contribution of the rain rate for each diameter bin to the total rain rate, the rain rate for the ith diameter bin $R(D_i)$ (mm h^{-1} mm^{-1}) (Ma et al. 2019) is calculated by

$$R(D_i) = 6\pi \times 10^{-4} \sum_{j=1}^{32} D_i^3 \frac{n_{ij}}{A_i \Delta t \Delta D_i}, \tag{2.8}$$

which satisfies

$$R = \sum_{i=3}^{23} R(D_i) \Delta D_i. \tag{2.9}$$

The 1-min disdrometer data can be described by the normalized gamma drop size distribution (Testud et al. 2001) as

$$N(D) = N_{\mathrm{w}} \frac{(4+\mu)^{4+\mu}}{4^4} \frac{\Gamma(4)}{\Gamma(4+\mu)} \left(\frac{D}{D_{\mathrm{m}}} \right)^{\mu} \exp\left[-(4+\mu) \frac{D}{D_{\mathrm{m}}} \right]. \tag{2.10}$$

where μ is the shape parameter of the gamma drop size distribution, N_{w} (m^{-3} mm^{-1}) is the generalized intercept parameter, D_{m} (mm) is the mass-weighted mean diameter, and Γ is the gamma function. N_{w} and D_{m} are given by

$$N_{\mathrm{w}} = \frac{4^4}{\pi\rho_{\mathrm{w}}}\left(\frac{10^3 W}{D_{\mathrm{m}}^4}\right), \tag{2.11}$$

$$D_{\mathrm{m}} = \frac{M_4}{M_3}. \tag{2.12}$$

The 1-minute disdrometer data can also be described by the gamma drop size distribution in the following form (Ulbrich 1983; Cao and Zhang 2009):

$$N(D) = N_0 D^{\mu} \exp(-\Lambda D), \tag{2.13}$$

where N_0 ($\mathrm{m}^{-3}\ \mathrm{mm}^{-1-\mu}$) is the intercept parameter, Λ (mm^{-1}) is the slope parameter, and μ is the shape parameter. The three parameters are calculated by

$$N_0 = \frac{M_2 \Lambda^{\mu+3}}{\Gamma(\mu+3)}, \tag{2.14}$$

$$\Lambda = \frac{M_2}{M_4}(\mu+3)(\mu+4), \tag{2.15}$$

$$\mu = \frac{(7-11\eta)-(\eta^2+14\eta+1)^{(1/2)}}{2(\eta-1)}, \tag{2.16}$$

where η is given by

$$\eta = \frac{M_4^2}{M_2 M_6}\ . \qquad (2.17)$$

To validate the disdrometer data, the hourly accumulated rainfall amount observed by the disdrometer at each site is compared to that observed by the collocated rain gauge (Fig. 2.2). Note that for Chuncheon, the comparison is done for the period from 2 October 2019, not for the whole period, because of the poor data quality before that. At all sites, the disdrometers generally underestimate the hourly accumulated rainfall amount. This underestimation could be caused by the quality control that excludes data that do not satisfy certain conditions. Despite the underestimation, the hourly accumulated rainfall amount from the disdrometer is highly correlated with that from the rain gauge ($R \geq 0.98$ for all sites), suggesting that the RSD parameters estimated from the disdrometer data have sufficient reliability.

2.2.2 Rain-type classification

Many RSD studies showed that RSD characteristics differ depending

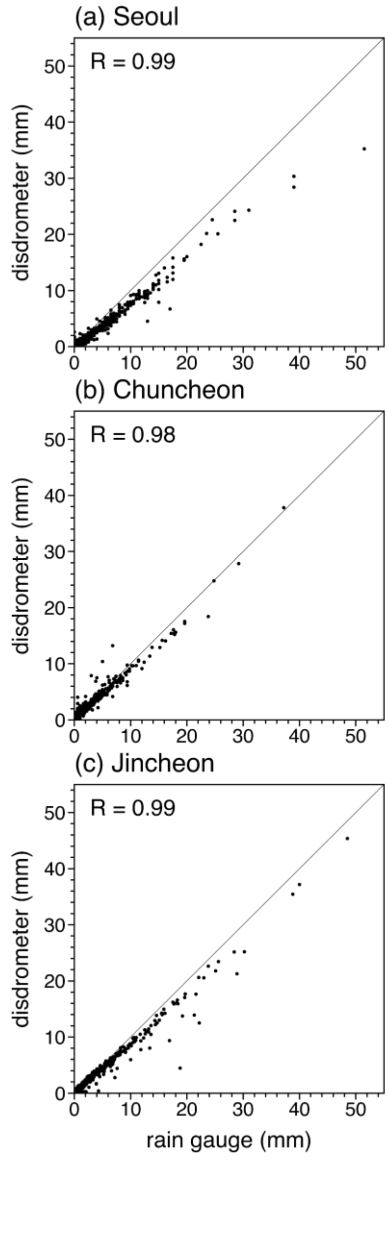

Figure 2.2 Scatter plots of hourly accumulated rainfall amount observed by t he disdrometers and rain gauges in (a) Seoul, (b) Chuncheon, and (c) Jincheon.

on the rain type (Tokay and Short 1996; Bringi et al. 2003; Niu et al. 2010; Chen et al. 2017; Seela et al. 2017; Jwa et al. 2021) To determine the rain type of each 1-min disdrometer data, the method suggested by Bringi et al. (2009) is used. Bringi et al. (2009) suggested a line in the N_w–D_0 plane, where D_0 is the median volume diameter, that separates the convective and stratiform rain types, which is expressed by

$$\log_{10}(N_{\mathrm{w}}^{\mathrm{sep}}) = -1.6 D_0 + 6.3. \tag{2.18}$$

Using Eq. (2.13), they suggested the likelihood index I, which is defined as

$$I = \log_{10}(N_{\mathrm{w}}) - \log_{10}(N_{\mathrm{w}}^{\mathrm{sep}}). \tag{2.19}$$

Thurai et al. (2016) classified the rain type of 1-min disdrometer data using I. When $I < -0.3$ ($I > 0.3$), the 1-min disdrometer data is identified as convective (stratiform) rain, otherwise it is classified as mixed rain.

2.2.3 Reanalysis data

To investigate the thermodynamical and cloud characteristics at each site which may be associated with the RSD characteristics at the site, the reanalysis version 5 from the European Centre for Medium-Range Weather Forecasts (ERA5, Hersbach et al. 2020) with 1-h temporal resolution and 0.25° × 0.25° horizontal resolution is used. The convective available potential energy (CAPE), cloud-base height, cloud fraction, and hydrometeor mass contents in the ERA5 data at the grid point which is closest to each of the disdrometer sites are used. In addition, cloud-top height is obtained by identifying the topmost grid where the cloud fraction is greater than 0.01 and the total mass content of hydrometeors is greater than 10^{-3} g kg^{-1}.

2.3 Result and discussion

2.3.1 Regional differences in precipitation and RSD characteristics

To examine the differences in precipitation characteristics among the three sites, the accumulated rainfall amount and accumulated rainfall duration are shown in Fig. 2.3a. The accumulated rainfall amount (duration) is 2568 mm (889 h) for Seoul, 2697 mm (880 h) for Chuncheon, and 2845 mm (1090 h) for Jincheon. Jincheon exhibits the largest accumulated rainfall amount and duration, but the mean rainfall intensity calculated by dividing the accumulated rainfall amount by the accumulated rainfall duration is 2.6 mm

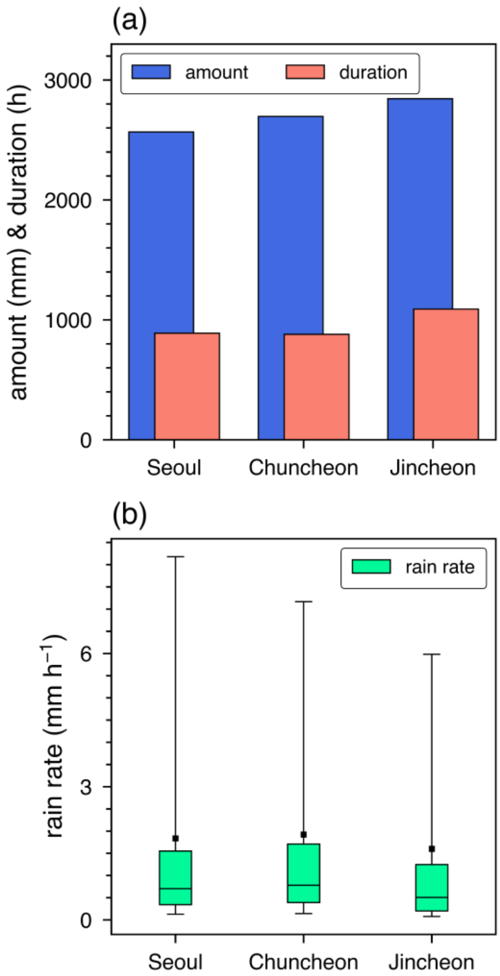

Figure 2.3 (a) Accumulated rainfall amount and duration and (b) box plot of rain rate for rainfall events at each site. The upper boundary, centerline, and lower boundary of the boxes represent the 75th, 50th, and 25th percentiles, respectively. The upper and lower whiskers indicate the 95th and 5th percentiles, respectively. The black squares in the box plots represent the mean value.

h^{-1}, which is the smallest among the three sites. Seoul and Chuncheon have similar accumulated rainfall durations, but Chuncheon has a larger accumulated rainfall amount than Seoul. This indicates that the mean rainfall intensity in Chuncheon (3.1 mm h^{-1}) is greater than that in Seoul (2.9 mm h^{-1}).

Figure 2.3b shows the box plot of rain rate for rainfall events at each site. Here, a single rainfall event is composed of a set of consecutive 1-min disdrometer data, and the rain rate is obtained for each event. The numbers of rainfall events in Seoul, Chuncheon, and Jincheon are 1958, 1730, and 2109, respectively. The rain rate averaged over the rainfall events in Jincheon (1.6 mm h^{-1}) is smaller than those of Seoul (1.8 mm h^{-1}) and Chuncheon (1.9 mm h^{-1}). The 95th percentile of rain rate in Jincheon (6.0 mm h^{-1}) is also smaller than those in Seoul (8.2 mm h^{-1}) and Chuncheon (7.2 mm h^{-1}). The mean and 75th percentile of rain rate in Seoul are smaller than those in Chuncheon, but the 95th percentile of rain rate in Seoul is larger than that in Chuncheon. This suggests that the rainfall in Chuncheon is stronger on average than that in Seoul, but Seoul experiences more extreme rainfall events than Chuncheon.

Figure 2.4a shows the RSD for each site, obtained by averaging those from 1-min disdrometer data. The raindrop number concentration in Jincheon peaks at D = 0.437 mm, while those in Seoul and Chuncheon both peak at larger D (0.562 mm). For smaller diameters, the raindrop number

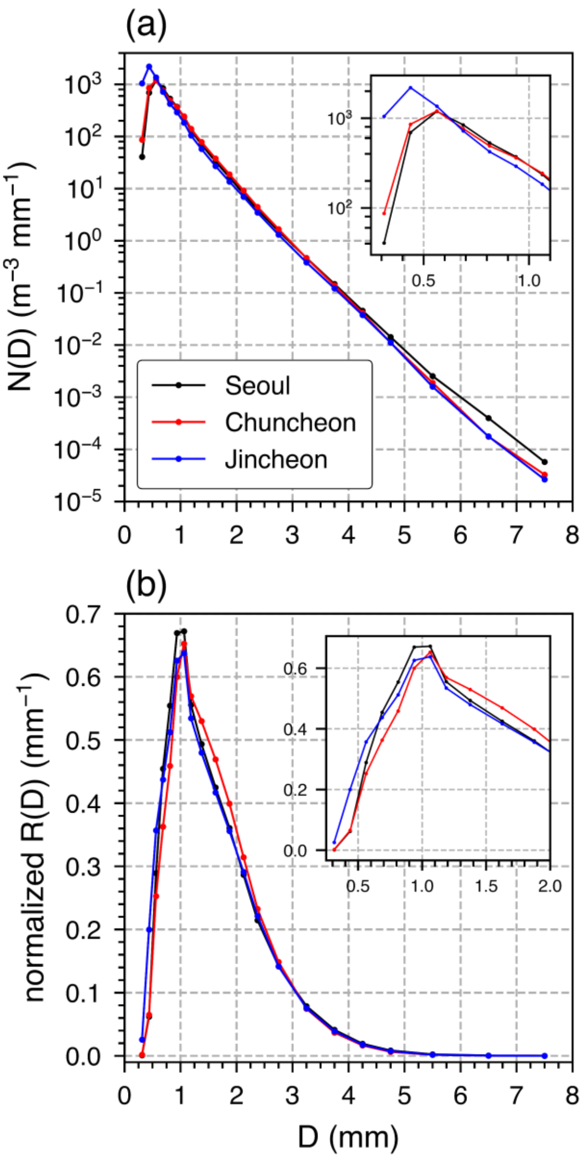

Figure 2.4 (a) Raindrop size distribution and (b) normalized R(D) at each site.

concentrations in Seoul and Chuncheon sharply decrease, being about 1-order smaller than that in Jincheon for the smallest-diameter bin (D = 0.25–0.375 mm). As the diameter increases from the RSD peaks, the raindrop number concentrations at all sites decrease almost exponentially, which resemble the Marshall-Palmer distribution (Marshall and Palmer 1948). Chuncheon shows the largest raindrop number concentration for D = 1–3 mm. Seoul shows the largest raindrop number concentration for $D \geq 3$ mm, and the difference from those at other two sites is prominent especially for $D \geq 6$ mm. Figure 2.4b shows the normalized $R(D)$ for each site, obtained by averaging those from 1-min disdrometer data and normalizing by the total rain rate. The area under the normalized $R(D)$ curve indicates the contribution of the raindrops in each diameter bin to the total rain rate. Jincheon shows a greater contribution of small raindrops to the total rain rate than the other two sites: the area under the normalized $R(D)$ curve for D = 0.25–0.625 mm is 0.07 in Jincheon, which is larger than those in Seoul and Chuncheon (0.04 and 0.04). Another notable difference is found at D = 1.125–3 mm. For this diameter range that is responsible for a large portion of the total rain rate, Chuncheon shows the largest area under the normalized $R(D)$ curve (0.63), followed by Seoul (0.59) and Jincheon (0.58).

The differences in RSD characteristics among the three sites can be better shown by looking into the probability density functions (PDFs) for

RSD parameters. Figure 2.5 shows the PDFs of the logarithm of total raindrop number concentration $\log_{10}N_t$, the radar reflectivity Z, the logarithm of rainwater content $\log_{10}W$, the logarithm of rain rate $\log_{10}R$, the mass-weighted diameter D_m, and the logarithm of generalized intercept parameter $\log_{10}N_w$ at each site. The mean and standard deviation values of the six RSD parameters are given in Table 2.1. The PDFs of $\log_{10}N_t$ are positively skewed at all sites. Jincheon's PDF of $\log_{10}N_t$ is highly distinguishable from those of Seoul and Chuncheon, showing a peak at larger $\log_{10}N_t$ (2.65) than the other two sites (2.45 for both Seoul and Chuncheon). Also, the $\log_{10}N_t$ PDF in Jincheon is more widely distributed than the others: the standard deviation of $\log_{10}N_t$ in Jincheon (0.37) is larger than those in Seoul (0.31) and Chuncheon (0.31). This is associated with the much larger PDF in Jincheon for $\log_{10}N_t > 3$. For Z, Chuncheon shows the largest mean value (24.73 dBZ), followed by Seoul (23.74 dBZ) and Jincheon (22.02 dBZ). The PDF of Z in Chuncheon is least positively skewed, showing the largest values for 22 dBZ $< Z <$ 42 dBZ among the three sites. This suggests that Chuncheon experiences the most frequent appearance of large raindrops. In contrast, Jincheon shows the largest PDF for $Z <$ 16 dBZ among the three sites. The PDFs of $\log_{10}W$ and $\log_{10}R$ where Jincheon shows large values for small W and R, respectively, reflect the higher frequency of light rain in Jincheon than in Seoul and Chuncheon.

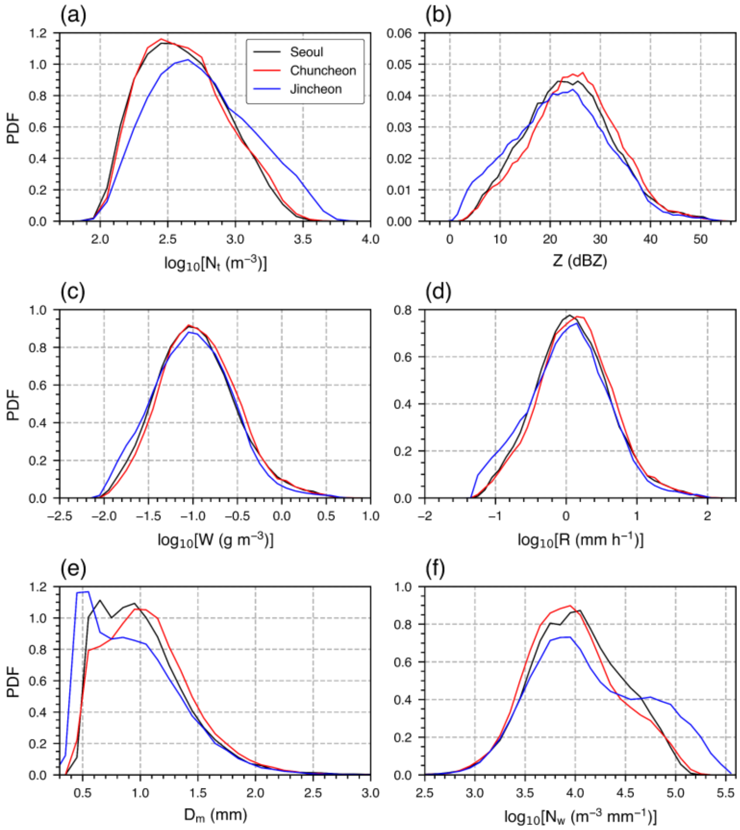

Figure 2.5 Probability density functions of (a) $\log_{10}N_t$, (b) Z, (c) $\log_{10}W$, (d) $\log_{10}R$, (e) D_m, and (f) $\log_{10}N_w$ for each site.

Table 2.1 Mean and standard deviation (in parentheses) values of RSD parameters for each site. The units of N_t, Z, W, R, D_m, and N_w are m^{-3}, dBZ, g m^{-3}, mm h^{-1}, mm, and m^{-3} mm^{-1}, respectively.

site data #	$\log_{10}N_t$	Z	$\log_{10}W$	$\log_{10}R$	D_m	$\log_{10}N_w$
Seoul 53,340	2.61 (0.31)	23.74 (8.69)	−0.96 (0.44)	0.10 (0.53)	1.02 (0.38)	4.03 (0.45)
Chuncheon 52,787	2.63 (0.31)	24.73 (8.58)	−0.92 (0.43)	0.14 (0.53)	1.07 (0.38)	3.99 (0.45)
Jincheon 65,405	2.75 (0.37)	22.02 (9.43)	−1.00 (0.44)	0.03 (0.57)	0.95 (0.41)	4.16 (0.57)

The PDFs of D_m and $\log_{10}N_w$ show clear differences among the three sites. The PDF of D_m in Jincheon peaks at D_m = 0.55 mm, drops at D_m = 0.55–0.65 mm, and plateaus until D_m = 1.1 mm. The high frequency of small D_m may be associated with the high frequency of light rain in Jincheon. The PDF of D_m in Seoul shows a bimodal distribution, peaking at D_m = 0.65 and 0.95 mm. Chuncheon shows the PDF of D_m that peaks at much larger D_m (0.95 mm) than that in Jincheon, and also shows the largest PDF for D_m = 1.0–2.4 mm among the three sites. The PDF of $\log_{10}N_w$ in Jincheon shows a peak at $\log_{10}N_w$ = 3.95 and a plateau in the range of $\log_{10}N_w$ = 4.4–4.9. The former is related to the plateau in the D_m PDF for D_m = 0.7–1.1 mm and the latter is related to the peak at D_m = 0.55 mm. The PDFs of $\log_{10}N_w$ in Seoul and Chuncheon show their maxima at 4.05 and 3.95, respectively.

2.3.2 RSD characteristics according to the rain rate and rain type and their regional differences

In this subchapter, the RSD characteristics at each site are examined according to the rain rate and rain type and their differences among the three sites are investigated. Figure 2.6a–c shows the density scatter plots of D_m and $\log_{10}N_w$ at each site, where the D_m–$\log_{10}N_w$ line that was obtained through the least square fitting of stratiform rain data by Bringi et al. (2003) is indicated.

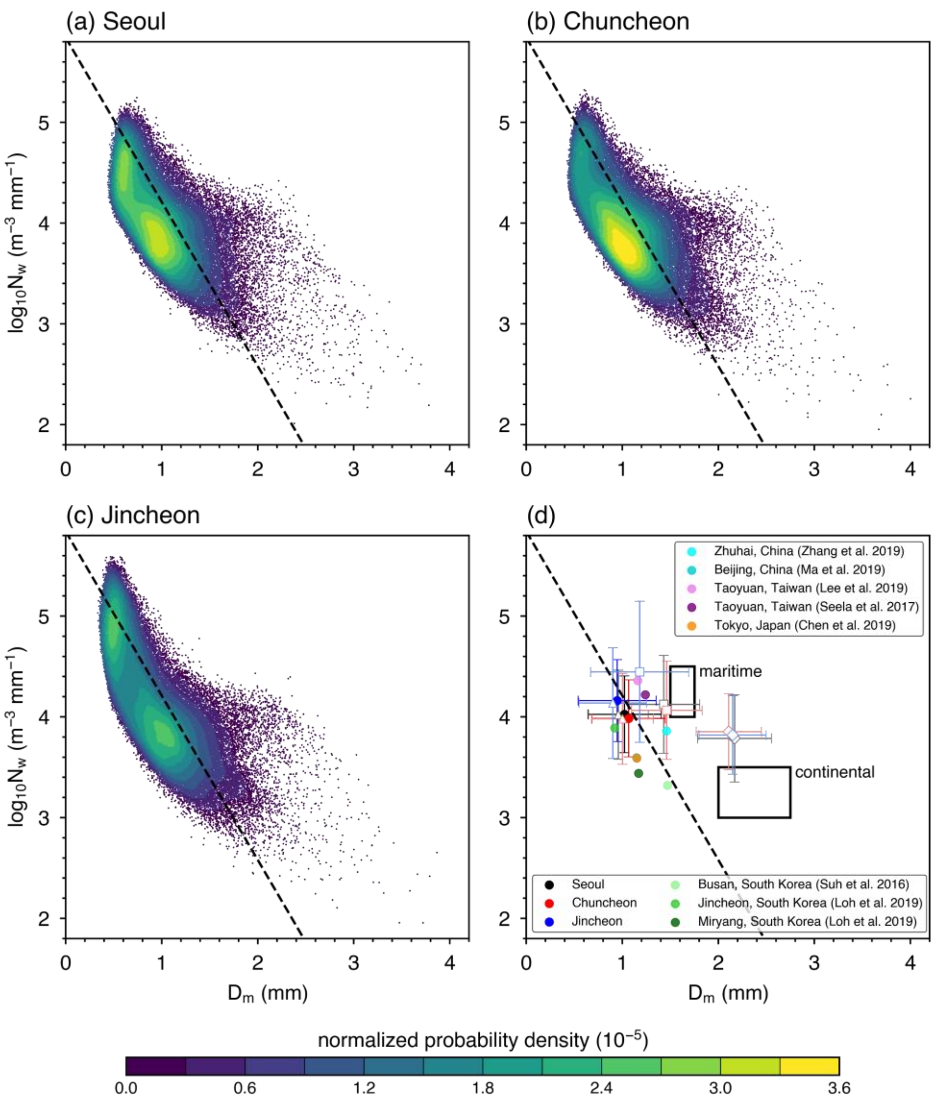

(a) Seoul
(b) Chuncheon
(c) Jincheon
(d)
$\log_{10}N_w$ (m^{-3} mm^{-1})
D_m (mm)
Zhuhai, China (Zhang et al. 2019)
Beijing, China (Ma et al. 2019)
Taoyuan, Taiwan (Lee et al. 2019)
Taoyuan, Taiwan (Seela et al. 2017)
Tokyo, Japan (Chen et al. 2019)
maritime
continental
Seoul
Chuncheon
Jincheon
Busan, South Korea (Suh et al. 2016)
Jincheon, South Korea (Loh et al. 2019)
Miryang, South Korea (Loh et al. 2019)
normalized probability density (10^{-5})
0.0
0.6
1.2
1.8
2.4
3.0
3.6

Figure 2.6 Density scatter plots of the mass-weighted diameter and the logarithm of generalized intercept parameter for (**a**) Seoul, (**b**) Chuncheon, and (**c**) Jincheon. (d) shows the mean values of D_{m} and $\log_{10}N_{\mathrm{w}}$ for the total (filled circles), stratiform rain (triangles), mixed rain (squares), and convective rain (diamonds) at each site with their standard deviation (whiskers). The mean values obtained in previous studies for East Asia are represented by different color dots in (d). Note that the dots of Ma et al. (2019) and Chen et al. (2019) overlap each other. The black dashed line represents the stratiform line proposed by Bringi et al. (2003). The two boxes in (d) represent the maritime-like convective rain and continental-like convective rain proposed by Bringi et al. (2003), respectively.

At all sites, a large portion of data appear near or below the stratiform line, indicating that stratiform rain dominates the precipitation. All three sites show a peak of probability density at D_m = 0.8–1.2 mm and $\log_{10}N_w$ = 3.6–4.2. In addition to this peak, Jincheon shows a prominent peak at D_m = 0.4–0.6 mm and $\log_{10}N_w$ = 4.6–5.1, and the probability densities of the two peaks are similar. The two peaks explain the distinctive distributions of D_m and $\log_{10}N_w$ PDFs in Jincheon, each of which has a peak and a plateau (Fig. 2.5e and f). This peak does not appear in Chuncheon. Seoul shows a secondary peak at D_m = 0.5–0.7 mm and $\log_{10}N_w$ = 4.2–4.8, but its probability density is much smaller than that of the primary peak.

Figure 2.6d shows the mean and standard deviation values of D_m and $\log_{10}N_w$ at each site for the total and each rain type, where two boxes represent the clusters of maritime-like convective rain and continental-like convective rain proposed by Bringi et al. (2003). For the total data, the mean D_m–$\log_{10}N_w$ pair at each station appears near the stratiform line and within the range of the primary peak (D_m = 0.8–1.2 mm and $\log_{10}N_w$ = 3.6–4.2) in the D_m–$\log_{10}N_w$ density scatter plots (Fig. 2.6a–c). Jincheon shows the smallest mean D_m (0.94 mm) and largest mean $\log_{10}N_w$ (4.16), while Chuncheon shows the largest mean D_m (1.06 mm) and smallest mean $\log_{10}N_w$ (3.98). The mean D_m–$\log_{10}N_w$ pair for stratiform rain also appear near the stratiform line, which is similar to those for the total, because stratiform rain accounts for about 90% of the total.

For mixed rain, the mean D_m–$\log_{10}N_w$ pair in Jincheon largely deviates from those in Seoul and Chuncheon. The mean D_m–$\log_{10}N_w$ pair in Jincheon is in an intermediate position between the stratiform line and the cluster of maritime-like convective rain, while those in Seoul and Chuncheon are close to the cluster of maritime-like convective rain. For convective rain, the mean D_m–$\log_{10}N_w$ pairs at all three sites are in intermediate positions between the clusters of maritime-like convective rain and continental-like convective rain. The difference among the three sites for convective rain is relatively small compared to that for the other rain types.

In Fig. 2.6d, mean D_m and $\log_{10}N_w$ obtained at many other locations in East Asia are also presented. Compared to the mean D_m–$\log_{10}N_w$ pair in Jincheon obtained in this study, that obtained by Loh et al. (2019) for the same site show similar mean D_m (0.92 mm) but somewhat smaller $\log_{10}N_w$ (3.89), which may be because Loh et al. (2019) obtained them from only twelve selected rainfall cases. Miryang (Loh et al. 2019), located in the southeastern region of South Korea, shows $\log_{10}N_w$ (3.44) that is much smaller than the three sites examined in this study and D_m (1.17 mm) that is comparable to that in Seoul (1.02 mm) and Chuncheon (1.06 mm). Busan (Suh et al. 2016), a coastal city of South Korea located farther southeast from the three sites examined in this study, shows $\log_{10}N_w$ further smaller that in Miryang and D_m much larger than the other South Korean cities. Busan exhibits the longest distance in the D_m–$\log_{10}N_w$ space from the three sites examined in this study, even longer than that for any other city in East Asia presented in Fig. 2.6d, which indicates that South Korea has a very large variability of RSD characteristics within the country. Beijing (Ma et al. 2019) and Tokyo (Chen et al. 2019) show almost identical mean D_m and $\log_{10}N_w$, and the mean D_m–$\log_{10}N_w$ pair is below the stratiform line, as in the South Korean cities. Mean D_m in the two cities (1.15 and 1.15 mm) are comparable to that in Seoul and Chuncheon and mean $\log_{10}N_w$ in the two cities (3.60, 3.59) are smaller than that in the three sites examined in this study. Taoyuan (Seela et al. 2017; Lee et al. 2019) and Zhuhai (Zhang et al. 2019), coastal cities located at much lower latitudes than the aforementioned cities, show the mean RSD characteristics that are closer to those of maritime-like convective precipitation than any other city.

Among the three sites, Seoul shows the largest proportion of convective rain, Chuncheon shows the largest proportion of mixed rain, and Jincheon shows the largest proportion of stratiform rain. In terms of the precipitation amount, the stratiform, mixed, and convective rain respectively account for 47.4%, 27.9%, 24.7% in Seoul, 47.3%, 28.6%, and 24.1% in Chuncheon, and 49.6%, 27.0%, and 23.4% in Jincheon.

Figure 2.7 shows the PDFs of D_m and $\log_{10}N_w$ for each rain type at each site. For stratiform rain, as in the PDF without the rain-type classification

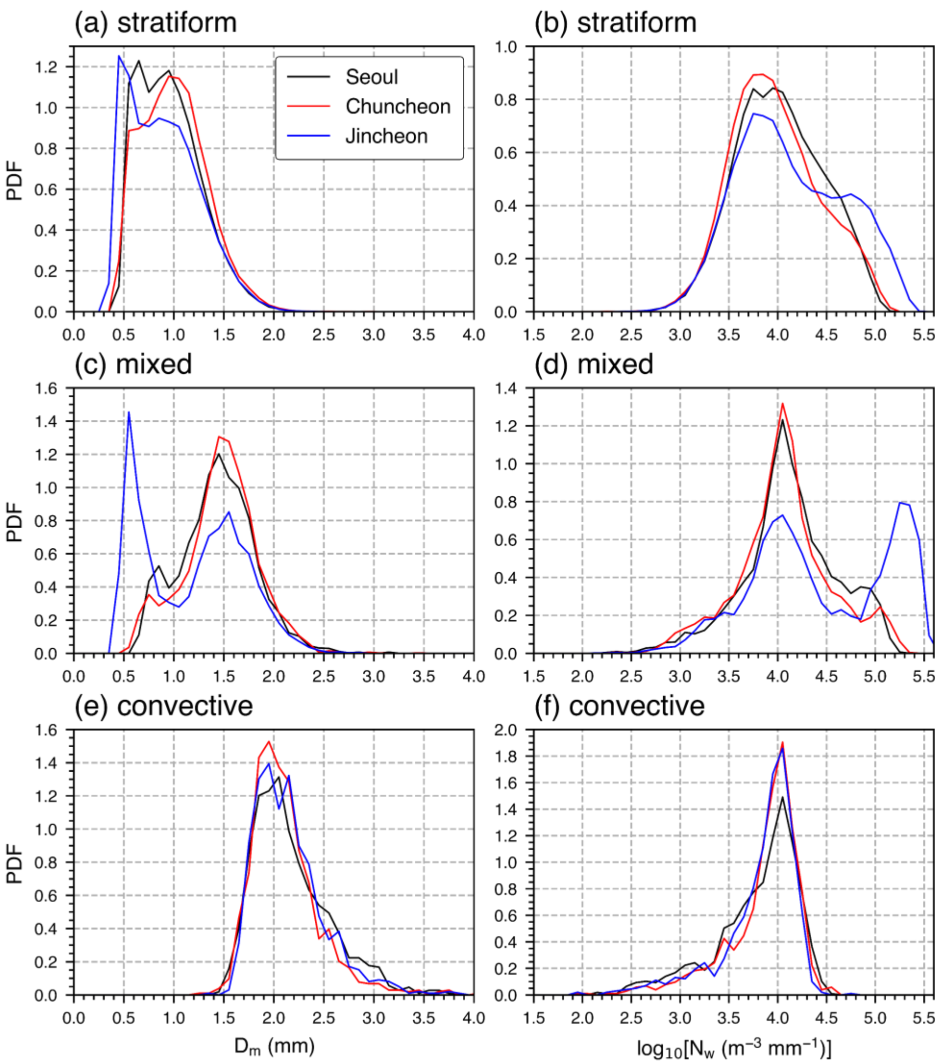

Figure 2.7 Probability density functions of (a,c,e) the mass-weighted mean diameter and (b,d,f) the logarithm of generalized intercept parameter for (a,b) stratiform, (c,d) mixed, and (e,f) convective rain at each site.

(Fig. 2.5e), the D_m value at which the PDF is maximized is smallest (0.45) in Jincheon and largest (0.95) in Chuncheon. Jincheon shows a distinct shape of $\log_{10}N_w$ PDF, which is relatively high at large $\log_{10}N_w$ compared to the other sites. In contrast, Chuncheon shows relatively high PDF at small $\log_{10}N_w$ compared to the other sites. For both D_m and $\log_{10}N_w$, Seoul shows somewhat intermediate distributions of PDF between Chuncheon and Jincheon. For convective rain, all sites have similar distributions of PDFs of D_m and $\log_{10}N_w$. Compared to stratiform rain, the PDF of D_m for convective rain is distributed mainly at much larger D_m and the PDF of $\log_{10}N_w$ at large $\log_{10}N_w$ is very low. The distributions of PDFs of D_m and $\log_{10}N_w$ for convective rain in Seoul are more dispersed than those in Chuncheon and Jincheon, showing overall higher PDF at large D_m (2.45 mm < D_m < 3.05 mm) and at small $\log_{10}N_w$ (2.45 < $\log_{10}N_w$ < 3.65). For mixed rain, the PDFs of D_m at all sites have double-peak structures where the peak on the left side is close to the peak of D_m PDF for stratiform rain and the peak on the right side is close to the peak of D_m PDF for convective rain. This double-peak structure of D_m PDF for mixed rain is also reported by Jwa et al. (2021) who examined the RSD characteristics in Seoul, and they suggested that the two peaks are associated with different weather types which are the Changma front and the low-pressure system. They showed that the RSD characteristic of mixed rain of the Changma front resembles that of convective rain, while the RSD characteristic of mixed rain of the low-pressure system resembles that of stratiform rain. In Jincheon, the stratiform-like peak is higher than the convective-like peak, while it is the opposite in Seoul and Chuncheon. For $\log_{10}N_w$, Jincheon again shows a different shape of PDF where the PDF is maximized at $\log_{10}N_w = 5.25$, while it is maximized at $\log_{10}N_w = 4.05$, which is the same as the $\log_{10}N_w$ value for the PDF peak for convective rain, in Seoul and Chuncheon. The distinct two peaks of $\log_{10}N_w$ PDF for mixed rain in Jincheon are closely linked to the distinct two peaks of D_m PDF. The left (right) peak among the former corresponds to the right (left) peak among the latter.

To further investigate the differences in RSD characteristics among the three sites, the relationship between the rain rate and D_m and that between the rain rate and $\log_{10}N_w$ at each site are presented in Fig. 2.8. D_m and $\log_{10}N_w$ are averaged for each of the eight rain rate categories, which is 0.05 mm h^{-1} $\le R <$ 0.5 mm h^{-1}, 0.5 mm h^{-1} $\le R <$ 1.0 mm h^{-1}, 1 mm h^{-1} $\le R <$ 2 mm h^{-1}, 2 mm h^{-1} $\le R <$ 5 mm h^{-1}, 5 mm h^{-1} $\le R <$ 10 mm h^{-1}, 10 mm h^{-1} $\le R <$ 20 mm h^{-1}, 20 mm h^{-1} $\le R <$ 50 mm h^{-1}, and 50 mm h^{-1} $\le R$. At all sites, D_m increases as the rain rate increases. For the rain rate in the range of 0.05−5 mm h^{-1}, Jincheon shows the smallest D_m. Chuncheon shows the largest D_m for the rain rate in the range of 0.05−20 mm h^{-1} and the smallest D_m for the rain rate larger than 20 mm h^{-1}. The relationship between the rain rate and $\log_{10}N_w$ is not monotonic at all sites. For the rain rate in the range of 0.05−5

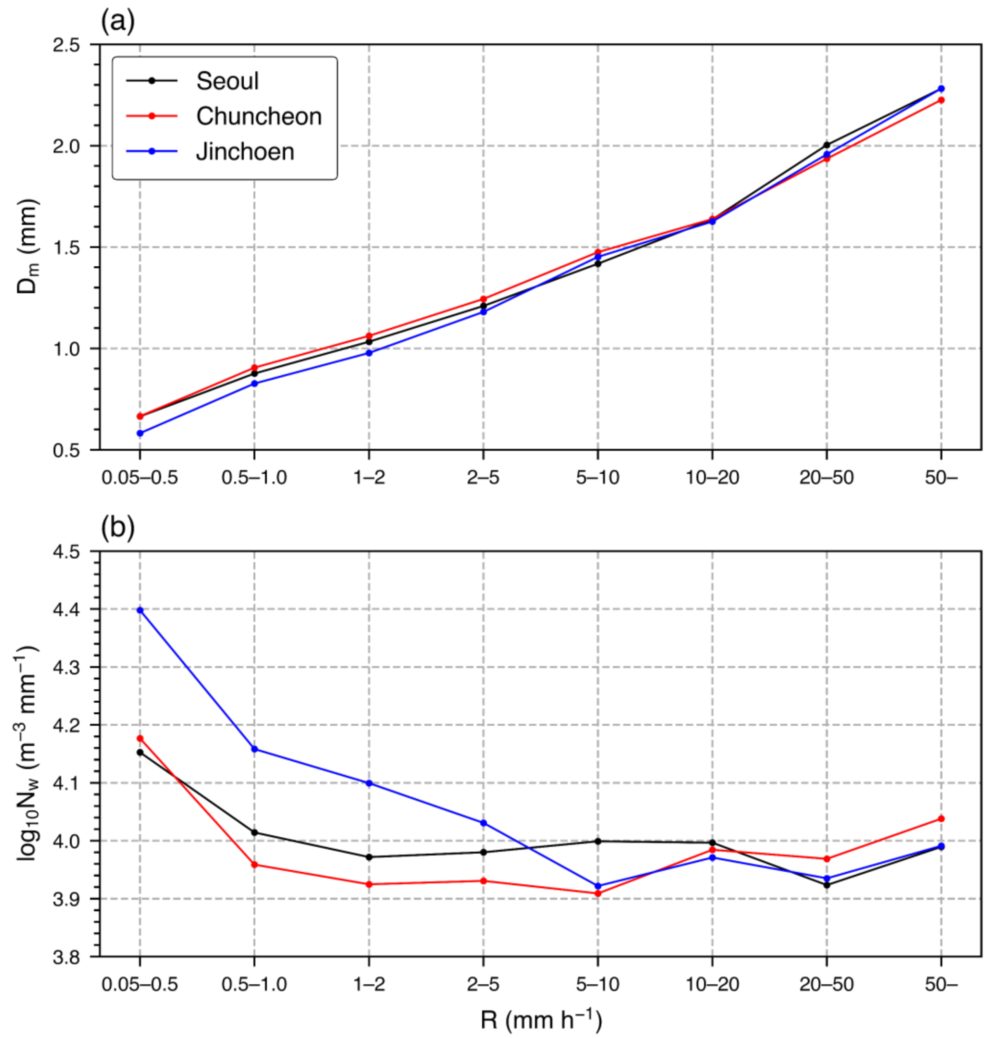

Figure 2.8 (a) Mass-weighted mean diameter and (b) logarithm of generalized intercept parameter averaged over RSD data in each rain rate category at each site.

mm h^{-1}, Jincheon shows the largest $\log_{10}N_w$ among the three sites. For the rain rate larger than 20 mm h^{-1}, Chuncheon shows the largest $\log_{10}N_w$. The above relationships between the rain rate and the two RSD parameters indicate that light precipitation in Jincheon consists of a relatively large number of relatively small raindrops compared to light precipitation in the other sites and that very heavy precipitation in Chuncheon consists of a relatively small raindrops compared to very heavy precipitation in other sites. Very heavy precipitation in Seoul consists of relatively large raindrops compared to very heavy precipitation in Chuncheon.

The above analyses in subchapters 2.3.1 and 2.3.2 reveal the differences in precipitation and RSD characteristics among the three cities in South Korea. Jincheon, the least populated and southernmost city among the three cities, is characterized by the smallest mean rainfall intensity with a relatively high frequency of light rain, which is associated with the smallest D_m and largest $\log_{10}N_w$. In contrast, Chuncheon, a medium-sized city located in a basin, is characterized by the largest mean rainfall intensity with a relatively high frequency of heavy rain, which is associated with the largest D_m and smallest $\log_{10}N_w$. Seoul, the most populated city in South Korea, is characterized by the intermediate mean rainfall intensity associated with the intermediate D_m and $\log_{10}N_w$ between those in Chuncheon and Jincheon. Distinctive features of the precipitation and RSD characteristics in Seoul are that although the mean rainfall intensity is weaker and the mean D_m is smaller than those in Chuncheon, extreme rainfall events occur more frequently and D_m for very heavy rain is larger compared to Chuncheon. In the next subchapter, possible causes for these regional differences in RSD characteristics are investigated.

2.3.3 Reginal differences in thermodynamic and cloud characteristics

The regional differences in thermodynamical and cloud microphysical characteristics that may be responsible for regional differences in RSD characteristics are examined. Figure 2.9 shows the box plots of the convective available potential energy (CAPE), cloud-top height, and cloud-base height at each site. The median and 75th and 95th percentiles of CAPE in Jincheon are smallest among those in the three sites, indicating that Jincheon has the least thermodynamical potential of development of strong convection, which is also supported by the overall lowest cloud-top height. Because relatively weak convective activities in clouds may lead to relatively insufficient growth of hydrometeor particles due to less interaction with each other, the overall smallest CAPE and lowest cloud-top height in Jincheon can be responsible for the smallest D_m. Compared to Jincheon, Chuncheon shows

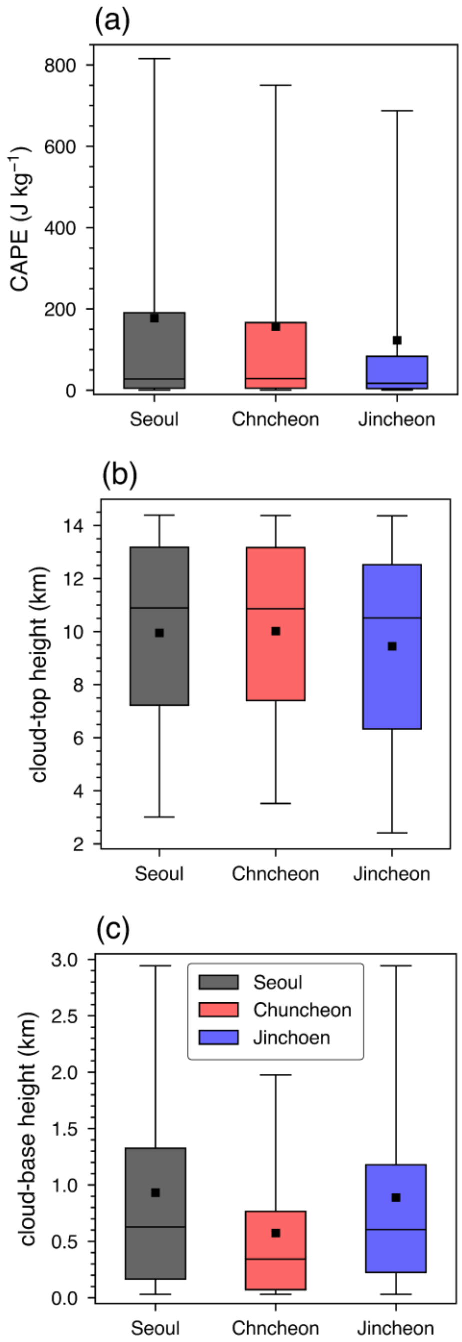
(a)
CAPE (J kg^{-1})
800
600
400
200
0
Seoul
Chncheon
Jincheon
(b)
cloud-top height (km)
14
12
10
8
6
4
2
Seoul
Chncheon
Jincheon
(c)
cloud-base height (km)
3.0
2.5
2.0
1.5
1.0
0.5
0.0
Seoul
Chuncheon
Jinchoen
Seoul
Chncheon
Jincheon

Figure 2.9 Box plots of (a) convective available potential energy, (b) cloud-top height, and (c) cloud-base height at each site. The upper boundary, centerline, and lower boundary of the boxes represent the 75th, 50th, and 25th percentiles, respectively. The upper and lower whiskers indicate the 95th and 5th percentiles, respectively. The black squares in the box plots represent the mean value.

noticeably larger mean and 75th and 95th percentiles of CAPE and higher cloud-top height, which implies stronger convective activities in clouds that may be associated with the substantially larger D_m. The D_m difference between Jincheon and Chuncheon is similar to that between Palau and Taiwan reported by Seela et al. (2017), who also attributed the difference to the stronger convective activity in Taiwan than in Palau. In addition, the cloud-base height is lowest in Chuncheon. The low cloud-base height indicates less evaporation of raindrops below the cloud base and thus results in the larger sizes of raindrops at the surface. Seoul shows the largest 75th and 95th percentiles of CAPE. This can be associated with the most frequent occurrence of extreme rainfall events in Seoul. Compared to Chuncheon, the cloud-top height is overall similar but the cloud-base height is overall much higher, which may be responsible for the smaller mean D_m.

2.3.4 Implications for quantitative precipitation estimations and cloud microphysics parameterizations

From RSD data, some relations between RSD parameters that are useful for quantitative precipitation estimations and cloud microphysics parameterizations can be obtained. One example is the radar reflectivity–rain rate (Z–R) relation that can be used to estimate surface rain rate from radar observation. The power-law fitted Z–R relations ($Z = aR^b$) at the three sites are compared in Fig. 2.10. The exponent b in the Z–R relation is similar among the three sites (1.56–1.59), while the coefficient a varies from 144 in Jincheon to 182 in Chuncheon (Fig. 2.10a). Up to Z = 68 dBZ, rain rate is smallest in Chuncheon and largest in Jincheon for the same radar reflectivity. For example, for Z = 45 dBZ, rain rate is as small as 27.3 mm h^{-1} in Chuncheon and as large as 29.7 mm h^{-1} in Jincheon, differing by 2.4 mm h^{-1}. The exponent b at the three sites is mostly larger than that in the southern region of South Korea (1.41–1.61 for stratiform rain and 1.39–1.48 for convective rain) obtained by Suh et al. (2021), and it is rather close to that in summertime Beijing (1.57) obtained by Ma et al. (2019). That Chuncheon shows the largest a among the three sites is consistent with the finding of Suh et al. (2021) that a is larger at inland sites than at coastal sites in the southern region of South Korea.

The features of the Z–R relations at the three sites found for the total data are also found when the stratiform rain data only are considered. For stratiform rain, the three sites show b that is similar among them (1.60–1.64) and a that is smallest in Jincheon (154) and largest in Chuncheon (186) (Fig. 2.10b). The exponent b for stratiform rain is similar to that obtained by Marshall and Palmer (1948) for warm stratiform rain (1.6). Compared to

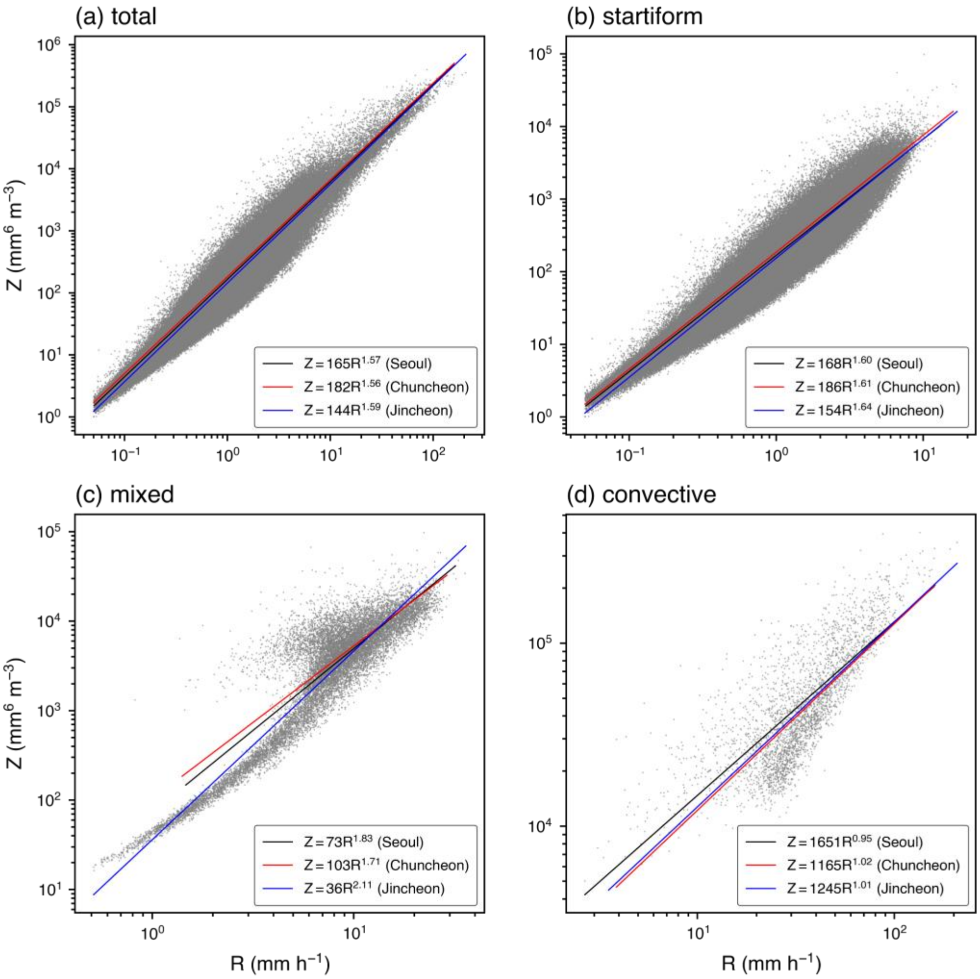

Figure 2.10 Scatter plot of the rain rate R and the radar reflectivity Z for (a) the total, (b) stratiform rain, (c) mixed rain, and (d) convective rain. The black, red, and blue lines represent the power-law fitted Z-R relations for Seoul, Chuncheon, and Jincheon, respectively.

stratiform rain, convective rain shows much smaller b (0.95–1.02) and much larger a (1165–1651) at all three sites (Fig. 2.10d). Smaller b and larger a for convective rain compared to stratiform rain are consistent with Marshall et al. (1955) who suggested $Z = 200R^{1.6}$ for stratiform rain and $Z = 300R^{1.4}$ for convective rain, but the differences in this study are much more drastic. For convective rain, the coefficient a is smallest in Chuncheon, which is in contrast with its behavior for stratiform rain. Mixed rain shows most distinct differences among the three sites (Fig. 2.10c). For mixed rain, Chuncheon shows the largest a and smallest b, while Jincheon shows the smallest a and largest b.

The shape parameter–slope parameter (μ–Λ) relation can be used to retrieve RSD when only limited information on RSD is given, which is the case for estimating rain rate from radar observation (Zhang et al. 2001) and for retrieving three-parameter gamma RSD from two prognostic RSD moments in double-moment cloud microphysics schemes (Morrison and Milbrandt 2015). The μ–Λ relation is known to vary with the location (see Table 8 in Seela et al. (2018) and Table 3 in Han et al. (2021)). Figure 2.11 shows the second-order polynomial fits for the μ–Λ relation at the three sites. Here, following Zhang et al. (2003), only the data with rain rate larger than 5 mm h^{-1} and with the total raindrop count larger than 1000 are considered. The μ–Λ relations at the three sites are overall similar to each other, which

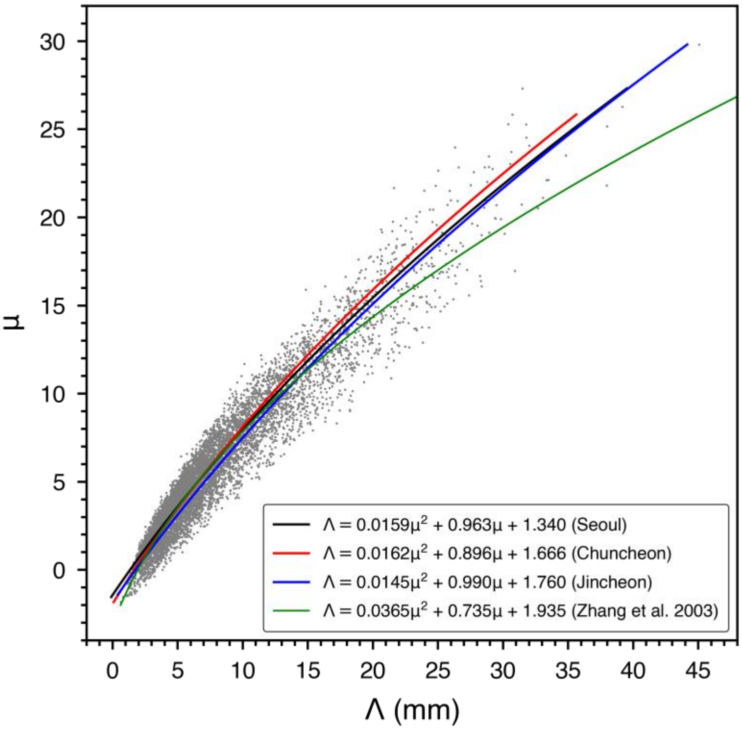

Figure 2.11 Scatter plot of the slope parameter Λ and the shape parameter μ. The black, red, and blue lines represent the second-order polynomial fits for the μ-Λ relation for Seoul, Chuncheon, and Jincheon, respectively. The green line represents the μ-Λ relation obtained in Zhang et al. (2003).

indicates a small spatial variability of the μ–Λ relation within the northern–central region of South Korea. Han et al. (2021) also reported that the μ–Λ relation does not vary much within a small region. Nevertheless, the μ–Λ relations at the three sites deviate much from that in Florida obtained by Zhang et al. (2003), especially for large Λ for which μ at the three sites are noticeably larger than that in Florida. Among the three sites, Jincheon exhibits the smallest μ for a wide range of Λ. Wu et al. (2019) stated that a relatively small μ for a given Λ may result from the a relatively high number concentration of small raindrops, which seems to be the case in Jincheon.

3 Diagnostic relations for the intercept parameter of exponential raindrop size distribution according to rain types derived from disdrometer data and their impacts on precipitation prediction

3.1 Introduction

There are two main methods of explicitly representing cloud microphysical processes in numerical models: the bin microphysics method and the bulk microphysics method. In models with bin microphysics schemes, hydrometeor of any type is subdivided according to its size and the number concentration of the hydrometeor in each size bin is prognostically calculated, thus the hydrometeor size distribution evolves naturally without any constraint. However, because the bin microphysics method requires a vast amount of computational resources (Khain et al. 2015; Lee and Baik 2018; Grabowski et al. 2019), the bulk microphysics method, which is more economical, is commonly employed in weather and climate models. In models with bulk microphysics schemes, hydrometeor of any type is assumed to have a specific particle size distribution such as the exponential, gamma, or lognormal distribution. For example, the exponential size distribution of raindrops is given as

$$N(D) = N_0 \exp(-\Lambda D)\,, \qquad (3.1)$$

where N_0 is the intercept parameter and Λ is the slope parameter of raindrop size distribution (RSD). A well-known exponential distribution is the Marshall-Palmer distribution (Marshall and Palmer 1948), where N_0 is a fixed value of 8000 m^{-3} mm^{-1} and Λ is a function of rain rate. In models with single-moment bulk microphysics schemes, which prognose only hydrometeor mixing ratios, the intercept parameter is usually fixed as in the Marshall-Palmer distribution and the slope parameter is determined by the prognosed rainwater mixing ratio.

The constant-N_0 assumption in single-moment bulk microphysics schemes is different from reality. Many studies have revealed that N_0 or the generalized intercept parameter N_w, which is computed from the rainwater content W and mass-weighted mean raindrop diameter D_m for a size distribution of any form and is identical to N_0 for an exponential size distribution, has a large spatiotemporal variability (Waldvogel 1974;

Uijlenhoet et al. 2003; Loh et al. 2019; Chen et al. 2020; Jwa et al. 2021; Suh et al. 2021). Waldvogel (1974) observed a sudden change in N_0, called the N_0 jump, during orographic precipitation when a convective portion within a precipitation system moved in to or out from a disdrometer site in Locarno, Switzerland. Uijlenhoet et al. (2003) also observed the N_0 jump at a disdrometer site in northern Mississippi, USA, when the transition from stratiform to convective rainfall occurred with the disappearance of the radar bright band. Chen et al. (2020) showed that N_0 and N_w decreased with altitude when landfalling typhoons passed the 356-m high meteorological tower in Shenzhen, China, where disdrometers are mounted at four different altitudes.

The analysis of data from a disdrometer in Seoul, South Korea, shows that N_0 fluctuates with rain rate and that the probability density function (PDF) of N_w have different characteristics depending on the rain type (i.e., stratiform, mixed, or convective) and weather type (Jwa et al. 2021). Suh et al. (2016) analyzed the data from a disdrometer in Busan and showed that the characteristics of N_w vary depending on the rain type and weather type and that N_w has clear seasonal and diurnal variability, which is attributed to changes in wind direction. Loh et al. (2019) compared the data from two disdrometers, one in the central region and the other in the southeastern region of the Korean Peninsula and showed that the mean value of N_w in the central region is larger than that in the southeastern region. Kim et al. (2022)

investigated the microphysical characteristics of orographic rainfall over Mt. Halla where ten disdrometers are installed. They revealed that N_w at windward sites is overall smaller than that at leeward sites. Suh et al. (2021) analyzed data from four disdrometers installed in the southeastern region of the Korean Peninsula at an interval of ~20 km from the coastline to inland. They found that for stratiform rain, multiple peaks are seen in the N_w PDF in the coastal region while they are not seen in the inland area. They also found that for convective rain, the N_w value at which the peak appears decreases with the distance from the coastline.

The N_0 variability can be considered in a model by employing either a multi-moment microphysics scheme or a diagnostic relation for N_0. In models using multi-moment microphysics schemes, two or more moments of RSD are prognosed and N_0 is calculated from the prognosed moments, having a spatiotemporal variability. In models using single-moment microphysics schemes, a diagnostic relation for N_0 is required in order to represent the N_0 variability. There have been proposed several methods to derive a diagnostic relation for N_0 for use in single-moment microphysics schemes (Zhang et al. 2008; Abel and Boutle 2012; Wainwright et al. 2014; Pan et al. 2016). Zhang et al. (2008, Z08 hereafter) proposed the moment relation method, in which it is assumed that two moments of RSD have a power-law relation. Using data from three disdrometers, they derived N_0–W diagnostic relations from the power-law relation between RSD moments and showed that in comparison with the direct fitting of the N_0–W relation, the moment relation method yields smaller biases in diagnosing N_0. Abel and Boutle (2012, AB12 hereafter) derived a power-law relation between N_0 and Λ using RSD data from aircraft, ground-based lidar, and disdrometer observations. Using the derived power-law relation between N_0 and Λ, N_0 is diagnosed from Λ in the Met Office Unified Model (Walters et al. 2019). In addition, there was an approach to obtain an optimal N_0–Λ power-law relation by optimizing the coefficients in the relation using a micro-genetic algorithm and a harmony search algorithm (Jang et al. 2017). Pan et al. (2016) and Wainwright et al. (2014) established N_0–W diagnostic relations using N_0 and W obtained from squall line and tornadic supercell simulations, respectively, that were run using a model with a double-moment microphysics scheme.

The implementation of a diagnostic relation for N_0 can improve the performance of a model with a single-moment microphysics scheme on precipitation prediction. In the numerical simulations of Abel and Boutle (2012), the overprediction of precipitation was reduced due to an increase of evaporation in the sub-cloud layer, which was attributed to the use of a diagnostic relation that represents large N_0 for light rain. Wainwright et al. (2014) evaluated a simulation where a diagnostic relation for N_0 was used by comparing it to a simulation with a double-moment microphysics scheme.

Compared to the simulation using a fixed N_0, the simulation using a diagnostic relation for N_0 yielded the predictions of cold pool size and strength that are more consistent with those in the simulation using a double-moment microphysics scheme.

Each of the aforementioned studies derived a single diagnostic relation for N_0 and applied to the simulations of various types of rain. Considering that the characteristics of N_w are different depending on the rain type (Bringi et al. 2003; Thurai et al. 2016; You et al. 2016; Jwa et al. 2021), the diagnosis of N_0 can be further improved if different diagnostic relations are derived for different rain types, which are done in this study. In addition, in this study, the several derivation methods that were used in previous studies are tested to find out the diagnostic relation for N_0 that best represents the N_0 variability. The derived diagnostic relation for N_0 is used in the simulations of precipitation in South Korea, where the disdrometer sites at which the data used for the derivation were obtained are located, to examine the impacts of the diagnostic relation on regional precipitation prediction.

In subchapter 3.2, the disdrometer data and derivation methods used to obtain the diagnostic relations for N_0 are presented. In that subchapter, the evaluation of the derived diagnostic relations is also given and the most appropriate diagnostic relation is chosen. In subchapter 3.3, the impacts of the diagnostic relations on precipitation prediction are investigated through the simulations of summer precipitation in South Korea. In Chapter 6, a summary and conclusions are given.

3.2 Diagnostic relations for the intercept parameter N_0

3.2.1 Disdrometer data

To derive diagnostic relations for N_0, we collected disdrometer data from four sites in South Korea in 2019. The locations of the four sites are given in Fig. 3.1. The four disdrometers in Seoul, Chuncheon, Jincheon, and Boseong have been operated by the Convection and Urban Meteorology Group of Seoul National University, the Air Quality Prediction Research Laboratory of Kangwon National University, the Weather Radar Center of Korean Meteorological Administration, and the National Institute of Meteorological Sciences of Korean Meteorological Administration, respectively. At all sites, the same type of disdrometer, Parsivel^2, is used. The Parsivel^2 disdrometer measures the diameter and fall speed of hydrometeors and classifies them into 32 × 32 bins of diameter and fall speed with non-uniform intervals (Tokay et al. 2014). The fall speed range is 0–22.4 m s^{-1}. The diameter range is 0.25–26 mm, and it is 0.25–8 mm for liquid precipitation. The two smallest diameter bins (0–0.25 mm) are excluded

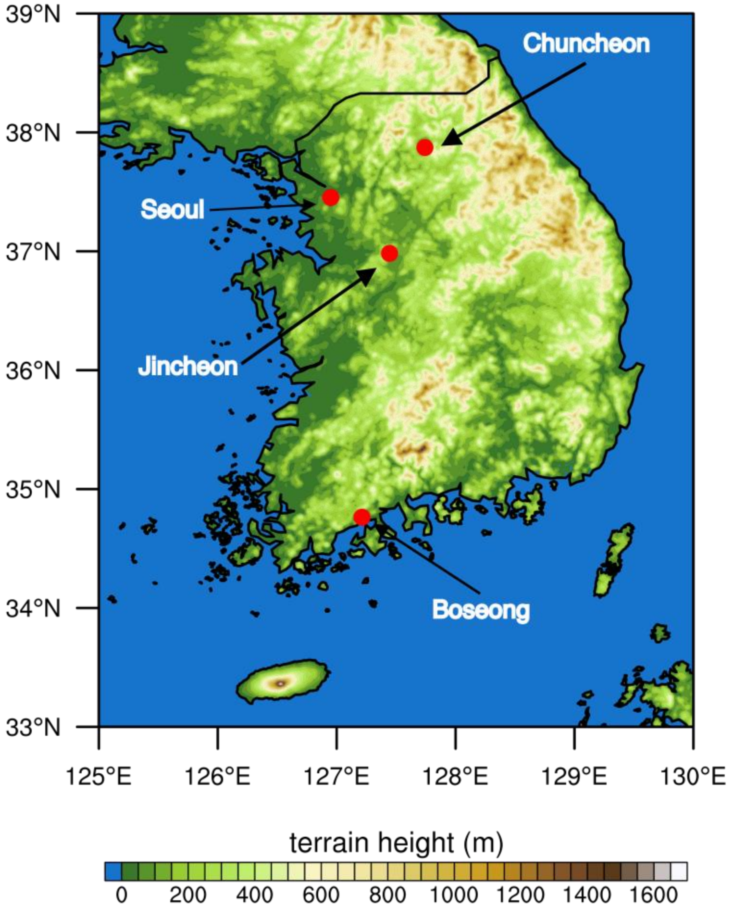

Figure 3.1 Locations of four disdrometers (red circles) on the topographic map of South Korea and surrounding regions (shaded).

because of the low signal-to-noise ratio. The data sampling interval is 1 minute. In this study, only liquid precipitation is considered. The quality control of the disdrometer data is conducted following Jwa et al. (2021). After the quality control, a total of 75,978 1-minute data remain and are used for the derivation of diagnostic relations for N_0.

Figure 3.2 shows the box plots of N_0 estimated from the disdrometer data at the four sites for four seasons. The number of data for each site and season is also shown in this figure. Fall, summer, and spring account for large portions of the data, while winter does not. In the three seasons, the numbers of data at the four sites are similar to each other, except for Boseong in spring and Chuncheon in summer. The temporal and spatial variabilities of N_0 are revealed well in this figure. For the total data from all four sites, the median of N_0 for spring is 9,406 m^{-3} mm^{-1}, which is larger than those for summer (6,676 m^{-3} mm^{-1}) and fall (5,149 m^{-3} mm^{-1}), which shows the seasonal variability of N_0. The ranges between the 5th and 95th percentiles of N_0 for spring, summer, and fall are 1,724–56,741, 1,413–51,695, and 1,410–33,114 m^{-3} mm^{-1}, respectively. This shows that N_0 significantly varies within the same season. The median of N_0 also differs depending on the site. In summer, for example, the medians of N_0 for Seoul, Chuncheon, Jincheon, and Boseong are 6,883, 4,603, 8,307, and 7,553 m^{-3} mm^{-1}, respectively. The large temporal and spatial variabilities of N_0 revealed in the disdrometer observations suggest

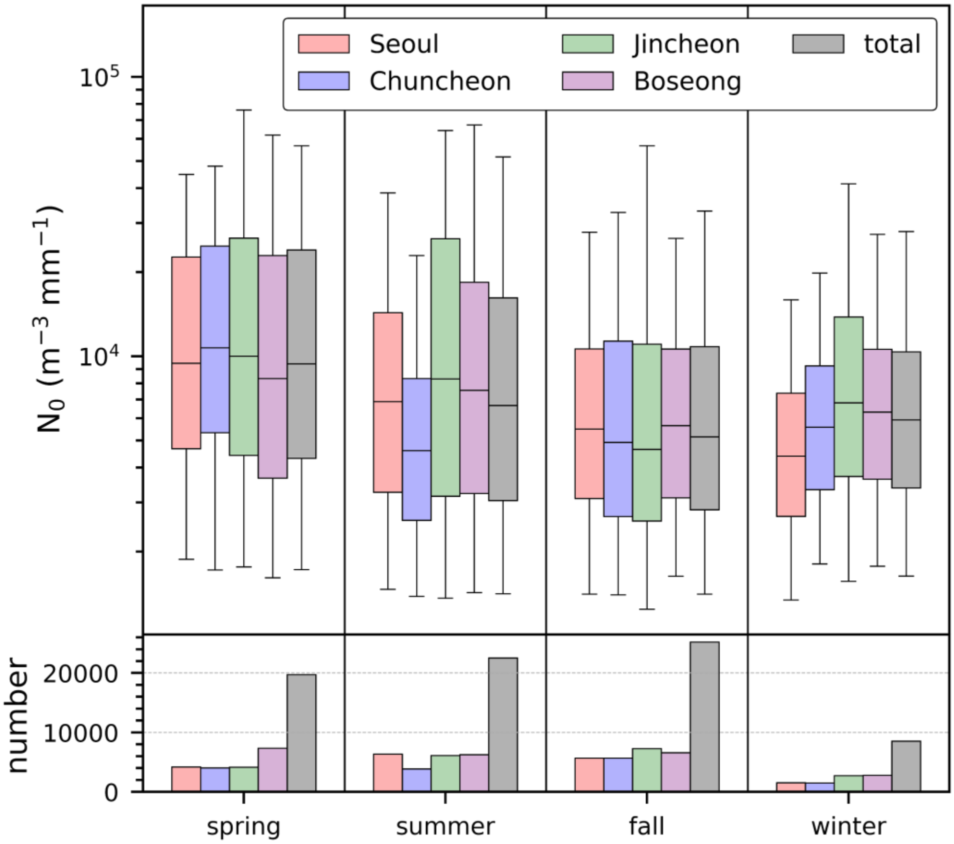

Figure 3.2 Box plots of the intercept parameter N_0 estimated from the disdrometer data at the four sites and the total data for four seasons. The lower boundary, centerline, and upper boundary of boxes indicate the lower quartile, median, and upper quartile, respectively. The lower and upper whiskers represent the 5th and 95th percentiles, respectively. The number of each dataset is shown at the bottom.

that single-moment microphysics schemes in numerical models should not use the constant N_0 and allow N_0 to change with time and space.

3.2.2 Review of the derivation methods of diagnostic relations

To diagnose N_0 for single-moment microphysics schemes, N_0 should be expressed as a function of any variable such as the rainwater content W. In this study, we derive the N_0–W diagnostic relations using three different methods proposed by previous studies (Zhang et al. 2008; Abel and Boutle 2012). For each method, we derive three diagnostic relations for different rain types, which was not done in the previous studies.

In the first method, the diagnostic relation between N_0 and W is determined by the direct fitting of the relation between N_0 and W estimated from the disdrometer data (Zhang et al. 2008). The nth moment of RSD is expressed as follows:

$$M_n = \int D^n N(D)\, dD \quad (3.2)$$

For the exponential RSD, Eq. (3.2) is expressed as

$$M_n = N_0 \Lambda^{-(n+1)} \Gamma(n+1), \tag{3.3}$$

where Γ is the gamma function. W is expressed as

$$W = \frac{\pi}{6} \rho_w M_3, \tag{3.4}$$

where ρ_w is the liquid water density. Following Zhang et al. (2008), the second and fourth moments of RSD are used to obtain Λ and N_0 as follows:

$$\Lambda = \left[\frac{M_2 \Gamma(5)}{M_4 \Gamma(3)} \right]^{\frac{1}{2}}, \tag{3.5}$$

$$N_0 = \frac{M_2 \Lambda^3}{\Gamma(3)}. \tag{3.6}$$

Based on N_0 and W estimated from the disdrometer data, the following power-law relation is obtained by a linear least-squares fitting for the logarithms of N_0 and W:

$$N_0 = \alpha_1 W^{\beta_1}. \tag{3.7}$$

Then, the coefficients α_1 and β_1 are determined.

In the second method, the diagnostic relation between N_0 and W is determined from the fitted N_0–Λ relation (Abel and Boutle 2012). Based on N_0 and Λ estimated from the disdrometer data, the power-law relation of N_0–Λ is obtained by a linear least-squares fitting for the logarithms of N_0 and Λ:

$$N_0 = a_2 \Lambda^{b_2} \, . \tag{3.8}$$

Substituting Eq. (3.3) for M_3 into Eq. (3.4) gives the relation between Λ and W:

$$\Lambda = \left(\frac{\pi \rho_w N_0}{W} \right)^{\frac{1}{4}} , \tag{3.9}$$

By substituting this relation into Eq. (3.8), the N_0–W diagnostic relation from the fitted N_0–Λ relation is obtained as follows:

$$N_0 = \alpha_2 W^{\beta_2} , \tag{3.10}$$

where

$$\alpha_2 = a_2^{\frac{4}{4-b_2}} (\pi\rho_w)^{\frac{-b_2}{b_2-4}}, \tag{3.11}$$

$$\beta_2 = \frac{b_2}{b_2 - 4}. \tag{3.12}$$

The third method to derive the diagnostic relation between N_0 and W is the moment relation method proposed by Zhang et al. (2008). Based on two different moments of RSD estimated from the disdrometer data, the power-law relation of the two moments is obtained by a linear least-squares fitting for the logarithms of the two moments:

$$M_l = a_3 M_m^{\ b_3}. \tag{3.13}$$

Substituting Eq. (3.3) into Eq. (3.13) and combining this equation with Eq. (3.9) gives the N_0–W diagnostic relation as follows:

$$N_0 = \alpha_3 W^{\beta_3}, \tag{3.14}$$

where

$$\alpha_3 = \left[a_3 \frac{\Gamma^{b_3}(m+1)}{\Gamma(l+1)\pi^c \rho_w{}^c} \right]^{\frac{1}{1-b_3+c}}, \tag{3.15}$$

$$\beta_3 = \frac{c}{1-b_3+c}, \tag{3.16}$$

$$c = \frac{b_3(m+1)-(l+1)}{4}. \tag{3.17}$$

Note that $(l, m) = (2, 4)$ is used in this study. Hereafter, the diagnostic relation for N_0 derived by the direct fitting of the relation between N_0 and W is called DNW, and those derived using the N_0–Λ relation and M_2–M_4 relation are called DNL and DMM, respectively.

Many observational studies have shown that the characteristics of N_w differ depending on the rain type (Janapati et al. 2017; Seela et al. 2018; Lee et al. 2019; Jwa et al. 2021). To better represent the variability of the intercept parameter, the disdrometer data are divided into three rain types and then the aforementioned derivation methods are applied for each rain type. Tokay and Short (1996) showed that when the rain rate is lower (higher) than 1 (10) mm h^{-1}, stratiform (convective) rain is dominant and when the rain rate is between 1 and 10 mm h^{-1}, both rain types appear with similar frequency. Thus, we adopted the above criteria to classify the disdrometer data into stratiform, mixed, and convective rain, respectively, and a diagnostic relation for N_0 is derived for each rain type. The coefficients and exponents of the derived diagnostic relations for total, stratiform, mixed, and convective rain are given in Table 3.1.

3.2.3 Evaluation of the derived relation

Figure 3.3 shows the density scatter plots of N_0 and W estimated from the disdrometer data for the three rain types and the total. For each rain type and the total, three N_0–W diagnostic relations derived using different methods are presented. Stratiform, mixed, and convective rain account for 47% (35,752), 49% (37,369), and 4% (2,857) of the total data (75,978), respectively. The estimated N_0 mostly ranges within 864–83,837 m^{-3} mm^{-1} for total, 1,180–85,012 m^{-3} mm^{-1} for stratiform rain, 731–84,152 m^{-3} mm^{-1} for mixed rain, and 706–29,142 m^{-3} mm^{-1} for convective rain, where the numbers are the 1st and 99th percentiles. For each of the total and three rain types, N_0 diagnosed by DNW and DMM stays within the 1st–99th percentile range of estimated N_0 for a wide range of W, while N_0 diagnosed by DNL stays within this range for only a limited range of W. The diagnostic relations derived from the same method show a consistent tendency for the different rain types and total. In DNW, N_0 increases as W increases, but in DNL and

Table 3.1 Coefficients α_i and β_i in the derived diagnostic relations for total, stratiform, mixed, and convective rain

	DNW		DNL		DMM	
	α_1	β_1	α_2	β_2	α_3	β_3
total	8434	0.071	531	−1.085	4807	−0.166
stratiform	22502	0.327	1.320×10^{-2}	−4.103	2278	−0.389
mixed	22555	0.746	2.022×10^{-5}	−11.066	4434	−0.209
convective	6696	0.365	6522	−3.090	6799	−0.205

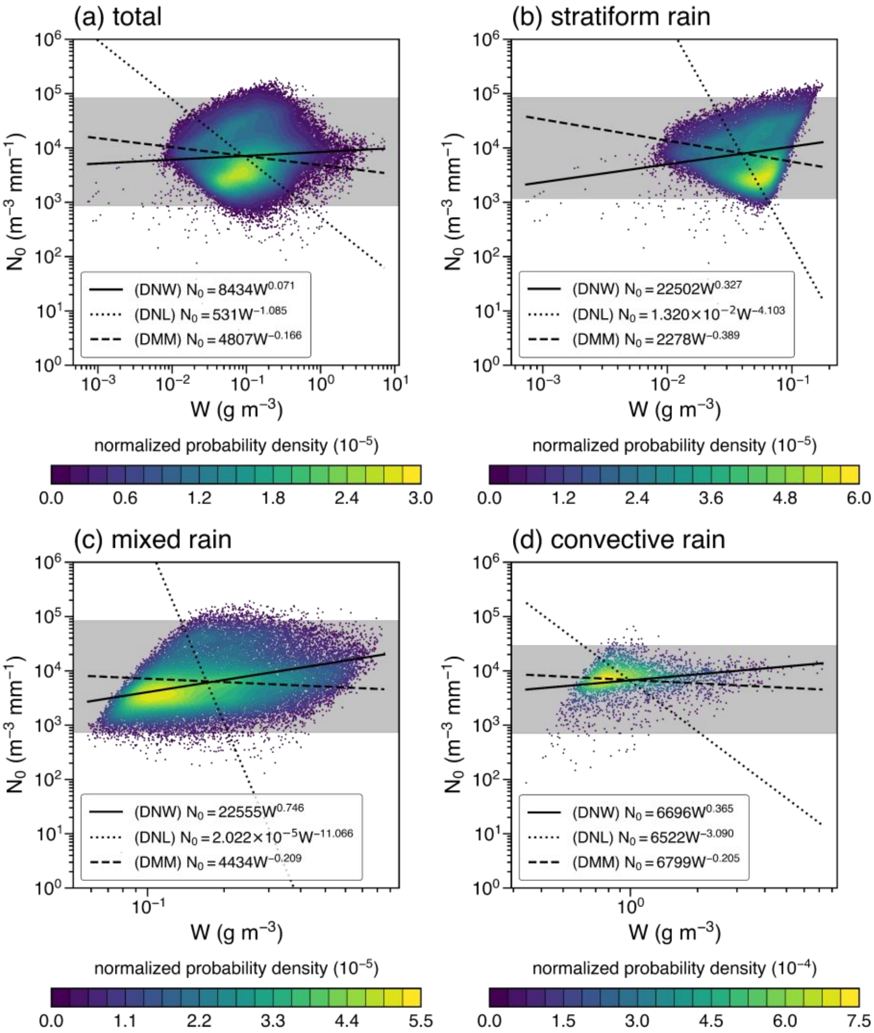

Figure 3.3 Density scatter plots of the intercept parameter N_0 and the rainwater content W estimated from the disdrometer data for (a) total, (b) stratiform rain, (c) mixed rain, and (d) convective rain. The solid, dotted, and dashed lines indicate DNW, DNL, and DMM, respectively. The gray shaded area represents the range between the 1st and 99th percentiles of N_0.

DMM, N_0 decreases as W increases. The exponent values of the diagnostic relations show that the slope of the diagnostic relation derived from each method is steeper for the individual rain types than for the total data. For example, DNW has an exponent value of 0.071 for the total data, which indicates a very weak dependency of N_0 on W, while it has larger values of exponent (0.327, 0.746, and 0.365 for stratiform, mixed, and convective rain, respectively) for individual rain types. This indicates that using different diagnostic relations according to the rain type improves the representation of the dependency of N_0 on W.

Depending on the method used to derive the diagnostic relation, the rain type that shows the largest variation of diagnosed N_0 changes. For example, for DNW and DNL, the largest variation of diagnosed N_0 appears in mixed rain, while it appears in stratiform rain for DMM. According to Tokay and Short (1996), the rain rate range of 1–10 mm h^{-1} is the range where convective and stratiform rain occur in similar frequency so that the N_0 jump is most important, which indicates that the N_0 variation is large for this rain rate range. Given that this rain rate range is classified as mixed rain in this study, DNW and DNL well reflect the characteristics of mixed rain. In addition, Tokay and Short (1996) showed that N_0 increases when W increases for the rain rate of 5 mm h^{-1}, and only DNW shows an increasing tendency of diagnosed N_0 with W for mixed rain.

To further evaluate the diagnostic relations, the density scatter plots of N_0 diagnosed from the diagnostic relations against N_0 estimated from the disdrometer data are plotted (Fig. 3.4). In Fig. 3.4a–c, the diagnosed N_0 obtained without the rain-type classification is compared to the estimated N_0. N_0 diagnosed by DNW and DMM is concentrated near 8,000 m^{-3} mm^{-1}, which is the value of N_0 of the Marshall-Palmer distribution. The standard deviations of the N_0 diagnosed by DNW and DMM are relatively small (523 and 1,189 m^{-3} mm^{-1}, respectively) compared to that of estimated N_0 (16,803 m^{-3} mm^{-1}). As a result, the correlation coefficient R is close to zero for both diagnostic relations, indicating that DNW and DMM without the rain-type classification can hardly reproduce the variation of the estimated N_0. On the other hand, the standard deviation of the N_0 diagnosed by DNL is 18,082 m^{-3} mm^{-1}, similar to that of estimated N_0. However, R is negative, showing DNL's poor capability of reproducing the estimated N_0.

In Fig. 3.4d–f, the diagnosed N_0 obtained with the rain-type classification is compared to the estimated N_0. Compared to the diagnosed N_0 obtained without the rain-type classification, that obtained with the rain-type classification shows larger standard deviations of diagnosed N_0, which are 2,401, 5.709×10^8, and 1,624 m^{-3} mm^{-1} for DNW, DNL, and DMM, respectively. For N_0 diagnosed by DNW, R increases from 0.08 to 0.24 as the rain-type classification is considered (Fig. 3.4a and d). The rain-type

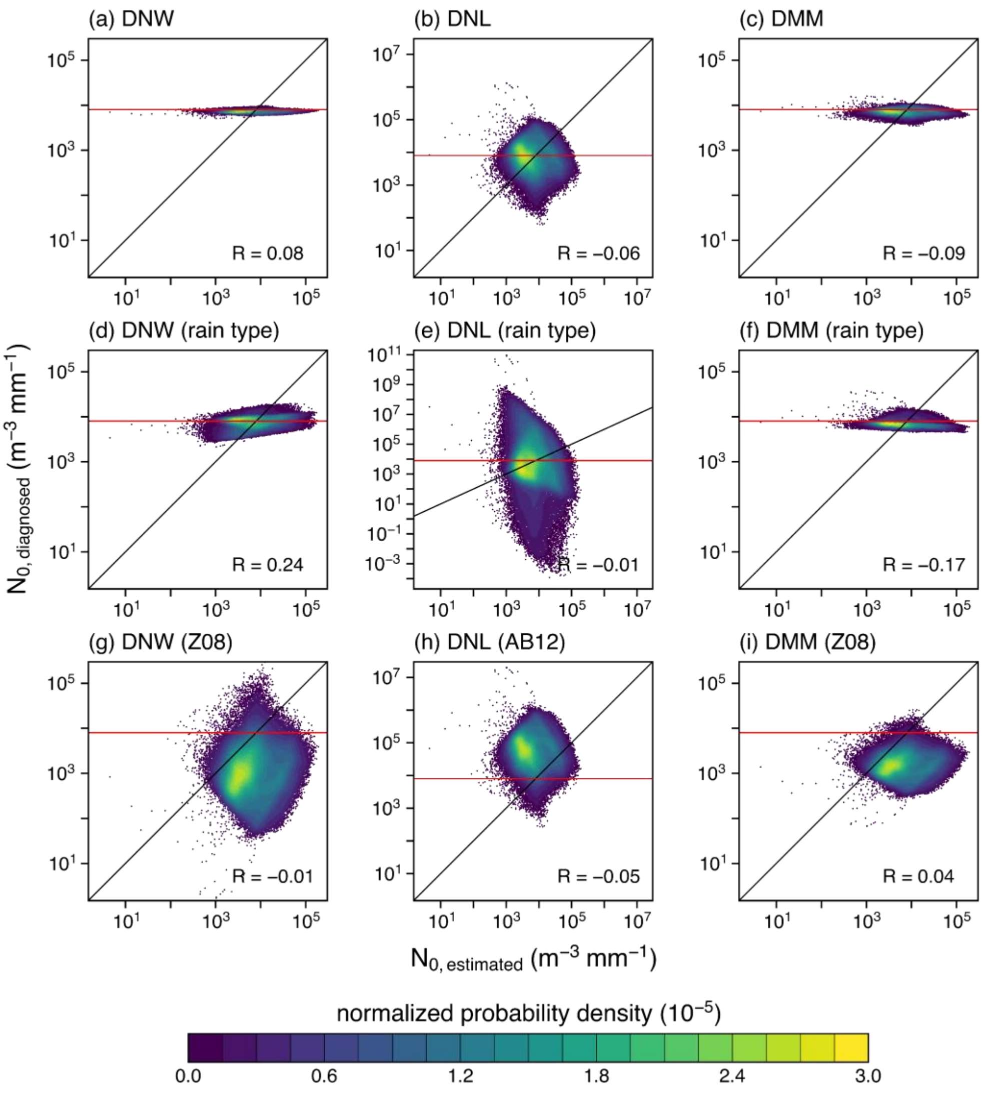
(a) DNW
(b) DNL
(c) DMM
(d) DNW (rain type)
(e) DNL (rain type)
(f) DMM (rain type)
(g) DNW (Z08)
(h) DNL (AB12)
(i) DMM (Z08)
R = 0.08
R = −0.06
R = −0.09
R = 0.24
R = −0.01
R = −0.17
R = −0.01
R = −0.05
R = 0.04
$N_{0,\,diagnosed}$ (m^{-3} mm^{-1})
$N_{0,\,estimated}$ (m^{-3} mm^{-1})
normalized probability density (10^{-5})
0.0
0.6
1.2
1.8
2.4
3.0

Figure 3.4 Density scatter plots of the intercept parameter estimated from the disdrometer data, $N_{0,\mathrm{estimated}}$, and the intercept parameter diagnosed from the diagnostic relations, $N_{0,\mathrm{diagnosed}}$, for different diagnostic relations (a–c) derived without the rain-type classification, (d–f) derived with the rain-type classification, and (g–i) provided by the previous studies. The probability density is normalized by the maximum probability density. The black line represents the identity line, and the red line represents the value of N_0 of the Marshall-Palmer distribution (8,000 $\mathrm{m}^{-3}\ \mathrm{mm}^{-1}$). R in each subfigure stands for the correlation coefficient.

classification makes it possible to diagnose a wider range of N_0. For N_0 diagnosed by DNL, R is still negative despite the consideration of the rain-type classification (Fig. 3.4b and e). In addition, DNL with the rain-type classification yields too much dispersion of diagnosed N_0. Because DNL without the rain-type classification already diagnoses a sufficiently wide range of N_0, the rain-type classification causes DNL to diagnose an unrealistically wide range of N_0. For N_0 diagnosed by DMM, the diagnosed and estimated N_0 become even more negatively correlated when the rain-type classification is applied to the diagnostic relation (Fig. 3.4c and f).

In Fig. 3.4g–i, the diagnosed N_0 using the diagnostic relations of the previous studies (Z08 and AB12) is compared to the estimated N_0. Z08 derived DNW ($N_0 = 24144W^{1.326}$ m^{-3} mm^{-1}) and DMM ($N_0 = 7106W^{0.648}$ m^{-3} mm^{-1}) using the RSD data of summertime rainfall in Oklahoma, and AB12 derived DNL ($N_0 = 3018W^{-1.222}$ m^{-3} mm^{-1}) using the RSD data collected from various field campaigns and disdrometer observations around the world. When applied to diagnose N_0 in South Korea, DNW and DMM of Z08 overall underdiagnose N_0, whereas DNL of AB12 overdiagnoses N_0. All the three diagnostic relations of the previous studies show R close to zero, suggesting that a diagnostic relation obtained using the RSD data of one region may not perform well in another region. In other words, to improve precipitation prediction of a numerical model in one region, a diagnostic relation that is derived using the RSD data of that region should be applied.

Based on the evaluation of different diagnostic relations so far, DNW with the rain-type classification is selected as the diagnostic relation to be implemented into a single-moment microphysics scheme in a numerical model to improve precipitation prediction. The reasons are as follows: 1) With or without the rain-type classification, N_0 diagnosed by DNL and DMM are negatively correlated with the estimated N_0, which means that they tend to diagnose N_0 inversely. 2) The rain-type classification improves the capability of DNW to reproduce the wide range of estimated N_0 and strengthens the correlation between the diagnosed and estimated N_0.

3.3 Impacts of the derived diagnostic relation on precipitation prediction

3.3.1 Model description and simulation setup

The Weather Research and Forecasting (WRF) model version 4.2 (Skamarock et al. 2019) is used in this study. Figure 3.5 shows the model domain configuration. Three one-way nested domains centered on South Korea are considered. The horizontal grid spacings (numbers) of domains 1, 2, and 3 are 27 (150×120), 9 (217×184), and 3 km (253×244), respectively. For all domains, the number of vertical layers is 49 and the vertical grid

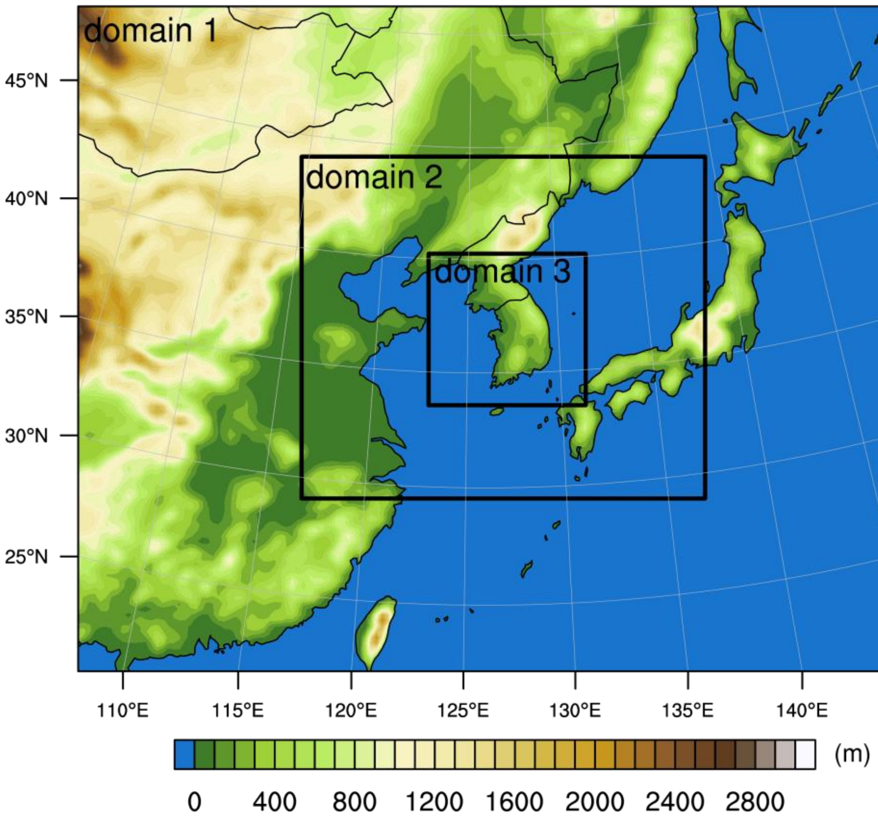

Figure 3.5 Model domain configuration. The shades represent the terrain height.

spacing is stretched from ~60 m in the lowest layer to ~450 m in the highest layer. The height of the model top is 50 hPa (~20 km). The fifth generation of reanalysis data from the European Centre for Medium-Range Weather Forecasts (ERA5, Hersbach et al. 2020) with 1-h temporal resolution and 0.25°×0.25° horizontal resolution are used as initial and boundary conditions. The physical parameterizations used in this study are the WRF single-moment 6-class (WSM6) cloud microphysics scheme (Hong and Lim 2006), the Kain–Fritsch cumulus parameterization scheme (Kain 2004), the Yonsei University PBL scheme (Hong et al. 2006), the revised MM5 surface layer scheme (Jiménez et al. 2012), the unified Noah land surface model (Tewari et al. 2004), the Dudhia shortwave radiation scheme (Dudhia 1989), and the Rapid Radiative Transfer Model (RRTM) longwave radiation scheme (Mlawer et al. 1997). The cumulus parameterization scheme is not applied to the innermost domain.

The diagnostic relation for N_0 selected in subchapter 3.1.3 is implemented into the WSM6 cloud microphysics scheme. The diagnostic relation requires two information: the rain type and the rainwater content W. In this study, the rain type of any column where rainwater exists is determined by the surface rain rate if it is not zero or the rain rate at the lowest level at which rainwater exists if the surface rain rate is zero. The rain rate criteria used to determine the rain type are the same as those used for the rain-type classification in subchapter 3.1.3. W used in the diagnostic relation can be determined by two different ways. One way is to use W at each level (Option E). This gives different diagnoses of N_0 at different levels because W varies within a column. The other way is to use W at the lowest level of its presence (Option L). In this way, a column is assigned a single value of N_0. Because the two options are expected to cause some differences in precipitation prediction, they are both tested in the precipitation simulations in this study.

In this study, we simulate the precipitation events that occurred in South Korea during the 7-day period from 12 UTC 27 July to 12 UTC 3 August 2020 when the Changma front, a quasi-stationary front that forms during the East Asian summer monsoon, affected South Korea. The model is initialized every day at 00 UTC and integrated for 36 h, and the first 12 h is considered as a spin-up time. Three sets of simulations are conducted, one with the original WSM6 scheme (WSM6-O simulation) and the other two with the WSM6 scheme where the diagnostic relation for N_0 is implemented with Option E (WSM6-E simulation) and Option L (WSM6-L simulation), respectively. The analysis of the simulation results is done for the innermost domain.

3.3.2 Evaluation of the simulations with different

methods of applying the diagnostic relation

The 7-day precipitation amounts from rain gauge observation and predicted in the WSM6-O, WSM6-E, and WSM6-L simulations are shown in Fig. 3.6. For each set of simulations, the 7-day accumulated precipitation amount is calculated by summing up the last 24-h accumulated precipitation amounts of the 7 simulations. During the 7-day period, a large amount of precipitation was observed in the region at ~37°N that is elongated in the west–east direction. The precipitation in the west part of this region is not predicted well in all three simulations. The precipitation in the east part of this region is predicted by the three simulations, but their predictions show large differences. The WSM6-O simulation predicts the precipitation in this region, but with a much smaller amount (local maximum: 415 mm) than the observed amount (local maximum: 569 mm). The maximum precipitation amount in the WSM6-O simulation (454 mm) is found further away to the south at ~36.3°N, not in this region. The WSM6-E simulation predicts a larger amount of precipitation in this region (local maximum: 527 mm) compared to the WSM6-O simulation, but it is still smaller than the observation. The WSM6-L simulation predicts an even larger amount of precipitation in this region (local maximum: 566 mm), which is close to the observation.

To quantitatively compare the performances of the three simulations

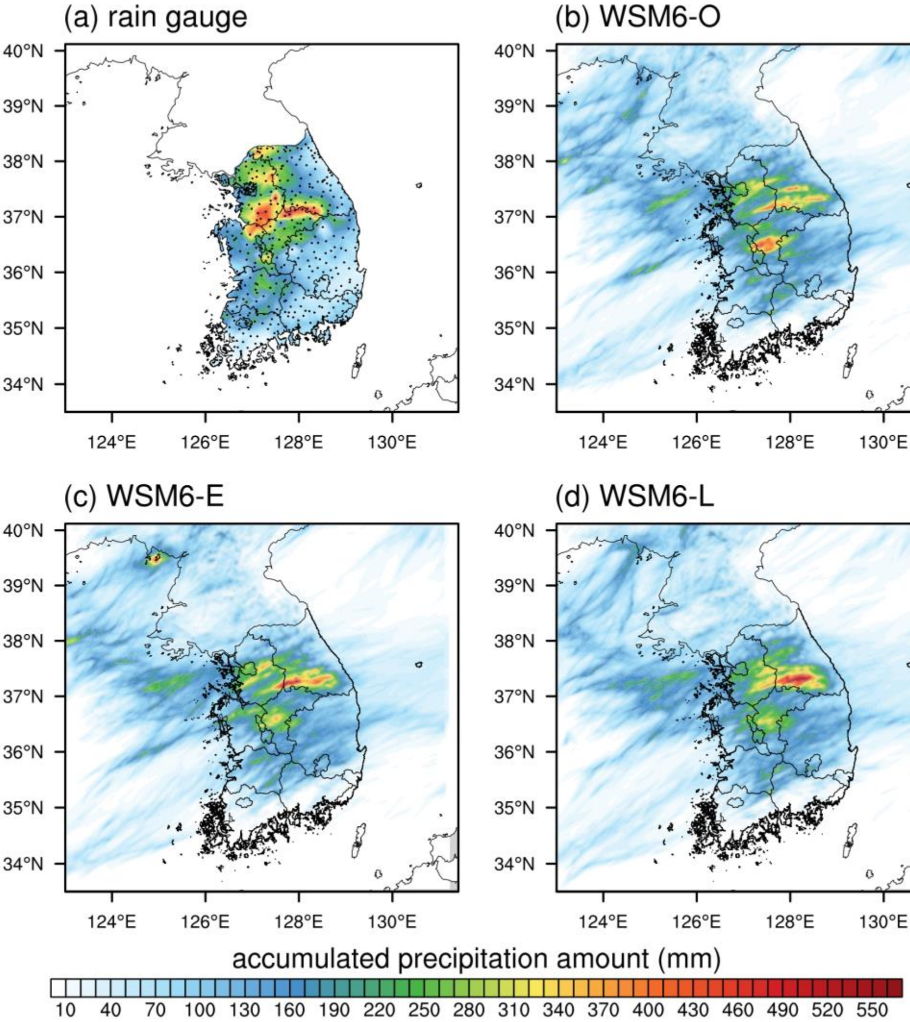

Figure 3.6 Seven-day accumulated precipitation amount (a) observed at 561 rain gauge stations (marked with black dots in (a)) and predicted in the (b) WSM6-O, (c) WSM6-E, and (d) WSM6-L simulations.

and select the better option for applying the diagnostic relation for N_0 to the WSM6 scheme, the root mean squared error (RMSE) and the correlation coefficient R are calculated. The WSM6-L simulation shows the smallest RMSE (89 mm), followed by the WSM6-O (91 mm) and WSM6-E (94 mm) simulations. Also, the WSM6-L simulation shows the highest value of R (0.62), followed by the WSM6-O (0.60) and WSM6-E (0.58) simulations. Applying the diagnostic relation for N_0 with Option L improves the precipitation prediction, while that with Option E degrades the precipitation prediction.

The WSM6-L simulation shows the best performance not only for the 7-day accumulated precipitation amount but also for individual daily precipitation amounts. RMSEs in the WSM6-O, WSM6-E, and WSM6-L simulations are 36, 36, and 34 mm, respectively, and R in these simulations are 0.45, 0.44, and 0.48, respectively. For the prediction of daily precipitation amounts, the performances of the WSM6-O and WSM6-E simulations are similar to each other. Also, when the evaluation indices above are calculated based on hourly precipitation amounts, the WSM6-L simulation gives a smaller RMSE (4.61 mm) than the WSM6-O (4.64 mm) and WSM6-E (4.63 mm) simulations, and a higher value of R (0.17) than the two simulations (0.15 for both WSM6-O and WSM6-E). The equitable threat scores (ETSs) calculated using daily precipitation amounts and hourly precipitation amounts are presented in Fig. 3.7a and b, respectively. Compared to the WSM6-O simulation, both ETSs are improved for almost all precipitation amount thresholds in the WSM6-L simulation. In the WSM6-E simulation, however, ETSs are improved only for a limited range of precipitation amount threshold (10–55 mm for daily precipitation amounts; 4–8 mm and 30–40 mm for hourly precipitation amounts) compared to the WSM6-O simulation. These results suggest that the impacts of applying the diagnostic relation for N_0 can be sensitive to how it is applied at upper levels where N_0 cannot be directly evaluated. Figuring out which option is more realistic at upper levels deserves investigation using RSD observation data at different altitudes, which cannot be done in this study. In this study, based on the quantitative evaluations for the simulated precipitation amounts at the surface, Option L is selected as the option for applying the diagnostic relation for N_0 to the WSM6 scheme.

3.3.3 Impacts of the diagnostic relation on cloud microphysical characteristics

In this subchapter, the WSM6-L simulation is compared with the WSM6-O simulation to examine the impacts of the diagnostic relation for N_0 on the prediction of cloud and precipitation characteristics. In Fig. 3.8, N_0 and Λ in the WSM6-O and WSM6-L simulations are evaluated in comparison

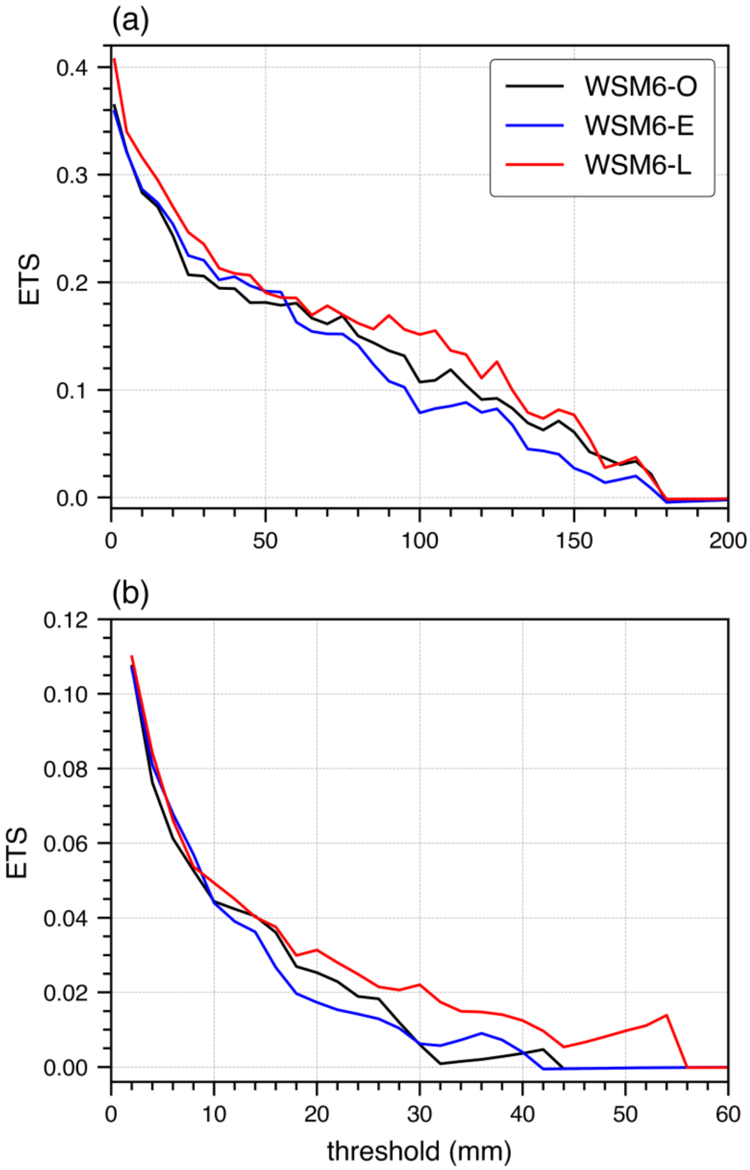

Figure 3.7 Equitable threat scores for (a) daily precipitation amounts and (b) hourly precipitation amounts in the WSM6-O, WSM6-E, and WSM6-L simulations.

with N_0 and Λ from the disdrometer observation. N_0 and Λ at the lowest level at the model grid points closest to each of the four disdrometer sites are compared to those estimated from the disdrometer data of the four sites during the seven-day period. The range between the 1st and 99th percentiles of predicted N_0 in the WSM6-L simulation is 2,583–13,542 m^{-3} mm^{-1}. Although this range is narrower than that of the observed N_0 (654–43,845 m^{-3} mm^{-1}), the representation of N_0 is substantially improved compared to the WSM6-O simulation where N_0 is fixed at 8000 m^{-3} mm^{-1}. Furthermore, the WSM6-L simulation predicts that the peak of PDF appears at N_0 ~ 6000 m^{-3} mm^{-1}, which is very close to the observation. The WSM6-O simulation predicts Λ in a much broader range compared to the observation. Especially, the WSM6-O simulation predicts the occurrence of Λ greater than 9 mm^{-1} which does not appear in the observation. In the WSM6-L simulation, the upper limit of simulated Λ decreases so that the PDF of simulated Λ becomes more similar to that of the observed Λ. However, discontinuities of PDF that does not appear in the observation appear at Λ ranges of 2.4–3.0 and 3.6–4.2 mm^{-1}. This is caused by the rain-type classification in the diagnostic relation. The left, middle, and right parts of the Λ PDF in the WSM6-L simulation are from convective, mixed, and stratiform rain, respectively, in this simulation.

The vertical profiles of $\log_{10}N_0$ and Λ in the WSM6-O and WSM6-L

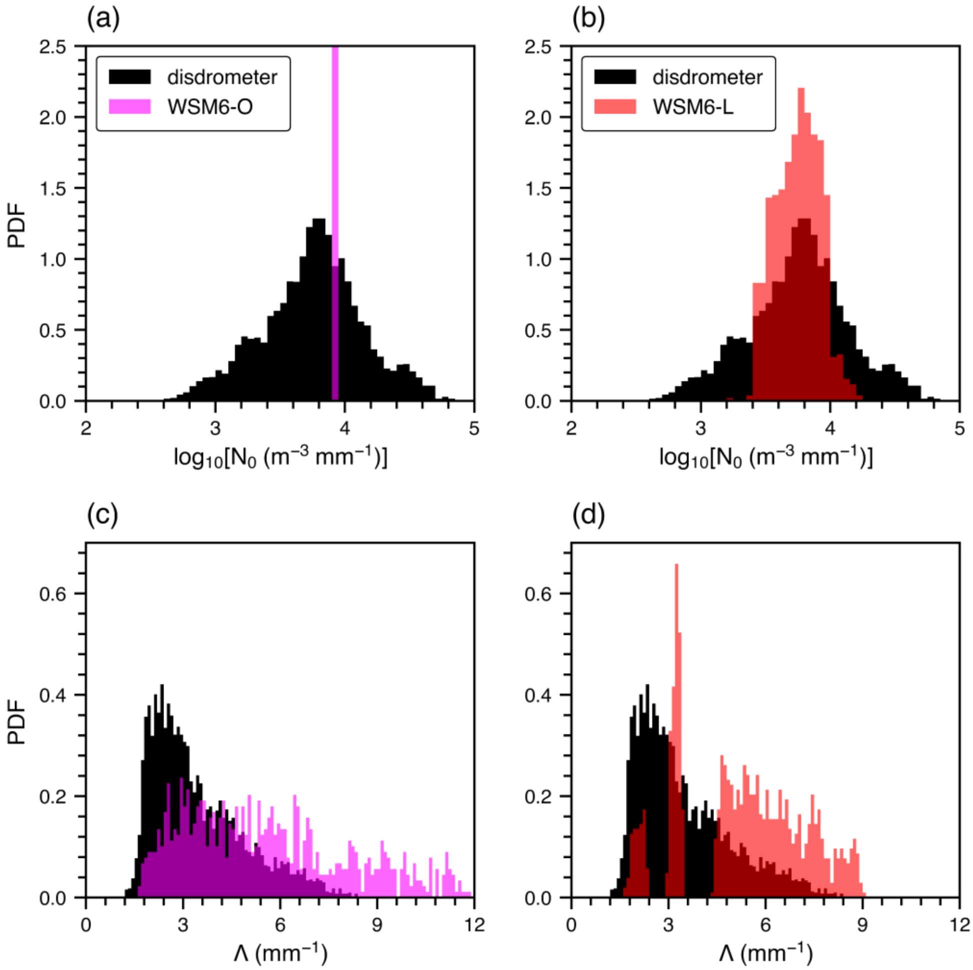

Figure 3.8 Probability density functions (PDFs) for (a, b) the logarithm of the intercept parameter N_0 and (c, d) the slope parameter Λ estimated from the disdrometer data and obtained from the (a, c) WSM6-O and (b, d) WSM6-L simulations.

simulations are compared in Fig. 3.9, where N_0 and Λ are time- and domain-averaged. The average N_0 in the WSM6-L simulation is smaller than that in the WSM6-O simulation at almost all heights, up to ~8.5 km. The difference in the average N_0 is prominent below z ~ 4.5 km, and N_0 at these levels is 2,846 m^{-3} mm^{-1} on average in the WSM6-L simulation. The WSM6-L simulation also shows smaller average Λ compared to the WSM6-O simulation. The average Λ below z = 4.5 km is 10.1 mm^{-1} in the WSM6-L simulation and 15.9 mm^{-1} in the WSM6-O simulation. Because the average W in the WSM6-L simulation is almost the same as that in the WSM6-O simulation (not shown), the relatively small average N_0 and Λ in the WSM6-L simulation suggest that on average, the RSD in the WSM6-L simulation consists of a larger number of large-size raindrops and a smaller number of small-size raindrops than the RSD in the WSM6-O simulation.

Figure 3.10 presents the time- and domain-averaged vertical profiles of the hydrometeor mixing ratios obtained from the WSM6-O and WSM6-L simulations and their differences. In both simulations, the proportion of the mixing ratio of each hydrometeor to the total is almost the same (Fig. 3.10a and b). In both simulations, the mixing ratio of snow accounts for the largest proportion of 35% to the total and the sum of the mixing ratios of ice hydrometeors accounts for 69% of the total. This indicates that ice microphysical processes are highly involved. The rainwater mixing ratios in

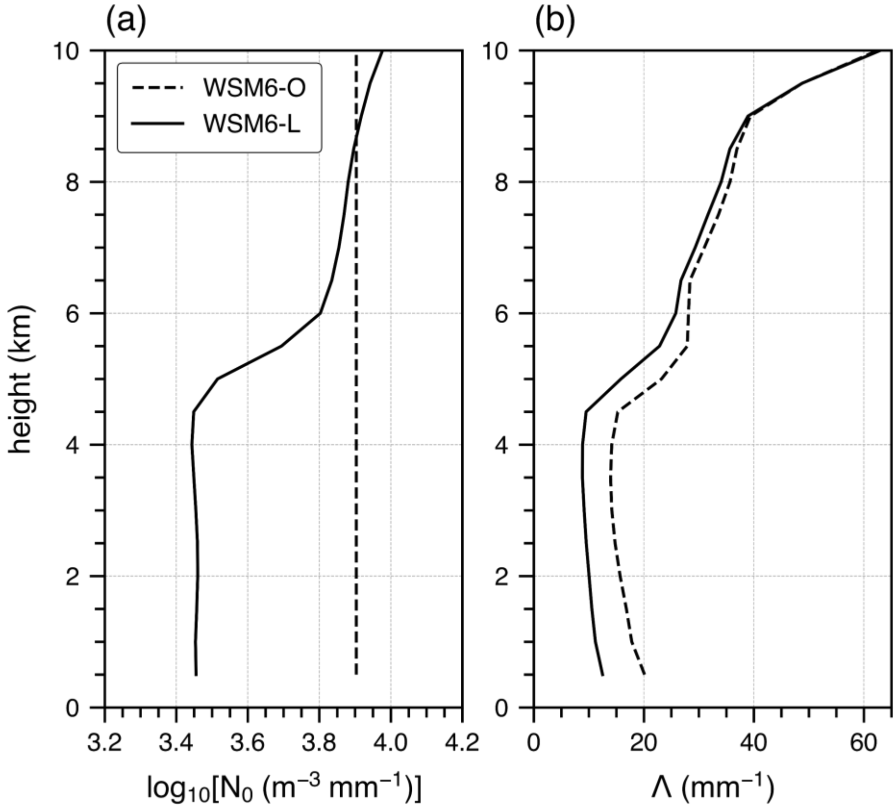

Figure 3.9 Vertical profiles of (a) the logarithm of the intercept parameter N_0 and (b) the slope parameter Λ. N_0 and Λ are time- and domain-averaged.

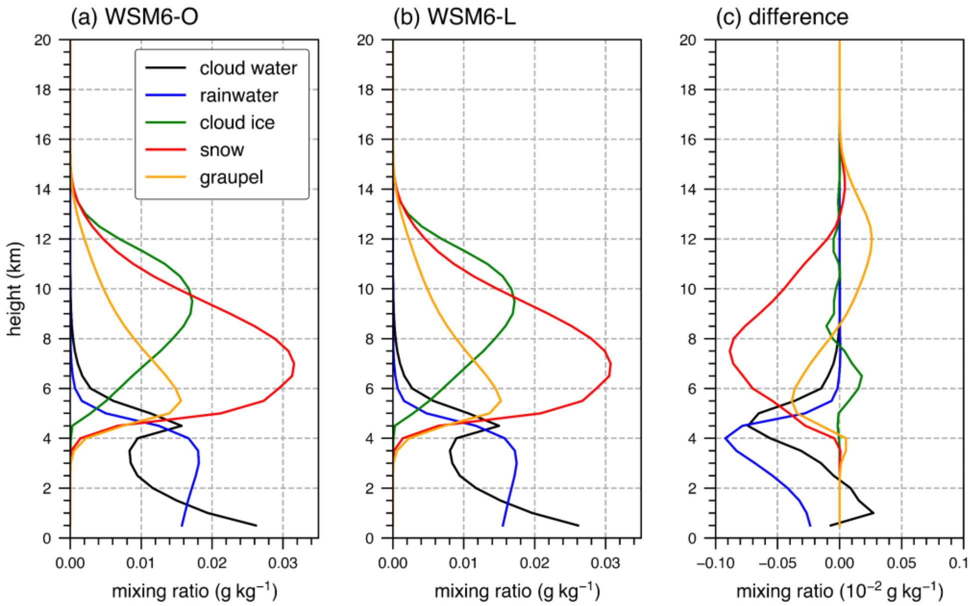

Figure 3.10 Time- and domain-averaged vertical profiles of hydrometeor mixing ratios obtained from the (a) WSM6-O and (b) WSM6-L simulations and (c) their differences (WSM6-L minus WSM6-O).

both simulations have almost identical vertical profiles that show a peak at z = 3.5 km. Compared to the WSM6-O simulation, the rainwater mixing ratio in the WSM6-L simulation is smaller at almost all levels, overall by 3%. The reduction of the rainwater mixing ratio is largest at z = 4 km, below the melting layer. The WSM6-L simulation also shows smaller cloud water mixing ratio except for below z ~ 2 km. The cloud ice mixing ratio is slightly larger at z ~ 5–8 km and smaller above z = 8 km in the WSM6-L simulation. The WSM6-L simulation shows smaller snow mixing ratio at almost all levels, overall by 3%, and smaller graupel mixing ratio at z ~ 4–8 km.

Figure 3.11 shows the time- and domain-averaged vertical profiles of microphysical conversion rates related to rainwater obtained from the WSM6-O and WSM6-L simulations and their differences. Note that Fig. 3.11a–c and Fig. 3.11d–f represent the source terms and sink terms of rainwater mass, respectively. The two simulations have the similar vertical profiles of microphysical conversion rates. Among the microphysical processes, the melting of ice hydrometeors contributes most to the rainwater production. In both simulations, the rate of melting of ice hydrometeors is ~10 times the rate of accretion of cloud water, when the rates are vertically integrated. The rates of melting of snow and graupel are both greatest at z = 4.5 km. Except for the melting of ice hydrometeors, the accretion of cloud

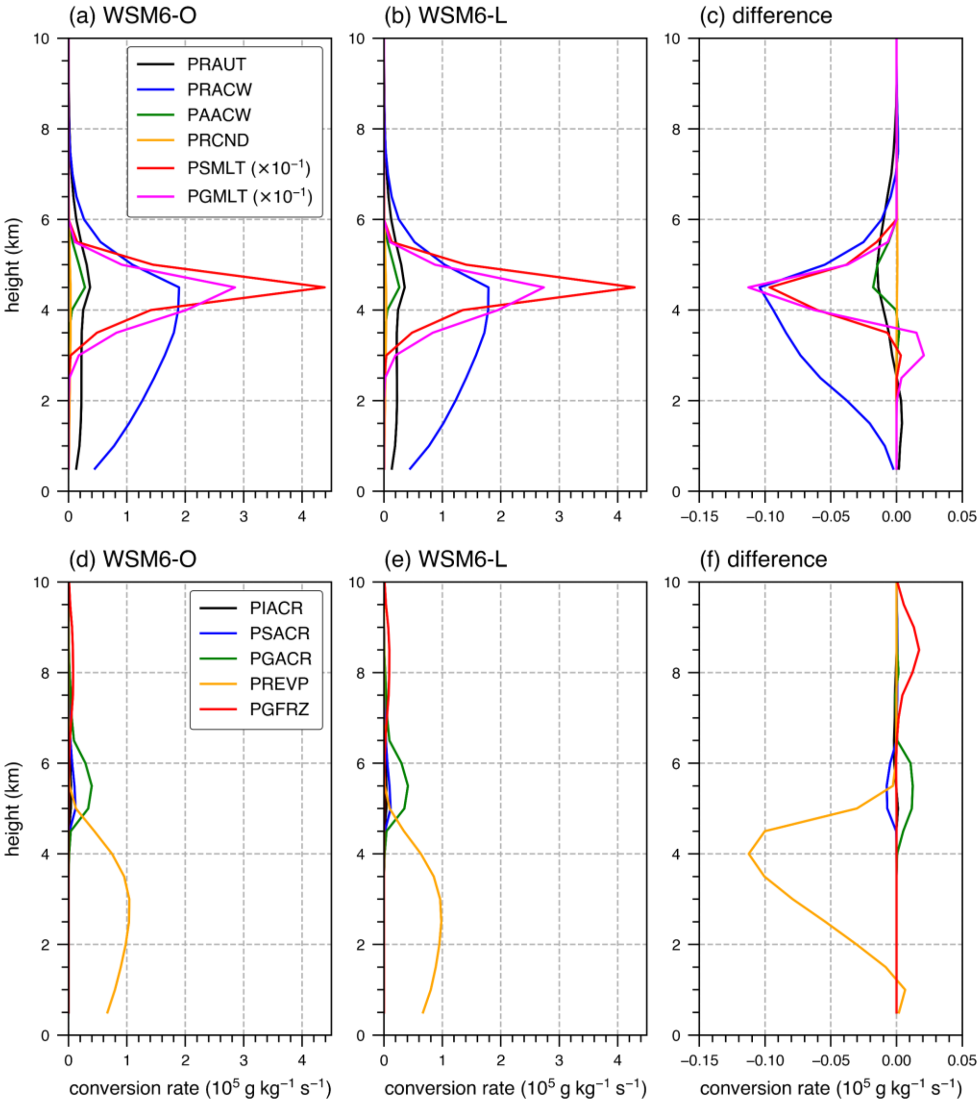
(a) WSM6-O
(b) WSM6-L
(c) difference
PRAUT
PRACW
PAACW
PRCND
PSMLT (×10⁻¹)
PGMLT (×10⁻¹)
height (km)
(d) WSM6-O
(e) WSM6-L
(f) difference
PIACR
PSACR
PGACR
PREVP
PGFRZ
conversion rate (10⁵ g kg⁻¹ s⁻¹)

Figure 3.11 Time- and domain-averaged vertical profiles of microphysical conversion rates related to rainwater (PRAUT: autoconversion of cloud water to rainwater, PRACW: accretion of cloud water by rainwater, PAACW: weighted mean of two types of accretion – accretion of cloud water by snow and accretion of cloud water by graupel, PRCND: condensation on rainwater, PSMLT: snow melting, PGMLT: graupel melting, PIACR: accretion rate of rainwater by cloud ice, PSACR: accretion rate of rainwater by snow, PGACR: accretion rate of rainwater by graupel, PREVP: evaporation of rainwater, PGFRZ: freezing of rainwater) obtained from the (a, d) WSM6-O and (b, e) WSM6-L simulations and (c, f) their differences (WSM6-L minus WSM6-O).

water by rainwater is the largest source of rainwater mass, followed by the autoconversion of cloud water. The conversion rates for source processes related to cloud water (PRAUT, PRACW, and PAACW) are greatest at z = 4.5 km where the peak of cloud water mixing ratio appears (Fig. 3.10a and b). The largest sink of rainwater mass is rainwater evaporation, which is most active at $z \sim 2.5$–3 km. The accretion of rainwater by ice hydrometeors and freezing occur near or above the melting layer, but the conversion rates for those processes are much smaller than the evaporation rate. The WSM6-L simulation shows overall 4% smaller rate of accretion of cloud water and 3% smaller melting rates of snow and graupel than the WSM6-O simulation (Fig. 3.11c). The evaporation rate in the WSM6-L simulation is overall 7% smaller than that in the WSM6-O simulation (Fig. 3.11f). The decreases in the rates of accretion and melting contribute to the decrease in rainwater mixing ratio in the WSM6-L simulation, and the contribution of the latter is larger.

Overall, the implementation of the N_0 diagnostic relation causes decreases in the rates of evaporation, accretion of cloud water, and melting. Because of the diagnostic relation, the WSM6-L simulation predicts N_0 that is on average smaller than the prescribed value in the WSM6-O simulation, which to some extent agrees with the observation that the peak of N_0 PDF appears at the value that is smaller than the prescribed value (Fig. 3.8). The smaller number of small raindrops and larger number of large raindrops in the

RSDs in the WSM6-L simulation caused by the smaller N_0 and Λ decrease the evaporation rate due to the smaller surface area and faster sedimentation of raindrops on average. The reduced evaporative cooling can affect the thermodynamic environment and lead to some changes in convection development. Figure 3.12 shows the differences in the horizontal fields and vertical profiles of virtual potential temperature θ_v between the WSM6-L and WSM6-O simulations. At z = 4 km where the decrease in rainwater evaporation in the WSM6-L simulation is maximized (Fig. 3.11f), θ_v is higher in the WSM6-L simulation over most of the domain due to the reduced evaporative cooling (Fig. 3.12a). At z = 1 km, on the other hand, θ_v is lower in the WSM6-L simulation over most of the domain (Fig. 3.12b). Consequently, the thermodynamic environment in the WSM6-L simulation is more stable than that in the WSM6-O simulation (Fig. 3.12c), which can lead to reduced cloud activities and thus the reduced amount of condensates in the WSM6-L simulation (Fig. 3.10c).

When the rainwater mixing ratio is not changed much, a decrease in N_0 and the corresponding decrease in Λ result in a decrease of accretion rate, based on the formula of the WSM6 scheme where the accretion rate is proportional to $N_0/\Lambda^{3.8}$ (Eq. (A40) in Hong et al. (2006)). The faster sedimentation of raindrops in the WSM6-L simulation can decrease the upward transport of raindrops above the freezing level, which can weaken ice

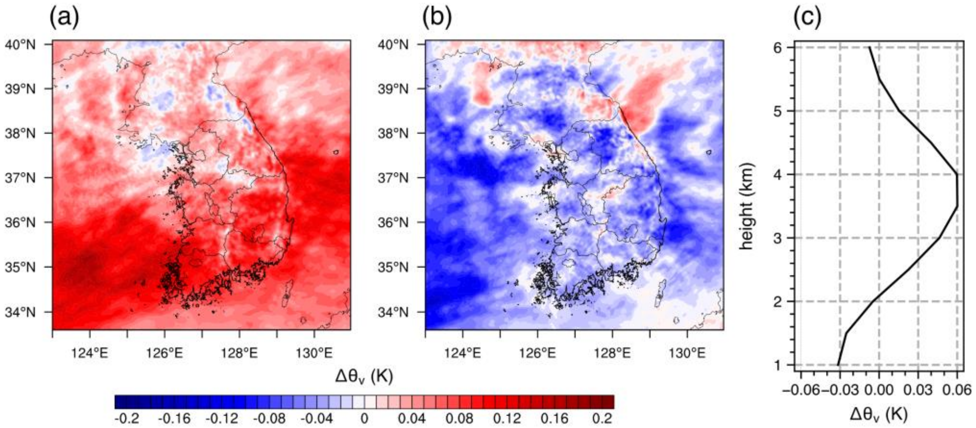

Figure 3.12 Differences in the horizontal fields at (a) z = 4 km and (b) z = 1 km and (c) vertical profiles of virtual potential temperature θ_v between the WSM6-L and WSM6-O simulations (WSM6-L minus WSM6-O).

microphysical processes. This may be a possible reason for the decreases in the ice hydrometeor mixing ratios and thus the decreases in the rates of melting of snow and graupel in the WSM6-L simulation.

The impacts of applying the diagnostic relation for N_0 on precipitation prediction can to some extent vary depending on the precipitation case. In addition to the summertime precipitation case analyzed above, a precipitation case associated with a low pressure system that occurred in April is simulated. The simulation period is from 06 UTC 2 to 18 UTC 3 April 2021, and the last 24 h of the period is the analysis period. Figure 3.13 shows 24-h accumulated precipitation amount from rain gauge observation and predicted in the WSM6-O and WSM6-L simulations. The WSM6-L simulation shows smaller RMSE (11.4 mm) and higher R (0.85) than the WSM6-O simulation (RMSE: 11.6 mm, R: 0.84) as in the summertime precipitation case, but the difference in the performance between the two simulations are reduced. The simulated N_0 and Λ are evaluated in Fig. 3.14, and the WSM6-L simulation still shows its advantages, that is, better predicting N_0 than the WSM6-O simulation and preventing the appearance of unrealistically high Λ. In the vertical profiles of hydrometeor mixing ratios (Fig. 3.15), the WSM6-L simulation shows smaller rainwater mixing ratio and snow mixing ratio than the WSM6-O simulation, which is also seen for the summertime precipitation case. On the other hand, the change in cloud

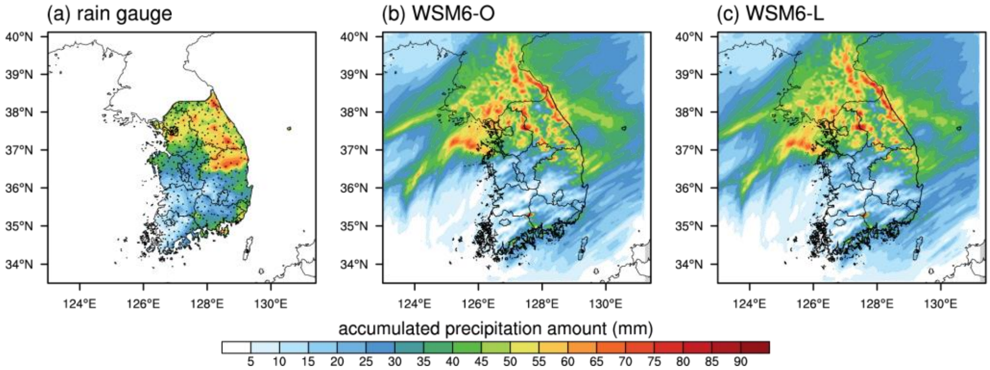

Figure 3.13 24-h accumulated precipitation amount (a) observed at rain gauge stations (marked with black dots in (a)) and predicted in the (b) WSM6-O and (c) WSM6-L simulations.

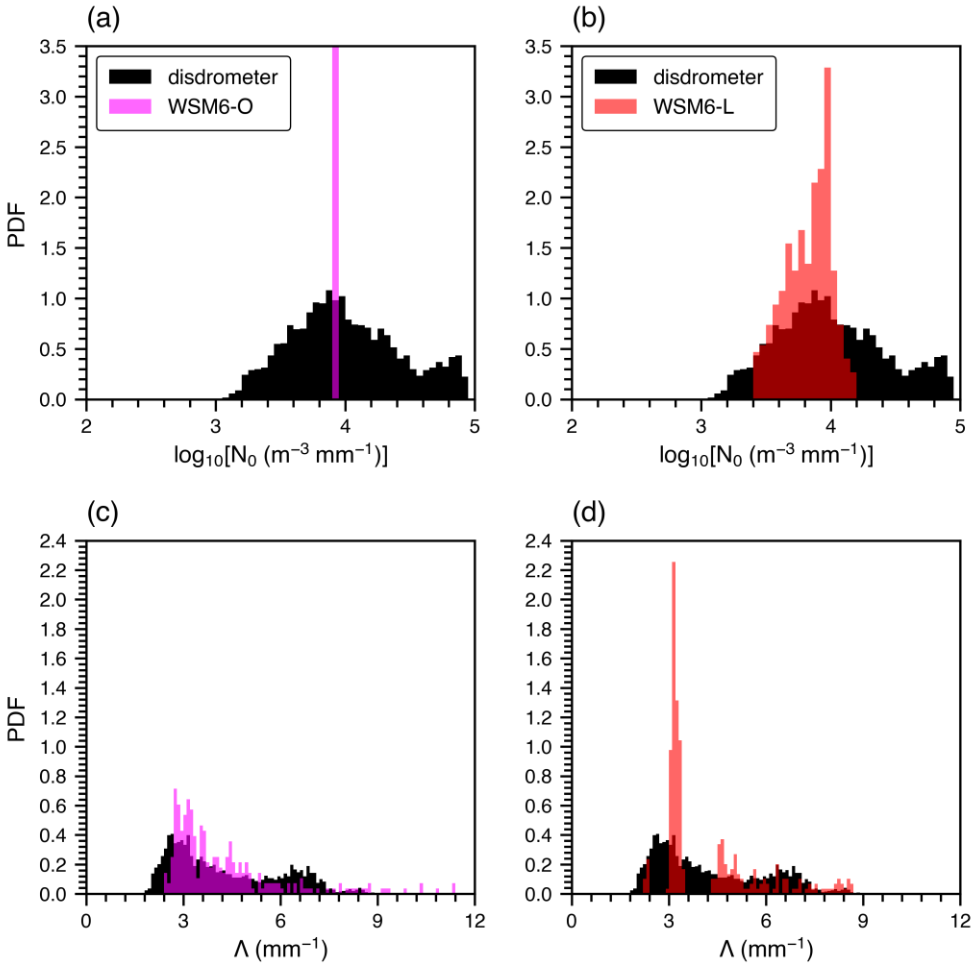

Figure 3.14 As in Fig. 3.8, but for the precipitation case on 2–3 April 2021.

water mixing ratio is not consistent in the two cases, which indicates that the impacts of the diagnostic relation on cloud microphysical characteristics can change with the precipitation case to some extent.

For the two precipitation cases simulated in this study, improvements in precipitation prediction are seen. More rigorous evaluation of the impacts of the diagnostic relation can be conducted if a larger variety of precipitation cases are simulated, which may be done in the future when more computational resources are available.

4 Raindrop size distributions simulated using a bin microphysics scheme: Different biases in stratiform and convective rain from an extratropical cyclone

4.1 Introduction

In cloud-resolving models, the cloud microphysical processes are represented using either bulk or bin microphysics schemes. The main difference between the two types of schemes is how the size distribution of hydrometeors is treated. While the bulk microphysics scheme assumes the size distribution of any hydrometeor to follow a specific distribution (e.g., exponential, gamma, and log-normal distribution), the bin microphysics scheme explicitly predicts the size distribution of any hydrometeor using size (mass) bins. The explicit prediction of hydrometeor size distributions by bin microphysics schemes enables to numerically solve the governing equations for microphysical processes with minimal approximations, which makes their prediction generally superior than that of bulk microphysics schemes (Iguchi, Nakajima, et al. 2012; Lee and Baik 2018, Lynn and Khain 2007).

Hydrometeor size distributions predicted using a bin microphysics scheme can be directly compared with observed distributions, which provides a more informative evaluation of precipitation simulations than comparing bulk precipitation characteristics such as precipitation rate. Hydrometeor size distributions contain information about the dominant microphysical processes involved in the clouds (Rosenfeld and Ulbrich 2003). For example, the collision–coalescence between raindrops decreases the number concentration of small raindrops and increases that of large raindrops, while the breakup of raindrops acts in the opposite manner. Therefore, the evaluation of simulated hydrometeor size distributions provides an indirect evaluation of simulated cloud microphysics, which is valuable because directly evaluating the microphysical process rates in the simulation based on in-situ observations is extremely difficult.

There have been some studies that evaluated the hydrometeor size distributions simulated using bin microphysics schemes (Chen et al. 2023; Fridlind et al. 2017; Hernández Pardo et al. 2021; Iguchi, Matsui, et al. 2012; Khairoutdinov and Kogan 1999; Morrison et al. 2022; Shpund et al. 2019; Witte et al. 2019). Khairoutdinov and Kogan (1999) and Witte et al. (2019) evaluated the simulated cloud drop size distributions in marine stratocumulus in comparison with aircraft observations and both found prominent discrepancies at the cloud boundaries. The discrepancies were attributed to the inaccurate representation of small-scale entrainment and mixing due to insufficient spatial resolution (Khairoutdinov and Kogan, 1999) and to a spurious peak of supersaturation generated by numerical problems (Witte et al. 2019). Shpund et al. (2019) simulated a rainfall event during Midlatitude Continental Convective Cloud Experiment (MC3E) and showed that the snow particle number concentration decreases with decreasing height in a larger rate in the simulation than in the aircraft observations. They suggested that the lack of ice fragmentation by collision between ice particles in the simulation is one of the possible reasons.

The evaluation of raindrop size distribution (RSD) has been performed using ground-based disdrometers (Chen et al. 2023; Iguchi, Matsui, et al. 2012; Shpund et al. 2019). Iguchi, Matsui, et al. (2012) evaluated the simulated RSDs in a rainfall event during MC3E. The simulation well reproduced the RSD differences between deep convective clouds and shallow warm clouds, but large raindrops were simulated when the precipitation rate is small, which did not appear in the disdrometer observations. They speculated that the absence of spontaneous breakup in the bin microphysics scheme may have led to the preservation of large raindrops formed by the melting of ice particles. The aforementioned study of Shpund et al. (2019) also evaluated the simulated RSDs using disdrometer observations. Contrary to the simulated snow particle size distributions that showed some discrepancy with the aircraft observations, the simulated RSDs at the surface showed good agreement with the disdrometer observations. Chen et al. (2023) evaluated the performances of different cloud microphysics schemes (five bulk microphysics schemes and one bin microphysics scheme) in reproducing the observed RSD variability in an extreme rainfall event that occurred in Henan Province, China. In their results, the simulation with the bin microphysics scheme best reproduced the observed RSD variability although the simulated RSD variability was still not large enough.

The evaluation of RSDs simulated using bin microphysics schemes has been mostly based on a few RSD parameters that are thought to successfully represent the whole RSD characteristics (e.g., Chen et al. 2023; Iguchi, Matsui, et al. 2012). This approach is not different from what has been used to evaluate the RSDs simulated using bulk microphysics schemes (e.g., Jin and Baik 2023; Lin et al. 2022; Wang et al. 2020). However, considering the bin microphysics schemes’ capability of representing hydrometeor size distributions of various shapes, comparison of full RSDs between simulations and observations can provide additional valuable information. For example, the simulated RSDs may contain spurious peaks that do not appear in the observation (which will be shown in this study), or the multimodality of observed RSDs that appear under particular circumstances (Radhakrishna and Rao 2009; Sauvageot and Koffi 2000) may not be captured in simulations.

Either of the abovementioned features can provide some insights into model deficiencies, but has not been investigated yet.

In this study, a precipitation event that occurred in South Korea during the passing of an extratropical cyclone is selected as a case for the evaluation of simulated RSDs. Cloud clusters accompanying an extratropical cyclone mostly consist of different types of clouds and precipitation (Field and Wood 2007; Houze 2014), which can have significantly different cloud microphysics. As the RSDs at the surface reflect the microphysics in the clouds above, the RSDs during this event can substantially vary both spatially and temporally. Examining whether the bin microphysics scheme can reproduce the variation of RSD within this event is an interesting point of this study.

This study evaluates the detailed features of RSDs simulated using a bin microphysics scheme by comparing full RSDs with disdrometer observations for different sub-periods within a precipitation event associated with an extratropical cyclone. Then, we attempt to figure out the sources of biases in the bin microphysics scheme. In subchapter 4.2, the precipitation case, disdrometer data, and simulation setup are described. In subchapter 4.3, results and discussion are given. A summary and conclusions are provided in Chapter 6.

4.2 Data and method

4.2.1 Case description

On 8 November 2018, an extratropical cyclone that developed over the East China Sea and moved northeast caused precipitation throughout South Korea. A large amount of precipitation occurred mainly in the northwestern part of South Korea, and the 24-h accumulated precipitation amount observed by a disdrometer in Seoul was 62 mm. Figure 4.1 shows the synoptic conditions for this precipitation event represented using the European Centre for Medium-Range Weather Forecasts reanalysis data (ERA5, Hersbach et al. 2020). At 0900 LST 8, a 500-hPa trough was located over eastern China and an 850-hPa trough was located to the east of the 500-hPa trough, indicating a westward tilt of the trough axis which is a favorable condition for a surface low-pressure system to develop. Along the east of the troughs, there are strong updrafts at the 500-hPa level (Fig. 4.1a). The low-level jet transports the warm and humid air toward South Korea (Fig. 4.1c). At 1500 LST 8, the troughs at the 500-hPa and 850-hPa levels strengthen. The 500-hPa updrafts appear along the western coast of South Korea and becomes stronger than at 0900 LST 8 (Fig. 4.1b). The transport of warm and humid air toward South Korea by the low-level jet is further intensified (Fig. 4.1d).

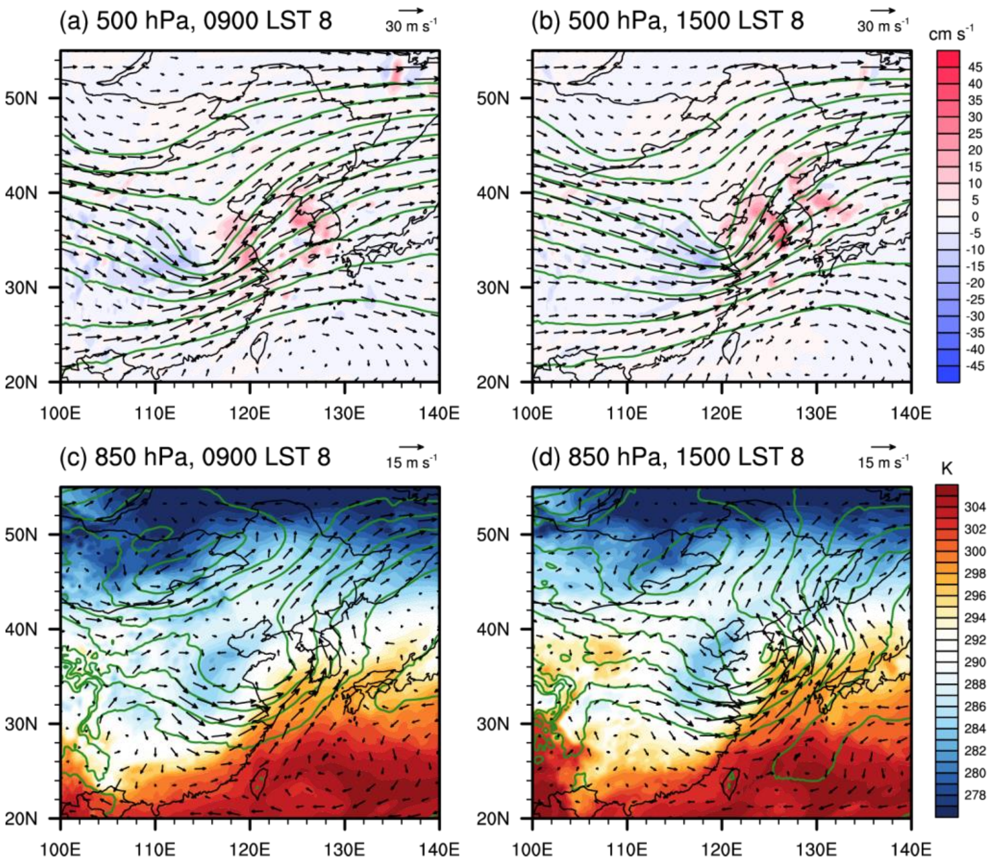

Figure 4.1 Fields of (a, b) 500-hPa and (c, d) 850-hPa geopotential height (green lines) and horizontal wind vectors (arrows) at (a, c) 0900 and (b, d) 1500 local standard time (LST) 8 November 2018. The color shades in (a, b) indicate the 500-hPa vertical velocity, and those in (c, d) indicate the 850-hPa equivalent potential temperature.

4.2.2 Model description and simulation setup

The Weather Research and Forecasting (WRF) model version 4.3.3 is used to simulate the precipitation event that occurred on 8 November 2018. The model domain configuration and the location of disdrometer are shown in Fig. 4.2. Three one-way nested domains centered on South Korea are used. The numbers of horizontal and vertical grids for all three domains are 250 × 250 and 49, respectively. The horizontal grid spacings are 18, 6, and 2 km for domains 1, 2, and 3 respectively. The vertical grid is stretched from ~60 m for the lowest layer to ~450 m for the highest layer. The physical parameterizations considered in this simulation are the unified Noah land surface model (Tewari et al. 2004), the revised MM5 surface layer scheme (Jiménez et al. 2012), the University of Washington boundary layer scheme (Bretherton and Park 2009), the Dudhia shortwave radiation (Dudhia, 1989), the Rapid Radiative Transfer Model (RRTM) longwave radiation scheme (Mlawer et al. 1997), the Kain–Fritsch cumulus parameterization scheme (Kain 2004), and the modified version of bin cloud microphysics scheme in the Hebrew University Cloud Model (HUCM, Khain et al. 2011; Lee and Baik 2016). Note that the cumulus parameterization scheme is used only for domains 1 and 2.

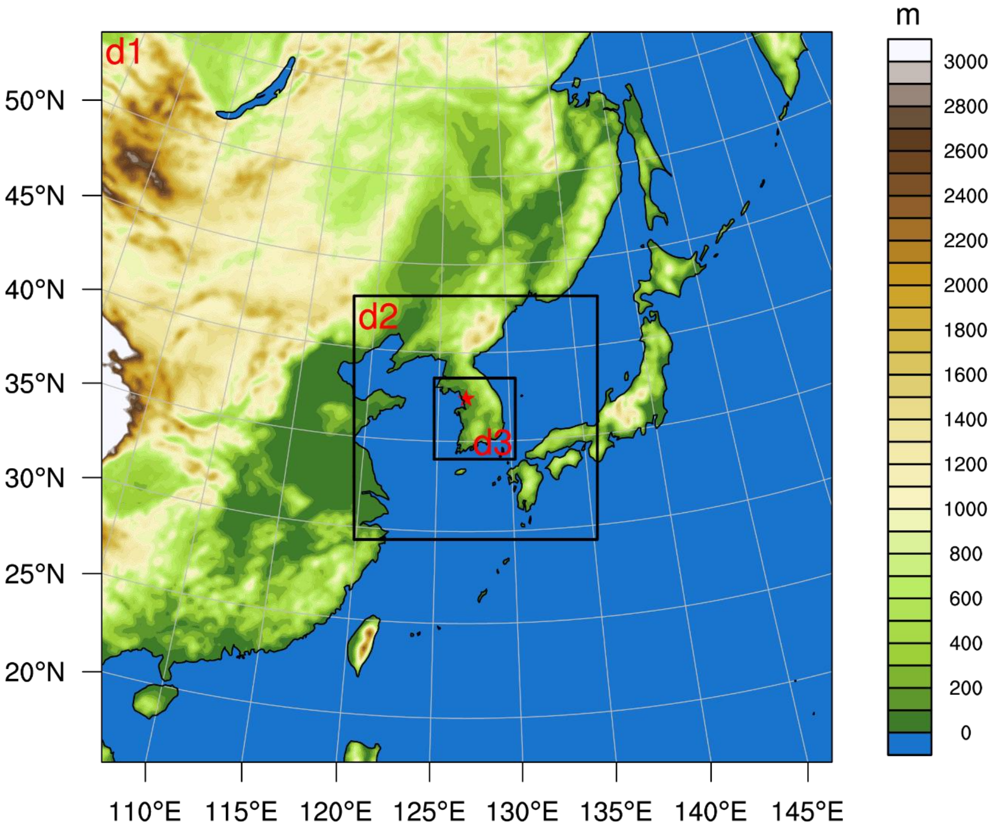

Figure 4.2 Model domain configuration with topography (shaded). The red star in domain 3 indicates the disdrometer site in Seoul.

Unlike bulk microphysics schemes which parameterize the size distribution of any hydrometeor using some parameters, the modified version of bin microphysics scheme in the HUCM explicitly predicts the size distribution. In this scheme, 43 mass-doubling bins are considered for seven hydrometeor types (liquid drop, three types of ice crystal (column, plate, and dendrite), snow, graupel, and hail) and aerosol. The microphysical processes included are nucleation, vapor diffusion, collection, breakup, sedimentation, freezing, melting, and secondary ice multiplication processes. For the collision process, turbulence-induced collision enhancement (Lee and Baik, 2016) is implemented in this version. Liquid water fractions of snow, graupel, and hail and rimed fraction of snow are predicted to calculate the time-dependent graupel melting and density and snow terminal velocity, respectively. The initial aerosol number concentration of 300 cm^{-3} is considered in this study. The model is integrated for 18 h starting from 21 LST 7 November 2018, and the last 12 h are used for analysis. As initial and boundary conditions, the ERA5 reanalysis data (Hersbach et al. 2020), which have a 1-h temporal resolution and a 0.25° horizontal resolution, are used.

4.2.3 RSDs from the disdrometer and the bin

microphysics scheme

For evaluation of RSDs simulated using a bin microphysics scheme, this study uses the data from Parsivel^2 disdrometer (Tokay et al. 2014) installed at Seoul National University in South Korea (37.45°N, 126.95°E; the red star in Figure 2). When precipitating particles pass through the laser sheet (180 mm long; 30 mm wide; 1 mm high) between the two heads of the disdrometer, the disdrometer optically measures the diameter and fall velocity of precipitating particles using the maximum attenuation of laser signal and the duration of precipitating particles within the laser sheet, respectively. The measured information about the diameter and fall velocity is assigned to the matrix of 32 size (0–26 mm) and 32 fall velocity (0–22.4 m s^{-1}) bins with a sampling interval of 1 minute.

The number and resolution of size bins in the disdrometer data and the bin microphysics scheme are different. The disdrometer considers 32 non-uniform size bins and the bin microphysics scheme considers 43 mass-doubling size bins. For raindrops, the disdrometer uses the 3rd–23rd size bins (diameter range of 0.25–8 mm). First two size bins are not considered due to the low signal-to-noise ratio. To match as closely as possible with the diameter range of the disdrometer data, the 19th–33rd size bins (diameter range of 0.23–7.3 mm) of the bin microphysics scheme are used for RSD evaluation.

To remove erroneous data caused by measurement errors such as a partial detection of drops at the edges of the laser sheet, splashing drops, drops affected by strong winds, and multiple small drops being perceived as one large drop, drops with fall velocities 60% larger or 60% smaller than theoretical values are excluded using the fall velocity–diameter relationship of Atlas et al. (1973). In addition, 1-min disdrometer data with the total drop count smaller than 100 or with the rain rate smaller than 0.05 mm h^{-1} are excluded, and the remaining data are further refined by removing data where the duration of rainfall is less than 3 minutes (Thompson et al., 2015). To ensure a fair comparison between the simulated and observed RSDs, the abovementioned method of Thompson et al. (2015) is also applied to the simulated RSDs.

The RSDs from the disdrometer are obtained as follows:

$$N(D_i) = \sum_{j=3}^{23} \frac{n_{ij}}{A_i V_j \Delta t \Delta D_i}, \quad (4.1)$$

where D_i (mm) is the mid-value of the ith diameter bin, $N(D_i)$ (m^{-3} mm^{-1}) is the raindrop number per unit volume per unit size interval for the ith diameter bin, n_{ij} is the number of raindrops assigned to the ith diameter and jth fall velocity bin, A_i (m^2) is the effective sampling area of the ith diameter bin, V_j (m s^{-1}) is the fall velocity of the jth fall velocity bin, Δt (s) is the sampling interval, and ΔD_i (mm) is the width of the ith diameter bin. The rain rate R (mm h^{-1}) is calculated as

$$R = 6\pi \times 10^{-4} \sum_{i=3}^{23} \sum_{j=1}^{32} D_i^3 \frac{n_{ij}}{A_i \Delta t}. \tag{4.2}$$

RSD parameters are calculated from both simulated and observed RSDs. The nth-order RSD moment M_n (m^{-3} mm^n) is calculated by

$$M_n = \sum_{i=i_s}^{i_e} D_i^n N(D_i) \Delta D_i, \tag{4.3}$$

where (i_s , i_e) is (3, 23) for the disdrometer data and (19, 33) for the bin microphysics scheme. The mass-weighted mean diameter D_m (mm) and the generalized intercept parameter N_w (m^{-3} mm^{-1}) are calculated as follows:

$$D_m = \frac{M_4}{M_3}, \tag{4.4}$$

$$N_{\mathrm{w}} = \frac{4^4}{\Gamma(4)}\left(\frac{M_3}{D_{\mathrm{m}}^4}\right), \tag{4.5}$$

where Γ is the gamma function.

4.3 Results and discussion

4.3.1 Evaluation of simulated raindrop size distribution

Figure 4.3 shows the spatial distributions of observed and simulated average rain rate for the periods of 0830–1030 LST, 1030–1230 LST, and 1230–1400 LST. The observation data are collected from 586 rain gauges. For 0830–1030 LST, in both the observation and simulation, light rain is widespread over the northern part of South Korea and a rainband with moderate intensity approaches Seoul from its southwest (Figs. 4.3a and 4.3b). For 1030–1230 LST, the approaching rainband in the observation is elongated in the west–east direction and is on the verge of entering Seoul, while the rainband in the simulation is elongated in the southwest–northeast direction and has already entered Seoul (Figs. 4.3c and 4.3d). For 1230–1400 LST, Seoul is under the influence of the rainband with moderate or heavy intensity in both the observation and simulation (Figs. 4.3e and 4.3f). Despite some

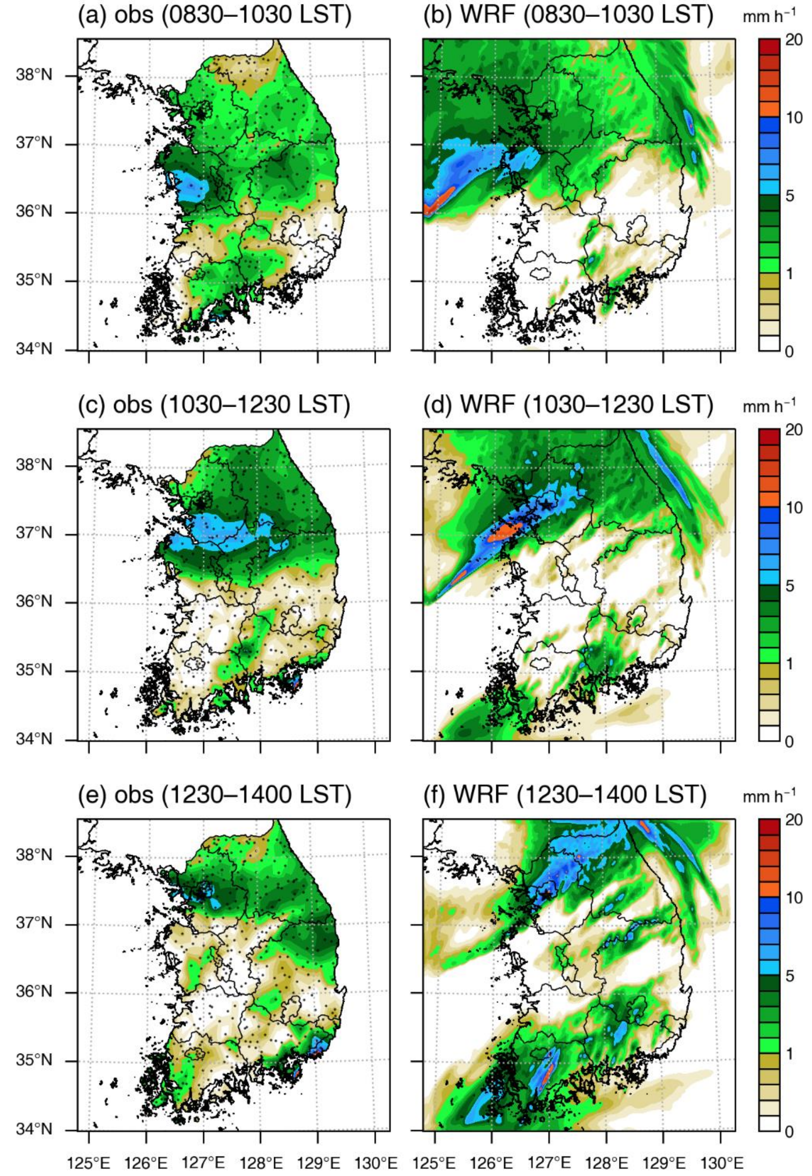

Figure 4.3 Spatial distributions of (a, c, e) observed and (b, d, f) simulated average rain rates for the periods of (a, b) 0830–1230 LST, (c, d) 1030–1230 LST, and (e, f) 1230–1400 LST.

differences in the orientation and moving speed of rainband, Seoul experiences the same rainband in both observation and simulation during this event.

Figure 4.4 shows the time series of rain rate averaged over the 110 rain gauges in the Seoul Metropolitan Area and the time series of the rain rate and rain type at the disdrometer site in the observation and the simulation. A 10-minute moving average is applied to the times series. The rain type classification is done following the method of Wen et al. (2016). Rain is classified as stratiform if the rain rate is larger than 0.5 mm h^{-1} and the 10-min standard deviation of rain rate is smaller than 1.5 mm h^{-1}, and it is classified as convective if the rain rate is larger than 5 mm h^{-1} and the 10-min standard deviation is larger than 1.5 mm h^{-1}. Otherwise, it remains unclassified. In the Seoul Metropolitan Area (Fig. 4.4a), the observed rain rate is small until ~0800 LST and increases to reach its first peak at 1044 LST, after which it decreases and increases again showing its highest peak at 1302 LST. The simulation overall well reproduces this trend of rain rate, with a slight delay of the first peak (1058 LST) and a slight advance of the highest peak (1228 LST). In the comparison between simulation and disdrometer observation (Fig. 4.4b), moderate rain with weak temporal variability classified as stratiform rain during 0830–1030 LST and heavy rain with strong temporal variability classified as convective rain during 1230–1400 LST are

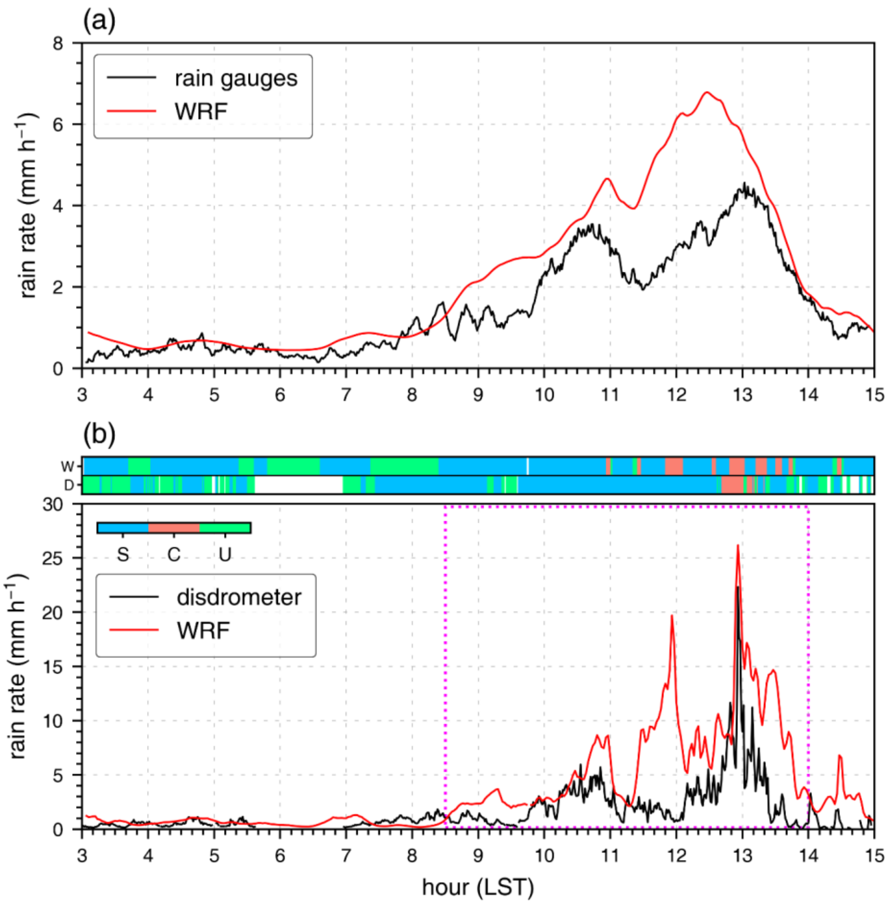

Figure 4.4 (a) Time series of rain rate in the rain gauge observation and simulation averaged over the locations of 110 rain gauges in the Seoul Metropolitan Area. (b) Time series of rain rate in the disdrometer observation and simulation at the disdrometer site. The rain type of each data in the WRF simulation (W) and disdrometer observation (D) is presented at the top of (b), which is categorized as stratiform (S), convective (C), and unclassified (U) following the method of Wen et al. (2016).

well reproduced. It is noteworthy that the time of maximum rain rate in the simulation coincides with that in the observation (1256 LST), and rain at that time is classified as convective in both observation and simulation. The peak during 1120–1210 LST in the simulation is not seen in the observation, which is attributable to the slight mislocation of the simulated rainband. In the following analysis, the period of 0830–1400 LST is selected as a time window to evaluate the RSD prediction.

The simulated RSD averaged over the time window is compared to the disdrometer observation (Fig. 4.5). For the comparison, the drop size bins from 0.256 to 6.502 mm in the simulation are used. The observed raindrop number concentration increases with diameter until its peak at 0.56 mm and then decreases monotonically. The simulation reproduces the overall decrease in $N(D)$ with diameter and particularly shows good agreement with the observation for the intermediate-diameter range. Meanwhile, there are some biases in the small- and large-diameter ranges. For small raindrops, $N(D)$ is overestimated by 1.4–2.4 times (D = 0.56–1.88 mm). Note that for further smaller drops (D < 0.56 mm), the observed $N(D)$ sharply decreases with decreasing diameter but this may be involved with systematic measurement errors (Park et al., 2017; Raupach et al., 2019; Thurai et al., 2017). For large raindrops, the simulation shows a local maximum of $N(D)$ at D = 3.3 mm while the observation does not. This results in an approximately one-order

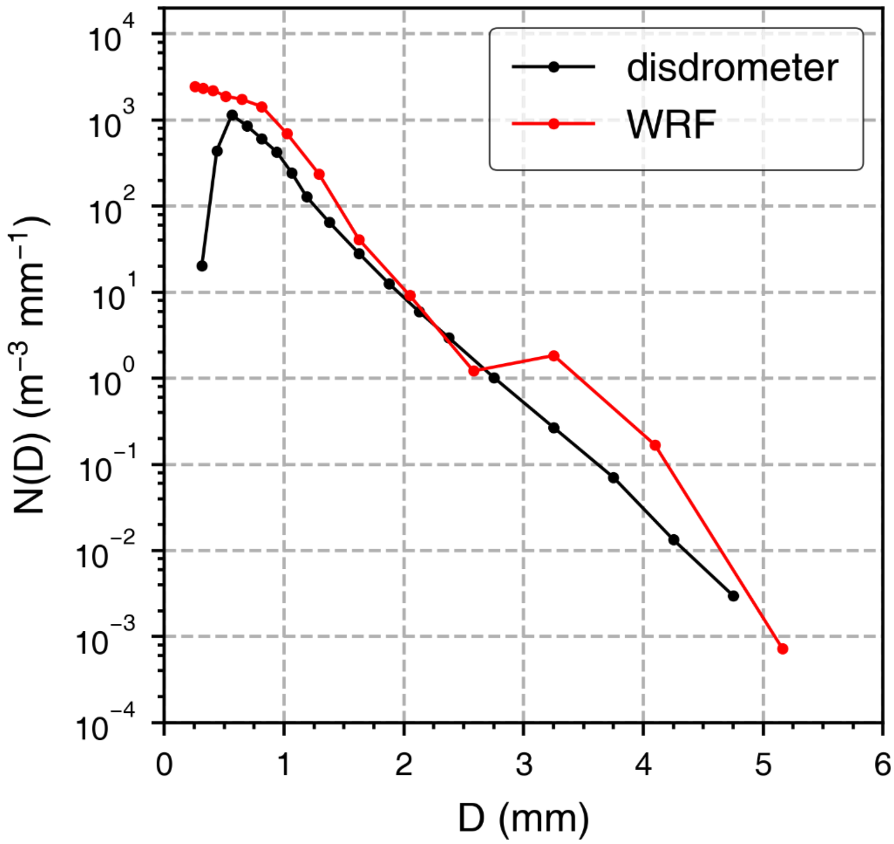

Figure 4.5 Simulated and observed raindrop size distributions at the disdrometer site averaged over the period of 0830–1400 LST.

overestimation of $N(D)$ for D = 3.3–4.3 mm.

For a more detailed evaluation, the time evolution of simulated RSD is compared to the observation (Fig.4. 6). In the observation, during 0830–1230 LST when the stratiform rain is dominant, the RSDs are characterized by a relatively low number concentration of small raindrops and the presence of large raindrops (D > 3.5 mm), resulting in a relatively large variability of RSD width, compared to that during 1230–1400 LST. During 1230–1400 LST when the convective rain is largely involved, the RSDs are characterized by a high number concentration of small raindrops and the lack of large raindrops. This RSD evolution pattern is overall well captured in the simulation. However, a local maximum of $N(D)$ at D = 3.3 mm that is not seen in the observation persists in the stratiform rain until ~1200 LST, and the number concentration of small raindrops after 1230 LST is much larger than the observation.

These comparisons are clearly presented in Fig. 4.7 that shows the observed and simulated average RSDs during two different time periods, Phase 1 (P1; 0830–1030 LST) and Phase 2 (P2; 1230–1400 LST). Here, the period during 1030–1230 LST is excluded because of large discrepancies in rain rate and rain type between the observation and simulation (Figures 3c, 3d, and 4b). In the observation, P1 shows lower number concentration of small raindrops and a wider RSD than P2. The simulation captures these

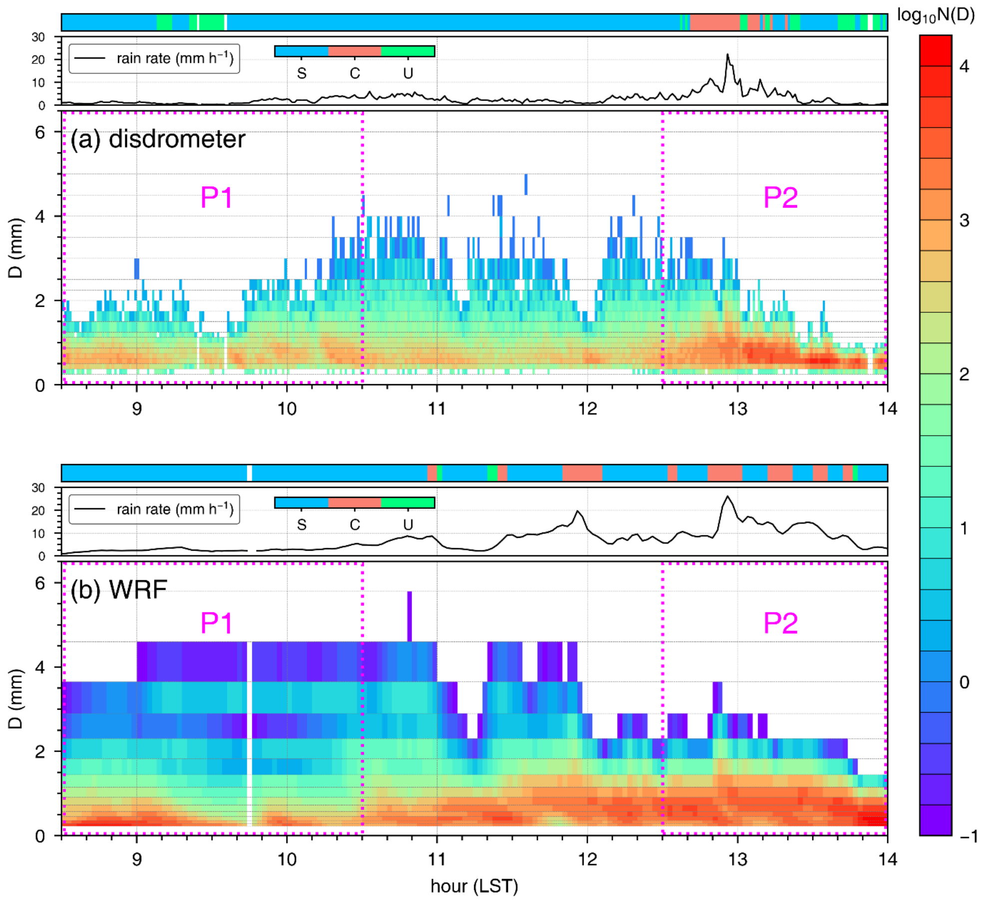

Figure 4.6 Time series of the logarithm of raindrop number concentration (shaded) in the (a) disdrometer observation and (b) simulation at the disdrometer site. The rain type of each data in the observation and simulation is presented at the top of each subfigure, which is categorized as stratiform (S), convective (C), and unclassified (U) following the method of Wen et al. (2016), along with the time series of rain rate.

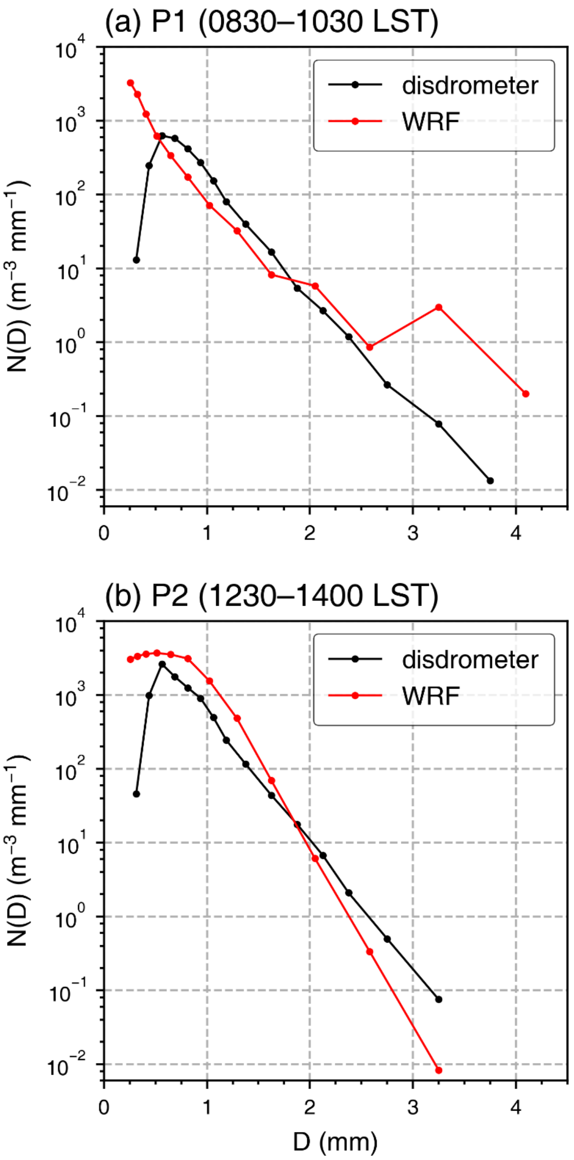

Figure 4.7 Simulated and observed raindrop size distributions at the disdrometer site in (a) Phase 1 (P1) and (b) Phase 2 (P2).

differences in RSD characteristics between P1 and P2, but the differences are somewhat exaggerated. In P1, the simulation overestimates the number concentration of large raindrops, showing a local maximum at D = 3.3 mm, and underestimates the number concentration of small raindrops (D = 0.7–1.6 mm) except for very small ones. In P2, the simulation overestimates the number concentration of small raindrops and underestimates the number concentration of intermediate and large raindrops. The overestimation of the number concentration of large raindrops in P1 and the overestimation of the number concentration of small raindrops in P2 are largely responsible for the two prominent biases in the mean RSD for the period of 0830–1400 LST shown in Fig. 4.5.

The simulated and observed RSD characteristics in P1 and P2 are further compared using two widely used RSD parameters, the mass-weighted mean diameter D_m and the logarithm of generalized intercept parameter $\log_{10}N_w$. Figure 4.8 shows the scatterplots of simulated and observed D_m and $\log_{10}N_w$ with their means and standard deviations for the whole time window, P1, and P2. For the whole time window, the simulation shows a higher mean value of D_m compared to the observation, while the mean value of $\log_{10}N_w$ is similar to the observation. Both the standard deviations of D_m and $\log_{10}N_w$ are larger in the simulation than in the observation. In the observation, P1 exhibits a larger mean D_m and a smaller mean $\log_{10}N_w$ than P2. The simulation also

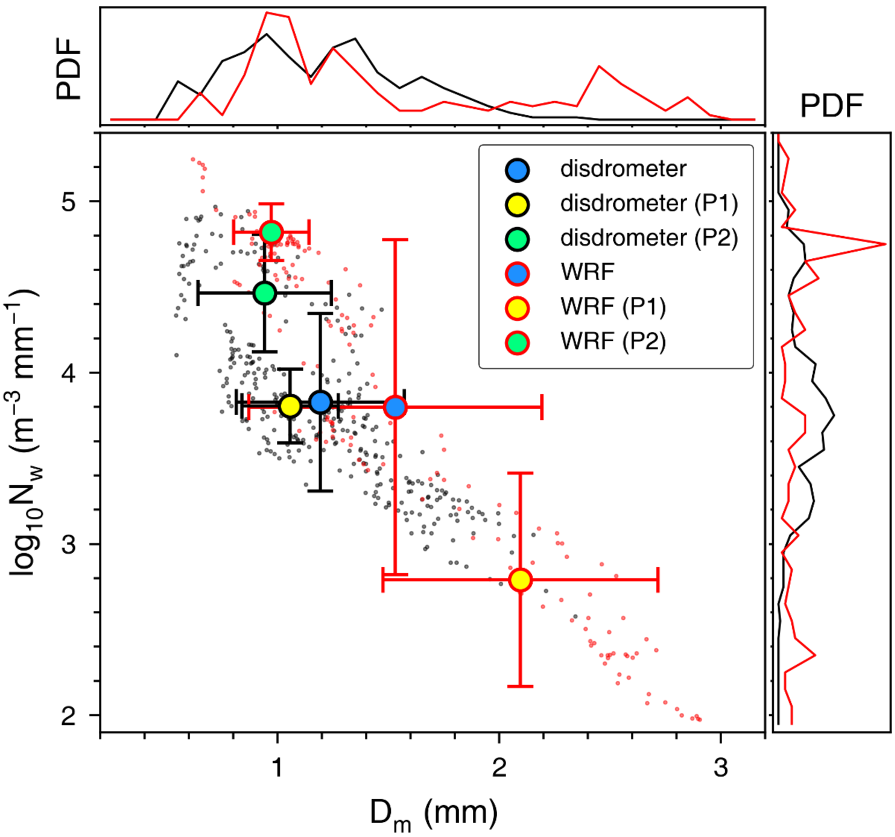

Figure 4.8 Mean values (filled circles) and ±1 standard deviation (whiskers) of mass-weighted mean diameter D_m and the logarithm of generalized intercept parameter $\log_{10}N_w$ at the disdrometer site in the simulation and disdrometer observation. The blue, yellow, and green colors represent the whole time window (0830–1400 LST), P1 (0830–1030 LST), and P2 (1230–1400 LST). The PDFs of D_m and $\log_{10}N_w$ are presented at the top and right side, respectively, where the red and black lines indicate the simulation and disdrometer observation, respectively.

shows that P1 has a larger mean D_m and a smaller $\log_{10}N_w$ than P2, but the differences between P1 and P2 are much larger than in the observation. The large differences between P1 and P2 in the simulation are mainly attributed to the biases present in each phase. In P1, the simulation largely overestimates D_m by 1.0 mm and largely underestimates $\log_{10}N_w$ by 1.0, which is associated with the overestimation of the number concentration of large raindrops. In P2, D_m is similarly simulated, but $\log_{10}N_w$ is overestimated. This is associated with the overestimation of the number concentration of small raindrops. Consequently, the overestimated differences in D_m and $\log_{10}N_w$ between P1 and P2 results in the overly strong variations of RSD in the simulation of this rain event. This is also indicated in the much wider PDFs of D_m and $\log_{10}N_w$. An interesting result is that in P2 when convective rain is largely involved, the standard deviations of D_m and $\log_{10}N_w$ in the simulation is rather smaller than those in the observation, as opposed to P1. This result agrees with that of Chen et al. (2023), who simulated a highly convective rainfall event and saw a lack of RSD variability in the simulation using a bin microphysics scheme compared to the observation. As they suggested, detailed examination on the parameterizations of warm-rain collection and breakup in bin microphysics schemes is needed in the future.

4.3.2 Possible sources of the biases in RSD

prediction

To examine the possible sources of the biases in RSD prediction shown in the previous subchapter, it is necessary to understand the characteristics of the precipitation system and the cloud microphysics therein. Figure 4.9 shows the time-height plot of mixing ratios of liquid-phase and ice-phase hydrometeors and their ratio to the total mixing ratio. P1 and P2 are clearly distinguished by different cloud properties and microphysics. In P1, ice-phase hydrometeors are dominant, accounting for 87% of the total condensates on average. Consistent with the rain type classification which classifies the precipitation during P1 as stratiform rain, weak precipitation appears uniformly at altitudes below 2.5 km. In P2, clouds do not develop up to high altitudes and liquid-phase hydrometeor is predominant, accounting for 89% of the total condensates on average. Contrary to P1, the liquid water mixing ratio abruptly changes with time, resulting in a high temporal variability of rain rate and a much larger average rain rate in P2.

Figure 4.10 shows the simulated RSDs at different levels in P1 and P2, along with the vertical distributions of RSD parameters. In P1, RSD undergoes an abrupt change from z = 3 km to z = 2 km, accompanied by a sharp increase in D_m from 0.4 to 1.6 mm. The RSD at z = 2 km exhibits a local maximum at D = 3.3 mm. The shape of RSD does not significantly

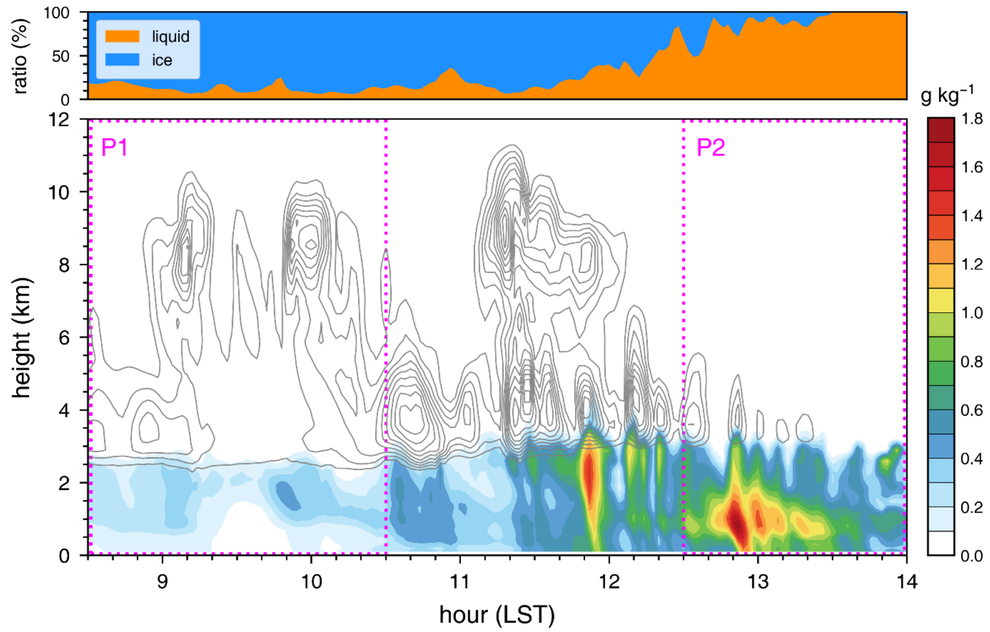

Figure 4.9 Time-height plot of mixing ratios of liquid-phase (shaded) and ice-phase (contoured) hydrometeors at the disdrometer site. The contours are in 0.3 g kg^{-1} intervals. At the top, the ratios of liquid and ice water paths to the total water path are presented.

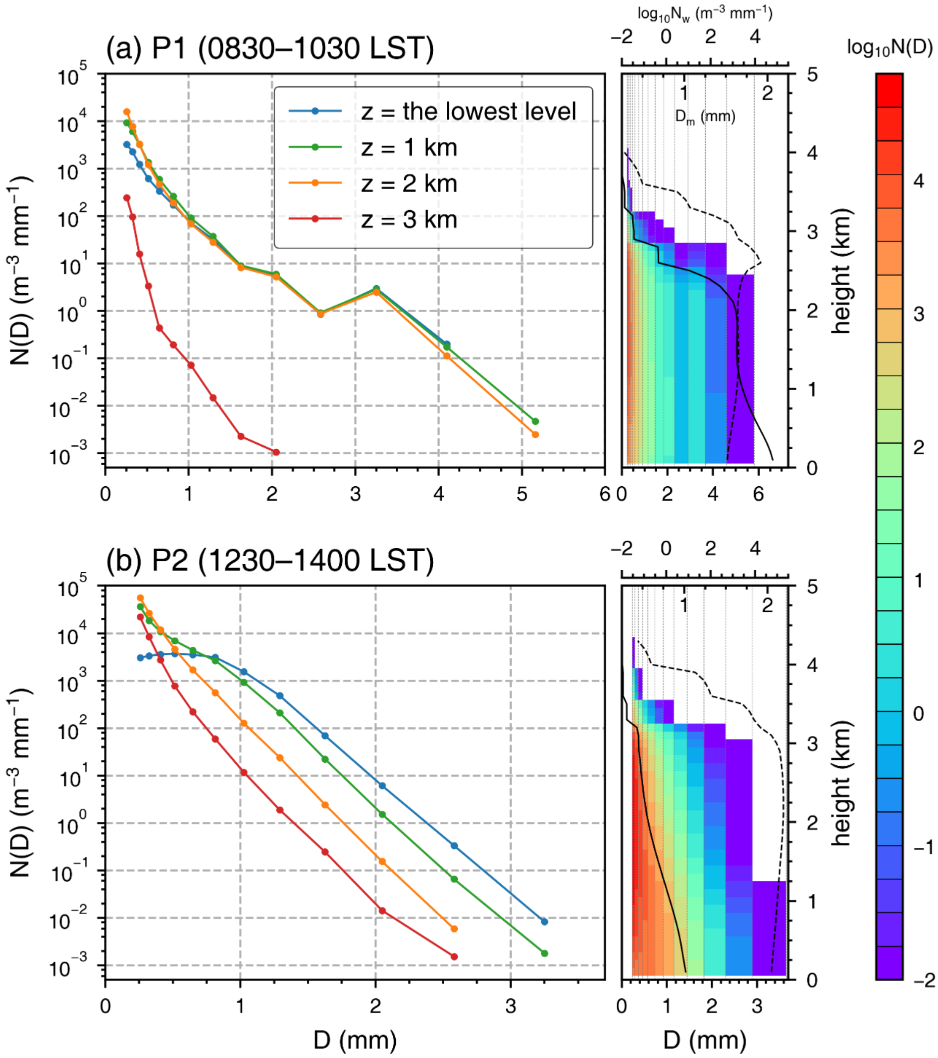

Figure 4.10 Simulated raindrop size distributions at different levels at the disdrometer site in (a) P1 and (b) P2. Vertical distributions of the logarithm of raindrop number concentration $\log_{10}N(D)$ (shaded), mass-weighted mean diameter D_m (solid line), and the logarithm of generalized intercept parameter $\log_{10}N_w$ (dashed line) are presented on the right side of each subfigure.

change from this level to the surface, and particularly, the local maximum remains almost unchanged. Given that the existence of the local maximum at D = 3.3 mm in the simulation is a main discrepancy from the disdrometer observation in P1 (Fig. 4.7a), the above result raises suspicions of an excessive production of large raindrops at z = 2–3 km or insufficient depletion of those large raindrops during their falling, which will be examined further later in this subchapter. Meanwhile, there do exist some minor changes in RSD from z = 2 km to the surface, which are the decrease in the number of very small raindrops and the slight increase in the number of intermediate and large raindrops. In contrast with P1, P2 shows gradual changes in RSD with decreasing height. The number concentration of very small raindrops decreases from z = 2 km with decreasing height, and the number concentration of intermediate and large raindrops significantly increases with decreasing height. Particularly, $N(D)$ for D = 0.8–2.6 mm increases by approximately two orders from z = 3 km to the lowest level. As a result, D_m gradually increases from z = 3 km to the lowest level and $\log_{10}N_w$ decreases a little below z = 2 km. However, the vertical changes in RSD seem to be not large enough, because the disdrometer observation exhibits even lower number concentration of small raindrops and even higher number concentration of large raindrops (Fig. 4.7b).

Cloud microphysical processes in P1 and P2 are investigated separately to figure out the processes that act as the sources of the RSD biases in each phase. For P1, the vertical profiles of hydrometeor mixing ratios and microphysical conversion rates are presented in Fig. 4.11. Clouds in P1 are characterized by a large amount of ice-phase hydrometeors, almost exclusively snow and cloud ice. Cloud ice prevails above $z \sim 8$ km, and snow is dominant from $z \sim 8$ km to $z \sim 2.5$ km with its peak located at $z = 3.2$ km. Cloud water and rainwater are rare above $z = 3.5$ km. The most prominent source of rainwater in P1 is melting, particularly melting of snow, actively occurring at $z \sim 2$–3 km. This suggests that the dramatic changes in RSD from $z = 3$ km to $z = 2$ km, that is, the appearance of the local maximum at $D = 3.3$ mm and the sharp increase in D_m (Fig. 4.10a) are caused by melting of snow. Accretion of cloud water by rainwater is another source of rainwater in P1 that occurs within a wider vertical range ($z \sim 0.5$–3 km), but its contribution to the rainwater production is much smaller than that of melting. To RSDs in P1, the contribution of warm-rain collision–coalescence including the accretion process seems to be limited, which can be deduced from that the RSD does not significantly change from $z = 2$ km to the surface. Nevertheless, the decrease in the number of small raindrops and the slight increase in the number of intermediate and large raindrops with decreasing height can be attributed to the warm-rain collision–coalescence processes. Evaporation that is prominent below $z = 2.5$ km also contributes to reduce the number of small

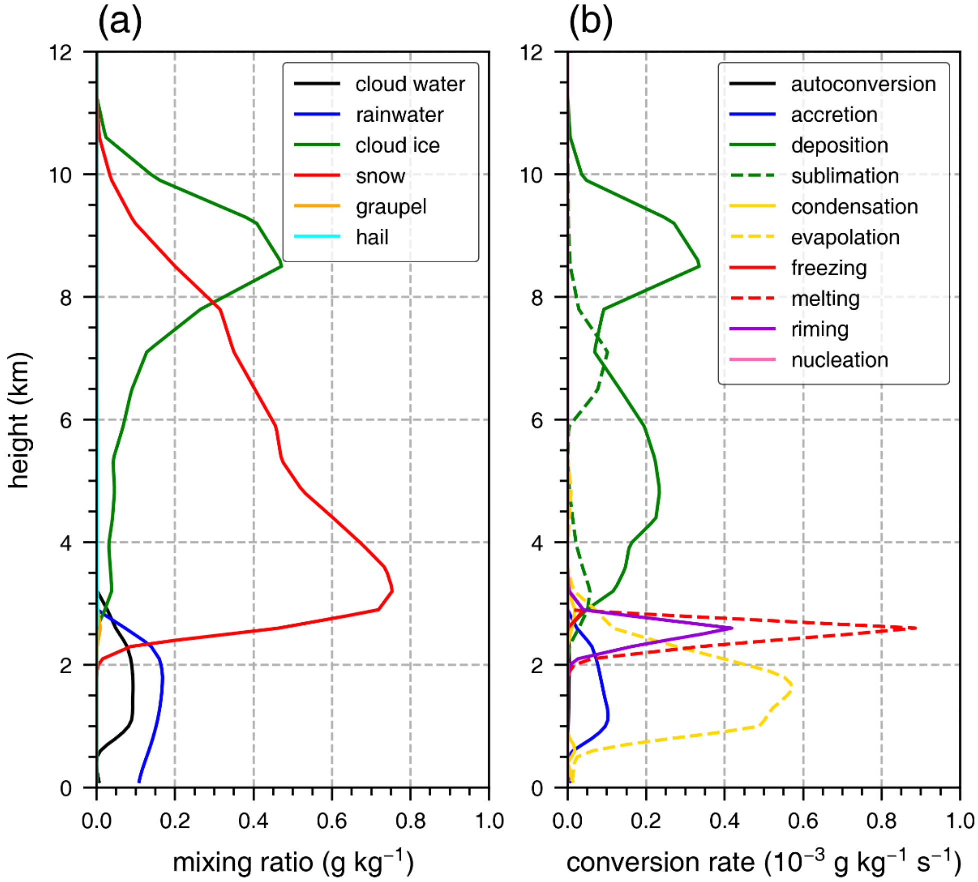

Figure 4.11 Vertical profiles of simulated (a) hydrometeor mixing ratios and (b) microphysical conversion rates at the disdrometer site in P1.

raindrops.

The above results suggest that the prominent bias in RSD prediction in P1, the existence of the local maximum at D = 3.3 mm, can be largely associated with snow melting. To further examine this association, the vertical evolution of simulated snow size distributions is presented in Fig. 4.12. For a direct comparison with the RSD, the snow size distributions are presented as a function of equivalent melted diameter. The shape of snow size distribution at z = 3 km is very similar to the RSD at z = 2 km (Fig. 4.10a). This confirms that the local maximum at D = 3.3 mm in RSD is produced by melting of snow, whose size distribution also exhibits the local maximum at the same equivalent melted diameter. The number concentration of snow particles at D_{eq} = 3.3 mm is gradually accumulated with decreasing height from z = 9 km to z = 3 km, and the local maximum is first formed at z = 6 km. At the altitudes where the local maximum is formed, no mixed-phase microphysical processes but only ice-phase microphysical processes take place (Fig. 4.11b). At these altitudes, snow particles are produced and grow at the expense of cloud ice particles through aggregation (Fig. 4.11a). Therefore, the local maximum in the snow size distributions is the result of active aggregation. This could be a source of RSD biases in P1 because the parameterization of ice–ice collection contains higher uncertainty than those of ice–drop collection or drop–drop collection, due to the highly variable collection

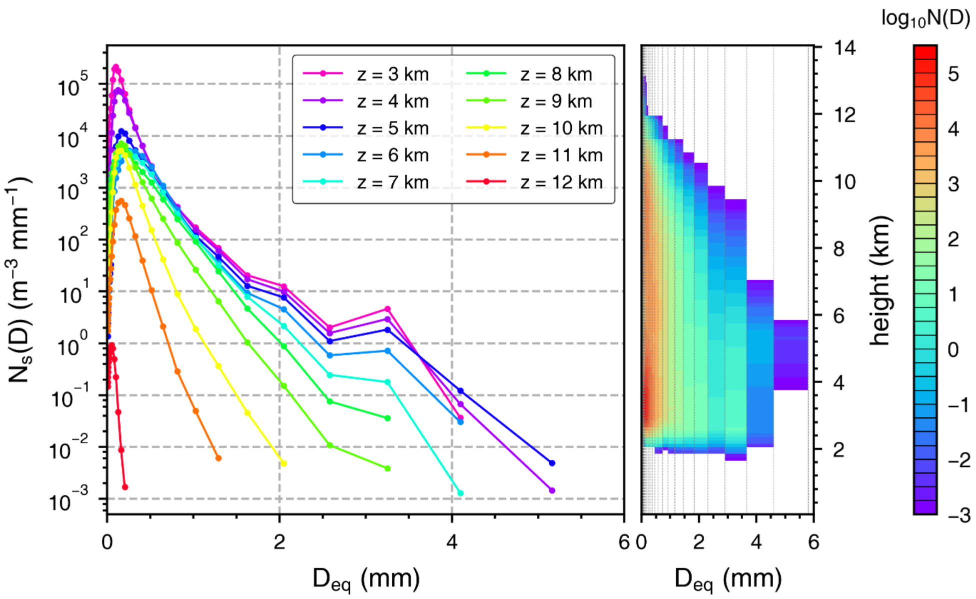

Figure 4.12 Simulated snow size distributions at different levels at the disdrometer site in P1. Vertical distribution of the logarithm of snow number concentration $\log_{10}N_s(D)$ (shaded) is presented on the right side.

efficiency according to the ice particle shapes, temperature, and humidity (Khain et al., 2000) and the lack of observations to properly constrain it. The bin microphysics scheme used in this study employs temperature-dependent collection efficiency for ice–ice collection (Khain et al., 2011), but there still remains high uncertainty in the representation of collection efficiency. The analysis so far gives a conclusion that the overestimation of the number concentration of large raindrops at the surface in P1 may be originated from the overly active aggregation at upper levels.

Besides the over-production of large raindrops, insufficient depletion of large raindrops during their falling could be another reason for the overestimation of large raindrops in P1. Large raindrops produced by melting of large snow particles can breakup into small drops either spontaneously or by collision with other drops. However, the number concentration of large raindrops in P1 rather keeps increasing with decreasing height below the melting layer (Fig. 4.10a), which indicates that the number of large raindrops produced by collision–coalescence is larger than the number of those depleted by spontaneous or collisional breakup. Given that the disdrometer observation exhibits a lower number concentration of large raindrops and a higher number concentration of small raindrops (D = 0.7–1.6 mm) than the simulation in P1 (Fig. 4.7a), the simulated RSD in P1 would be closer to the observed RSD if raindrop breakup were represented to be more active. Particularly, spontaneous breakup can be relatively more important than collisional breakup for large raindrops produced by melting (Paukert et al., 2019), but it is not considered in the bin microphysics scheme used in this study. Considering spontaneous breakup of raindrops in the bin microphysics scheme may contribute to reducing the RSD biases in P1.

Figure 4.13 shows the vertical profiles of hydrometeor mixing ratios and microphysical conversion rates in P2. In P2, liquid-phase hydrometeors (cloud water and rainwater) are dominant, and rainwater shows a bottom-heavy vertical profile with its peak at z = 0.6 km, indicating that rainwater is produced mainly by warm-rain processes. The mixing ratios of ice-phase hydrometeors are relatively small, and their melting does not significantly contribute to the rainwater production. As convective clouds are largely involved in this phase, vigorous condensation occurs and produces a large amount of liquid water mass. Raindrops are generated by autoconversion of cloud droplets that occurs throughout z = 0.5–3 km and grow mainly by accretion of cloud droplets which is more active at lower levels. The active warm-rain collision–coalescence processes including accretion explains the significant and continuous increases in the number concentration of intermediate and large raindrops and decrease in the number concentration of small raindrops with decreasing height in P2 (Fig. 4.10b). Despite these vertical evolution of RSD via accretion, the simulated number concentration

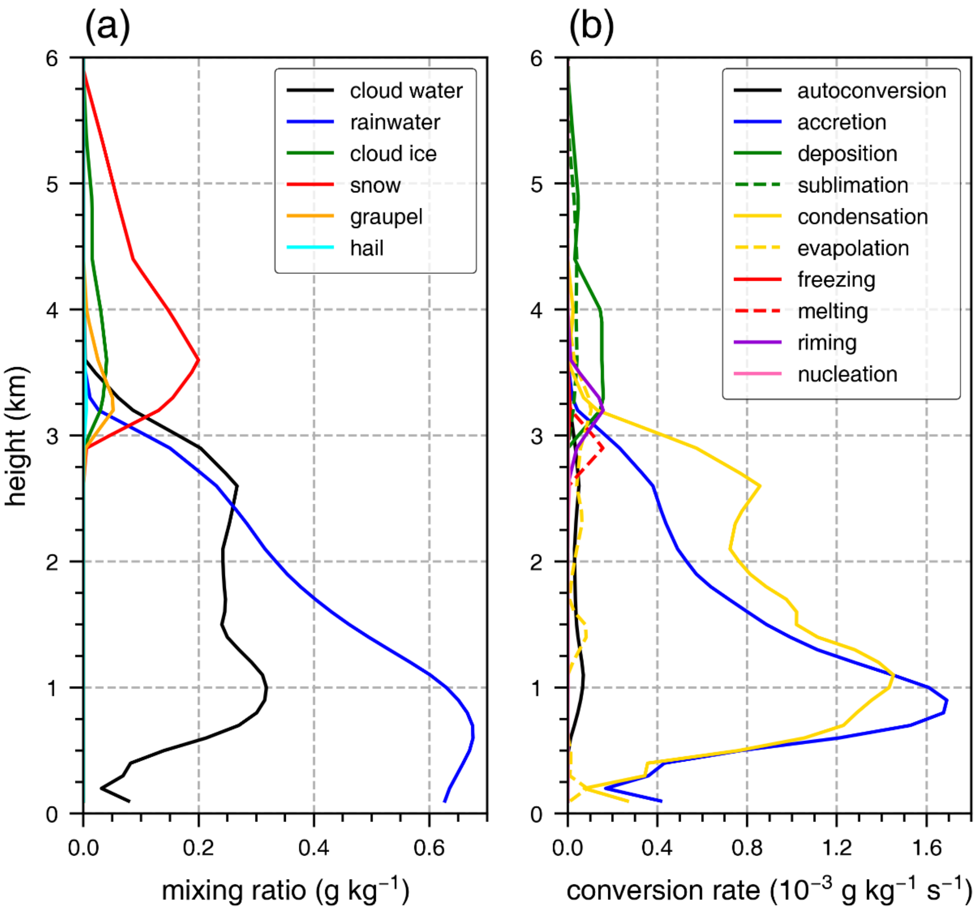

Figure 4.13 As in Fig. 4.11, but for P2.

of intermediate and large raindrops at the surface is still lower and that of small raindrops is still higher than the observation (Figure 7b). This implies that the collisional growth of raindrops in the simulation is weaker than that in reality.

Figure 4.14 shows the scatter plots of D_m and $\log_{10}N_w$ versus rain rate in the simulation and disdrometer observation in P2. D_m tends to increase as rain rate increases in both simulation and observation, indicating stronger collisional growth with increasing rain rate. However, for the whole range of rain rate, D_m of simulated RSD is relatively smaller than that of observed RSD at the same rain rate. Also, the simulation shows much larger $\log_{10}N_w$ than the observation for the same rain rate. This shows that the insufficient collisional growth in the simulation is present regardless of the various rain rate in P2. The prescription of aerosol number concentration in the bin microphysics scheme used in this study can be one reason for the insufficient collisional growth of raindrops. The collisional growth of raindrops can be sensitive to the aerosol number concentration because it affects the number concentration of cloud droplets and thus all relevant microphysical processes. A higher number concentration of cloud droplets with a given total mass indicates a smaller mean diameter of cloud droplets, which weakens autoconversion of cloud droplets into raindrops. Accretional growth of raindrops, on the other hand, can become stronger as there remain more cloud droplets to collect. The

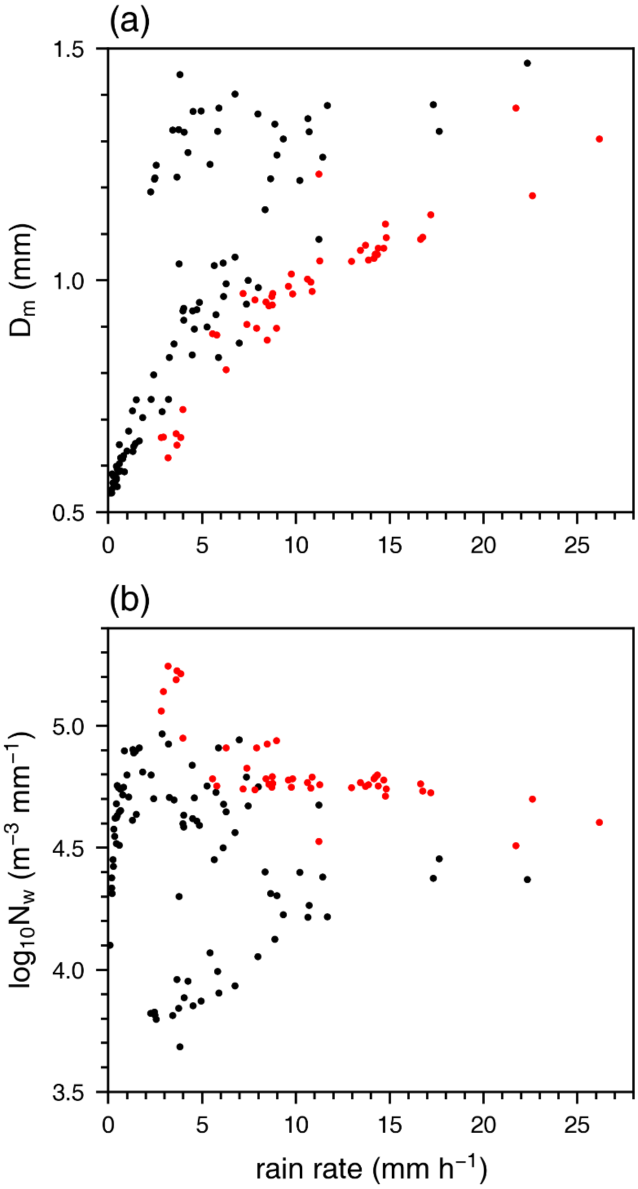

Figure 4.14 Scatter plots of (a) D_m and (b) $\log_{10}N_w$ versus rain rate at the disdrometer site in P2. Red and black dots indicate the simulation and disdrometer observation, respectively.

changes in the warm-rain collision–coalescence processes can result in a change in RSD. To quantitatively examine the contribution of prescribed aerosol number concentration to the RSD biases, further investigation with additional numerical simulations using different prescribed aerosol number concentrations is needed.

5 Impacts of aerosols on precipitation and raindrop size distribution in an extratropical cyclone system

5.1 Introduction

Aerosols can modify the radiative budget by both direct and indirect ways. The direct effects of aerosols refer to the absorption or scattering of incoming radiation by aerosols. Aerosols can also influence the radiation by acting as cloud condensation nuclei (CCN) or ice nuclei (IN). The increase of aerosols in the atmosphere can lead to an increase in the number of cloud droplets or a reduction in the width of droplet size distribution, then affecting the albedo or lifetime of clouds. This phenomenon is well known as aerosol indirect effects or aerosol-cloud interactions. Due to both their complexity and significant influences on weather and climate, aerosol-cloud interactions have received a lot of attention.

One of the complicating factors of aerosol-cloud interactions is that aerosol-cloud interactions can be different depending on cloud types (Fan et al., 2016). For shallow warm clouds, the increase of aerosols can lead to the reduction of droplet size and consequent increase of the amount of reflected solar radiation, which is known as the Twomey effect (Twomey 1977). For deep convective clouds, the reduction of droplet size and narrower droplet distribution suppress the warm rain processes, which can transport more cloud water to higher levels and cause more cloud water to freeze there. This leads to the enhanced latent heat and more invigorate convection.

Extratropical cyclones, a predominant precipitating system in South Korea, have various clouds along both cold and warm fronts (Field and Wood 2007). Various cloud types within this weather system make the aerosol-cloud interactions more complicated. In this chapter, aerosol-cloud interactions in the extratropical cyclone are examined through real case simulations with different initial aerosol concentrations. Furthermore, it will be investigated whether these complex aerosol-cloud interactions can affect the biases of raindrop size distribution shown in Chapter 4.

5.2 Simulation setup and methodology

5.2.1 Simulation setup

To investigate the sensitivity of precipitation and RSD to aerosol number concentration, five simulations with different initial aerosol concentrations (N_a = 100, 900, 2700, 8100, and 24300 cm^{-3}) are conducted. Except for the initial aerosol number concentration, the simulation case and setup are the same as those in Chapter 4.

In the modified version of Hebrew University Cloud Model (HUCM, Lee and Baik 2016) used as the microphysical parameterization in the simulations, the aerosol number concentration is predicted for 43 mass doubling bins with the largest radius of 2 μm. The initial size distribution of aerosol number concentration follows Khain et al. (2000).

$$\frac{dN}{d\ln r_a} = \frac{3}{2} N_a k \left(\frac{4A^3}{27Br_a^3}\right)^{\frac{k}{2}} \tag{5.1}$$

where N_a is the cloud condensation nuclei (CCN) number concentration at 1% supersaturation, r_a is the radius of aerosol particle, and k, A, and B are constants related to the hygroscopicity, curvature effect, and solution effect, respectively. The aerosol number concentration remains constant up to an altitude of 2 km, and above that altitude, it decreases exponentially according to the *e*-folding depth. It is assumed that all aerosol particles can act as CCN depending on their size and the ambient supersaturation.

5.2.2 Rain-type classification

The rain-type classification suggested by Steiner et al. (1995) is applied to investigate the sensitivity of different rain types (stratiform and convective rain) to aerosol number concentration. This classification method uses the field of equivalent radar reflectivity (Z_e) at the specific altitude. Here, the height of 1.5 km above the ground is selected to minimize errors caused by the bright band. The first step is the identification of convective center. There are two steps to identify the convective center. First, any grid point with Z_e value exceeding 40 dBZ is initially classified as convective center. Second, for grid points not identified as convective center in the first step, when the mean background Z_e, which is the averaged Z_e value within a radius of 10 km, exceeds the threshold value dependent on the mean background Z_e, the grid point is classified as a convective center. After the identification of convective centers, all grid points within the convective radius, determined by a function of mean background Z_e, at the convective center are also identified as convective rain. Next, among the grid points not classified as convective rain, those with Z_e values exceeding 10 dBZ are classified as stratiform rain, while those below this threshold value are identified as unclassified rain (Feng et al. 2011).

5.3 Results and discussion

5.3.1 General characteristics of simulated

precipitation

Figure 5.1 shows the spatial distribution of accumulated precipitation amount predicted in five simulations with different initial aerosol number concentrations. All simulations exhibit a linear distribution of accumulated precipitation amount, extending from the southwestern overseas region to the northeastern inland region. There seems to be a little difference in the amount of accumulated precipitation amount. To clarify the difference in precipitation, the time series of rain rate and accumulated precipitation averaged over the analysis area denoted by a red rectangle in Fig. 5.1 are shown in Fig. 5.2. Note that all subsequent analyses are conducted in the analysis area. In all simulations, weak precipitation continuously occurs until 0600 LST, and then the rain rate increases rapidly, peaking at 0858–0936 LST and then decreasing. The most noticeable difference between the simulations is that those with high aerosol number concentrations (N_a = 8100 and 24300 cm^{-3}) exhibit higher rain rate and accumulated precipitation amount.

Accumulated rain amount, the ratio of rain area to total area, and rain rate averaged over the analysis area for the total, stratiform rain, and convective rain are shown in Fig. 5.3. For the total, accumulated rain amount

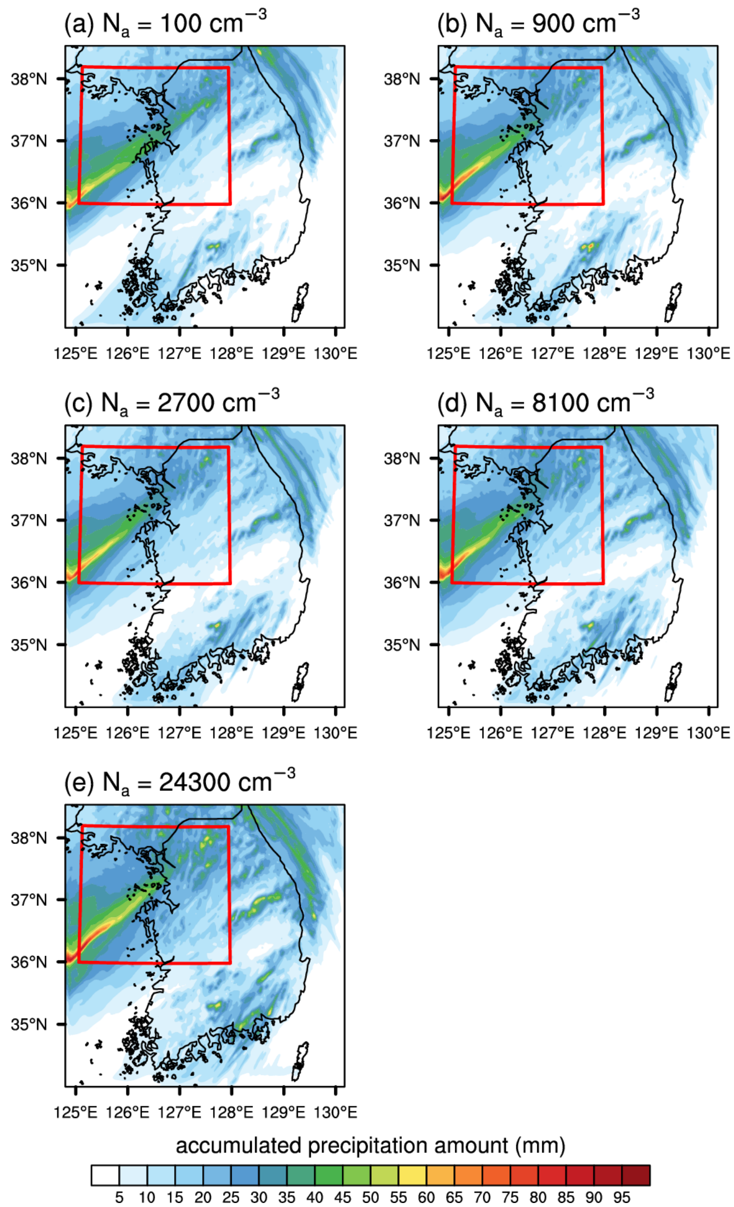

Figure 5.1 12-h accumulated precipitation amounts in the simulations with initial aerosol number concentrations of N_a = (a) 100, (b) 900, (c) 2700, (d) 8100, and (e) 24300 cm^{-3}.

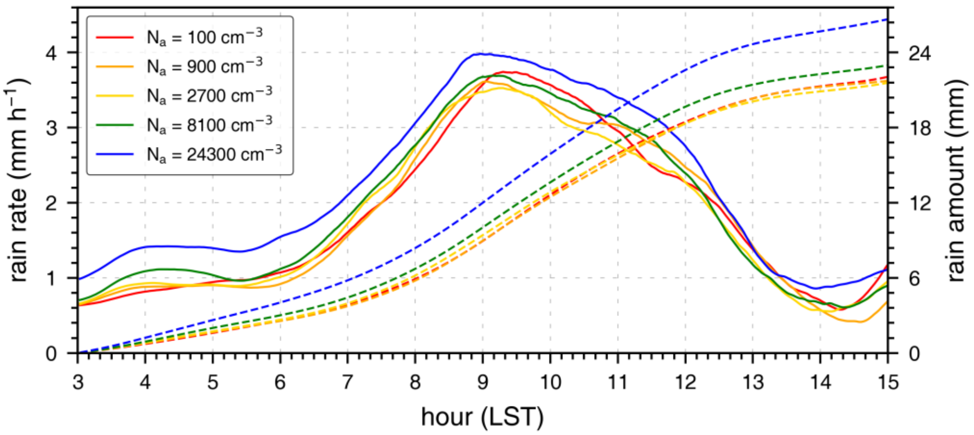

Figure 5.2 Time series of rain rates (solid lines) and accumulated rain amounts (dashed lines) in the simulations with different initial aerosol number concentrations (N_a = 100, 900, 2700, 8100, and 24300 cm^{-3}).

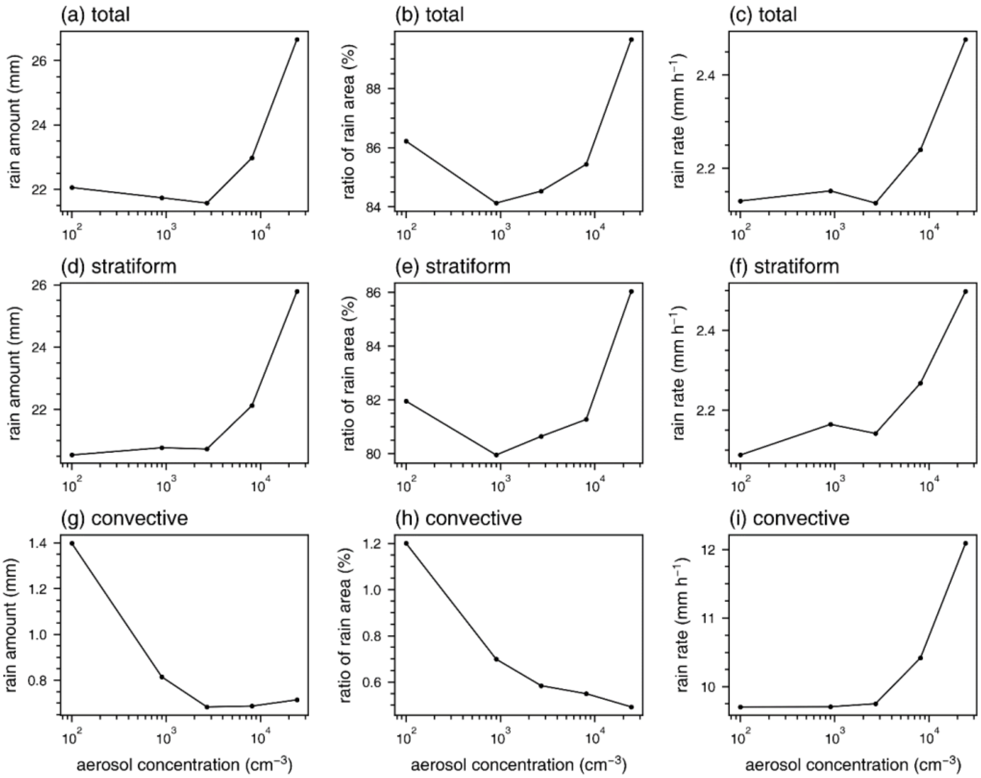

Figure 5.3 (a,d,g) Accumulated rain amount, (b,e,h) ratio of rain area to total area, and (c,f,i) rain rate averaged over the analysis area for (a,b,c) the total, (d,e,f) stratiform rain, and (g,h,i) convective rain as a function of initial aerosol number concentration.

slightly decreases up to N_a = 2700 cm^{-3}, and then increases abruptly with increasing N_a. The ratio of rain area to total area decreases up to N_a = 900 cm^{-3}, and then increases with increasing N_a. Rain rate, which is the ratio of rain amount to rain area, remains almost constant until N_a = 2700 cm^{-3}, and then increases significantly as N_a increases. For the stratiform rain, due to its high proportion to the total, the accumulated rain amount, ratio of rain area to total area, and rain rate exhibit almost the same trend to the total. Contrary to the stratiform rain, convective rain shows a decreasing trend for both accumulated rain amount and ratio of rain area to the total. For rain rate, convective rain shows an increasing trend like stratiform rain.

5.3.2 Response of convective rain to increasing N_a

To examine the response of convective rain to increasing aerosol number concentration (N_a), time- and area-averaged vertical profiles of hydrometeors and conversion rates are plotted in Fig. 5.4 and Fig. 5.5, respectively. The increase in N_a primarily affects the production of cloud water through nucleation. Enhanced nucleation with increasing N_a results in the increase in the number concentration of cloud droplets (Fig. 5.4a), while the mean size of cloud droplets decreases due to competition for a limited amount of water vapor (Fig. 5.4b). The decrease in the mean size of cloud

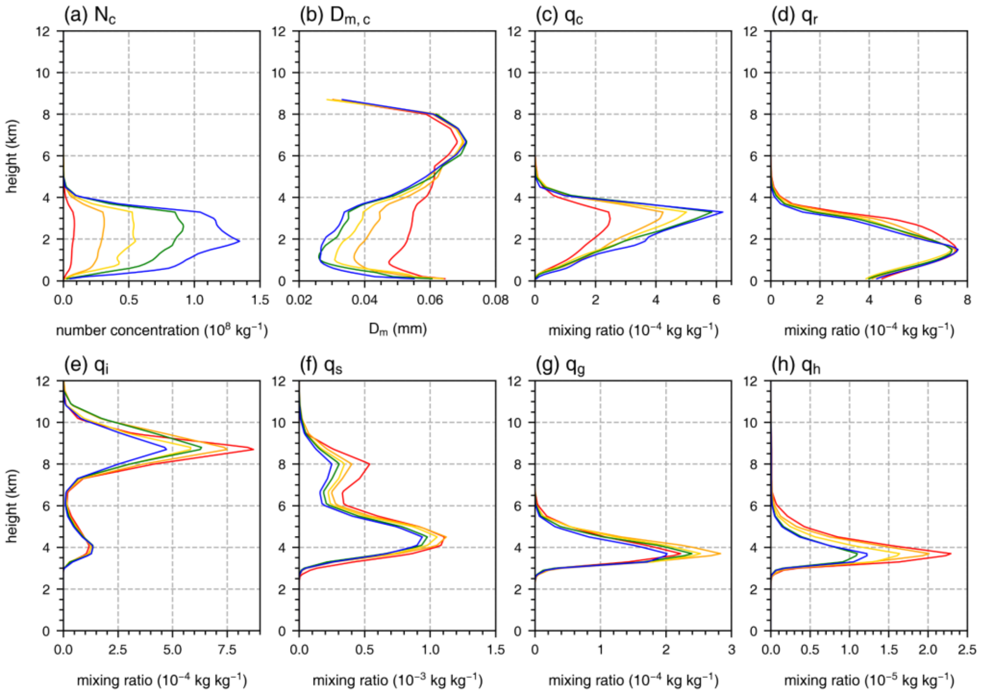

Figure 5.4 Vertical profiles of time- and area-averaged (a) number concentration and (b) mass-weighted diameter (D_m) for cloud droplets, and mixing ratios for (c) cloud water, (d) rainwater, (e) cloud ice, (f) snow, (g) graupel, and (h) hail for convective rain.

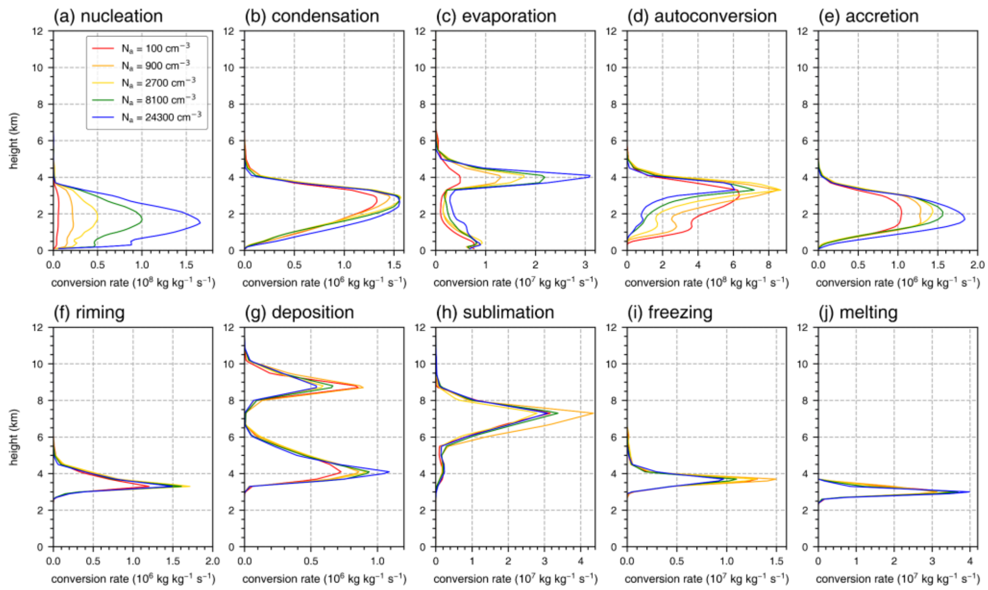

Figure 5.5 Vertical profiles of time- and area-averaged conversion rates of (a) nucleation, (b) condensation, (c) evaporation, (d) autoconversion, (e) accretion, (f) riming, (g) deposition, (h) sublimation, (i) freezing, and (j) melting for convective rain.

droplets reduces the collection efficiency between cloud droplets. As a result, the autoconversion rate decreases with increasing N_a (Fig. 5.5d). Contrary to the decreased autoconversion rate, the accretion and riming rates increase with increasing N_a (Figs. 5.5e and 5.5f). This is because the raindrop and snowflakes have more chances to collect the small-size cloud droplets compared to other cloud droplets. The increase in the number concentration of cloud droplets leads to the increase in condensation rate (Fig. 5.5b) due to the increase in total surface area of cloud droplets.

The increased condensation rate has two different effects. First, the latent heat release intensifies due to the increase in condensation rate with increasing N_a. The intensified latent heat can drive a stronger updraft. Figure 5.6 shows the vertical profiles of latent heat, supersaturation, and vertical velocity. The intensification of latent heat and updraft with increasing N_a are clearly shown in Fig. 5.6. Second, with increasing N_a, supersaturation is not accumulated due to the large condensation rate, resulting in a drier upper layer. Because of this effect, the evaporation rate is larger in the simulations with higher N_a. Simultaneously, the deposition rate is larger in the simulations with higher N_a, indicating that the active Wegener-Bergeron-Findeisen process occur at this height.

Because of the large conversion rate related to the ice hydrometeors such as riming and deposition, the conversion from ice hydrometeors to

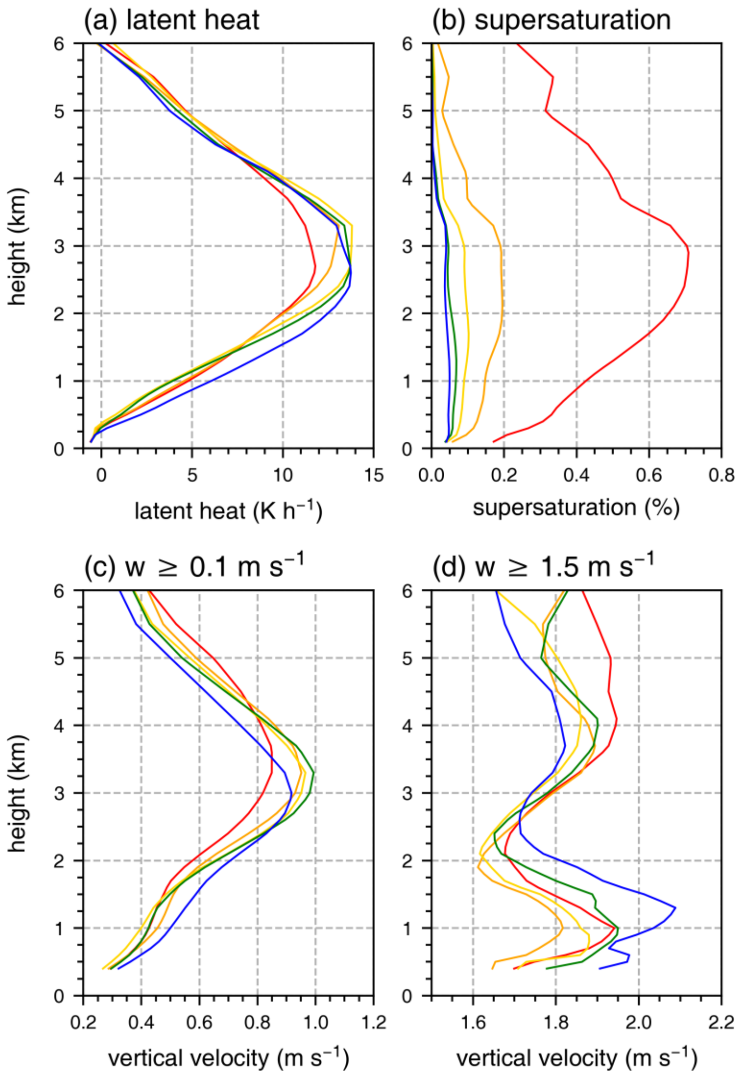

Figure 5.6 Vertical profiles of (a) latent heat, (b) supersaturation, (c) vertical velocity larger than 0.1 m s^{-1}, and (d) vertical velocity larger than 1.5 m s^{-1}.

rainwater by melting is relatively small. This means that the ice hydrometeors produced in convective rain may be advected to the other area. Figure 5.7 shows the spatial distributions of snow water path and stratiform area at 0600 LST. In both simulations, snow is widely distributed over the area of stratiform rain, providing the support for the possibility of snow advection from the area of convective rain. In addition, the stratiform area and snow are more widely distributed in the simulation with $N_a = 24300\ cm^{-3}$. Considering that the conversion processes related to ice hydrometeors are larger in the higher N_a simulations, the increase in the stratiform area with increasing N_a may be related to the advected snow from convective rain. Figure 5.8 shows the time-height plot for mixing ratios of liquid and ice hydrometeors at Seoul site. The convective systems in the simulation with $N_a = 100\ cm^{-3}$ are more organized than those in the simulation with $N_a = 24{,}300\ cm^{-3}$. This implies that the decrease in convective area may be related to the different structures of the convective systems.

Figure 5.9 shows the raindrop size distributions simulated in all simulations and their ratios to the RSD in the simulation with $N_a = 100\ cm^{-3}$. All simulations consistently predict the RSD, where $N(D)$ increases up to $D \sim 0.8$ mm with increasing diameter and then decreases. However, there are some differences depending on the diameter range. In the small diameter range ($D < 1$ mm), the simulation with higher N_a predicts smaller $N(D)$. This

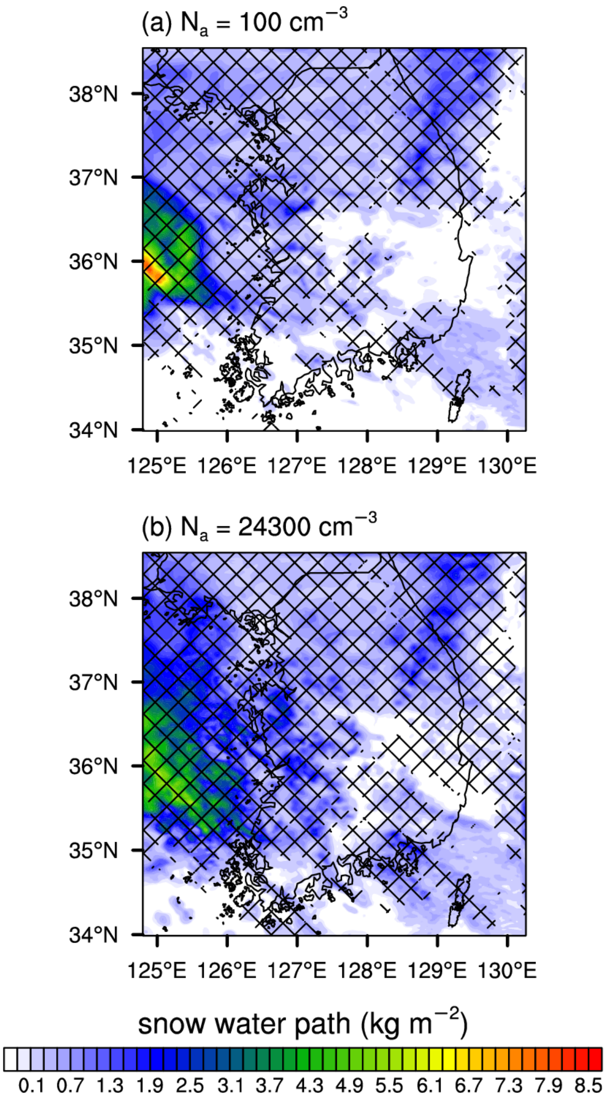

Figure 5.7 Snow water path (contoured) in the simulations with (a) N_a = 100 cm^{-3} and (b) N_a = 24300 cm^{-3} at 0600 LST. The shaded area represents the area classified as stratiform rain.

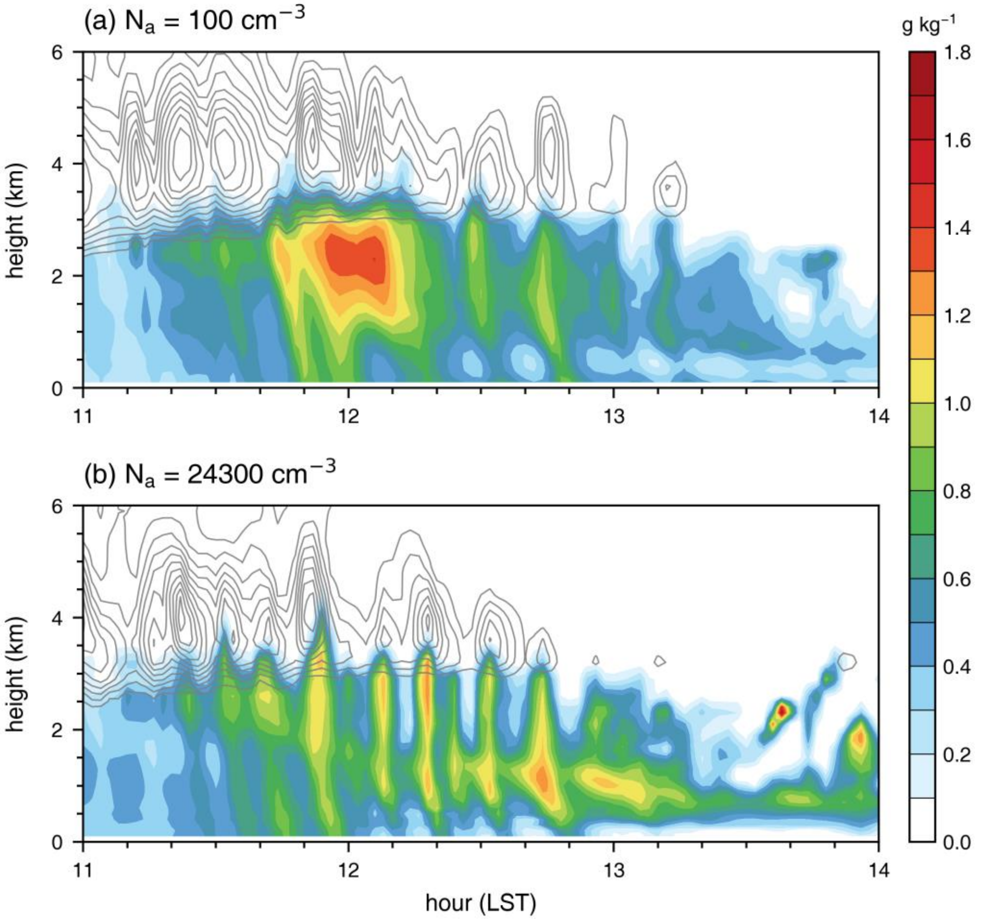

Figure 5.8 Time-height plots for mixing ratios for liquid and ice hydrometeors in the simulations with (a) N_a = 100 cm^{-3} and (b) N_a = 24300 cm^{-3} at Seoul site.

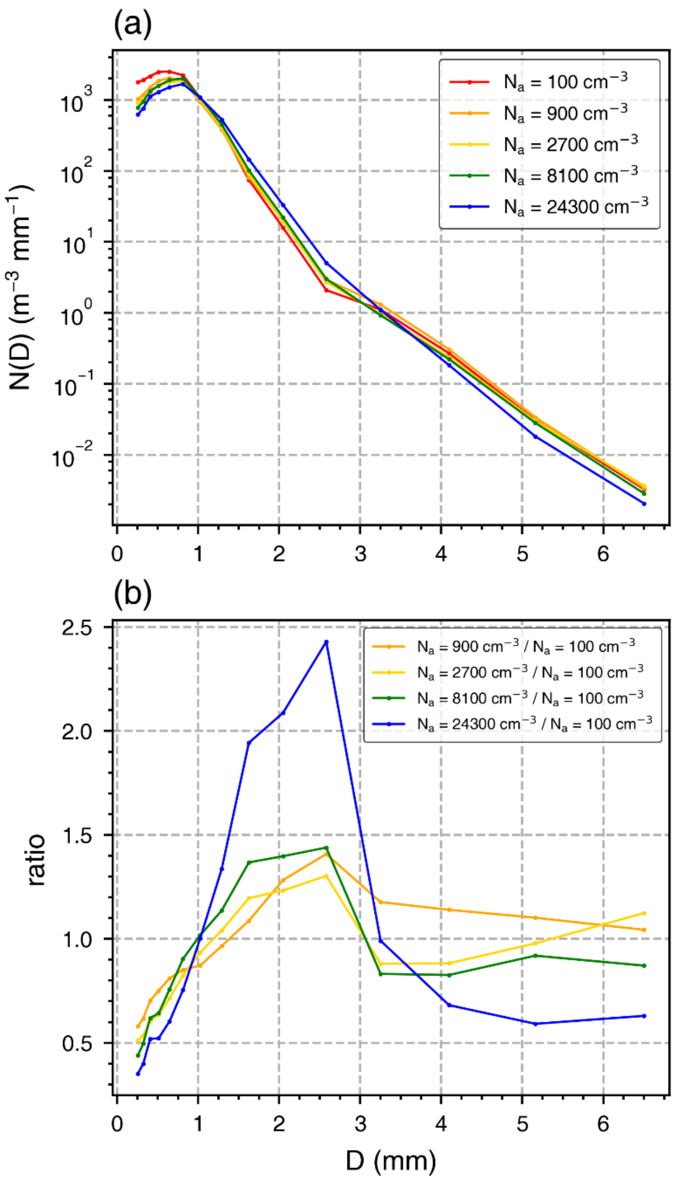

Figure 5.9 (a) Raindrop size distributions for convective rain and (b) their ratios to the raindrop size distributions in the simulation with $N_a = 100\ \mathrm{cm^{-3}}$.

is mainly due to the decreased autoconversion rate, resulting in the reduction of small-size raindrops. In the intermediate diameter range (D = 1–3 mm), the simulation with higher N_a predicts larger $N(D)$. In the simulation with higher N_a, the accretion rate is larger compared to that with lower N_a. Because of the increase in accretion rate, the number concentration of raindrops in the intermediate diameter range significantly increases. This implies that the increase in the rain rate with increasing N_a is mainly due to the increased $N(D)$ in the intermediate diameter range from increased accretion rate.

5.3.3 Response of stratiform rain to increasing N_a

As examined in convective rain, the response of stratiform rain to increasing aerosol number concentration (N_a) is investigated through time- and area-averaged vertical profiles of hydrometeors and conversion rates (Fig. 5.10 and Fig. 5.11). Stratiform rain also experienced an increase in nucleation, similar to convective rain. As a result, the number concentration of cloud drops increases, while the mean size of cloud drops decreases. The autoconversion rate decreases due to the decrease in the mean size of cloud drops, and the accretion and riming rates increase due to the increase in remaining cloud water mass.

There are two distinct features that do not appear in convective rain.

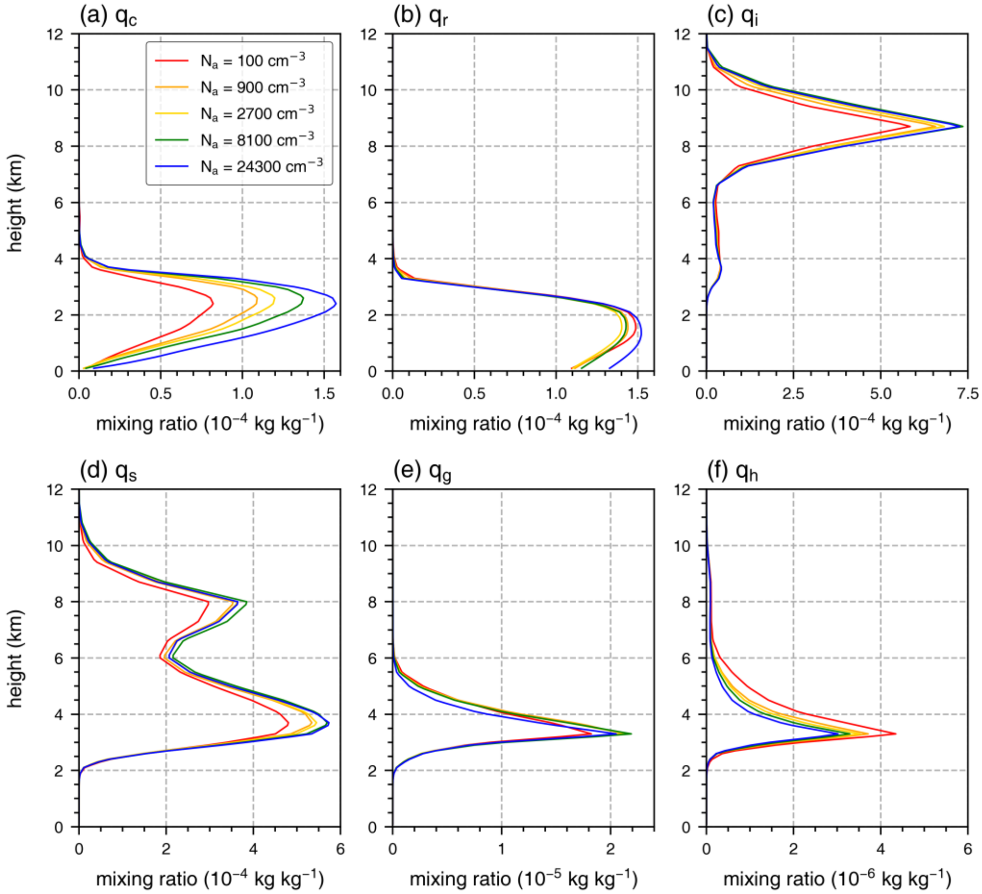

Figure 5.10 Vertical profiles of time- and area-averaged mixing ratios for (a) cloud water, (b) rainwater, (c) cloud ice, (d) snow, (e) graupel, and (f) hail.

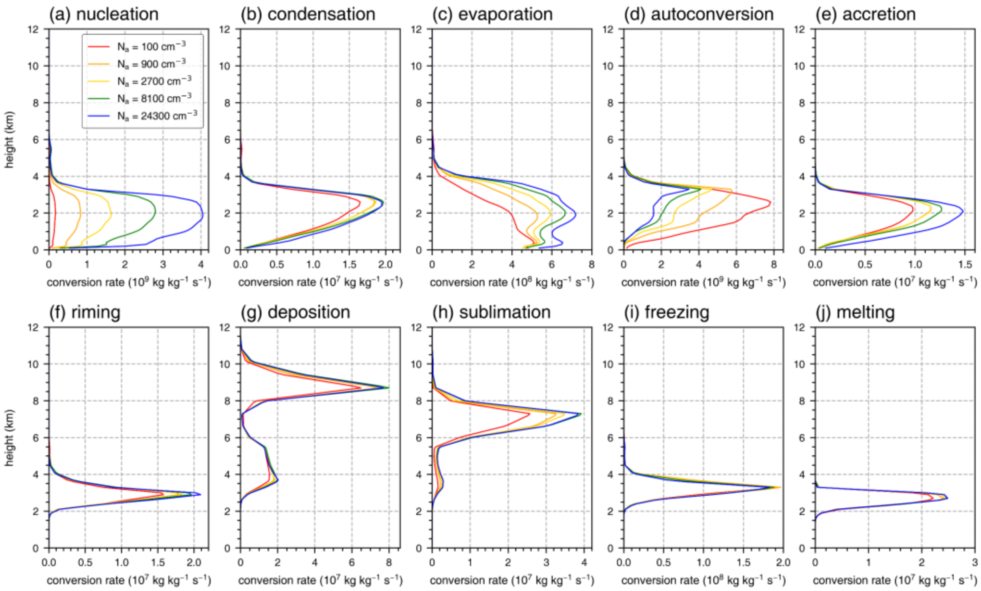

Figure 5.11 As in Fig. 5.5, but for stratiform rain.

First, there is no warm-phase invigoration. Compared to convective rain which shows more enhanced latent heat and vertical velocity with increasing N_a, there is almost no significant difference in latent heat release between the simulations, which consequently leads to similar vertical velocities. Second, the melting rate is comparable to accretion and riming rates. Unlike in convective rain, where melting is one order of magnitude lower than accretion, in stratiform rain, melting and accretion have a comparable magnitude. This means that the contribution of ice hydrometeors is more prominent in stratiform rain than in convective rain.

Figure 5.12 shows the raindrop size distributions for stratiform rain in all simulations and their ratios to the RSD in the simulation with N_a = 100 cm^{-3}. In all simulations, the peak at D = 3.3 mm commonly appears. For this peak, the simulations with high N_a (8100 and 24300 cm^{-3}) show the increase in $N(D)$. Given that melting is the process that exhibited the most significant difference compared to convective rain, it is attributed to the supply of relatively large raindrops from the melting of snow. As in convective rain, the enhancement of autoconversion and accretion with increasing N_a results in the decrease in $N(D)$ in the small diameter range and increase in the intermediate diameter range. The changes in $N(D)$ due to the increases in accretion and melting rates lead to an increase in the rain rate of stratiform rain.

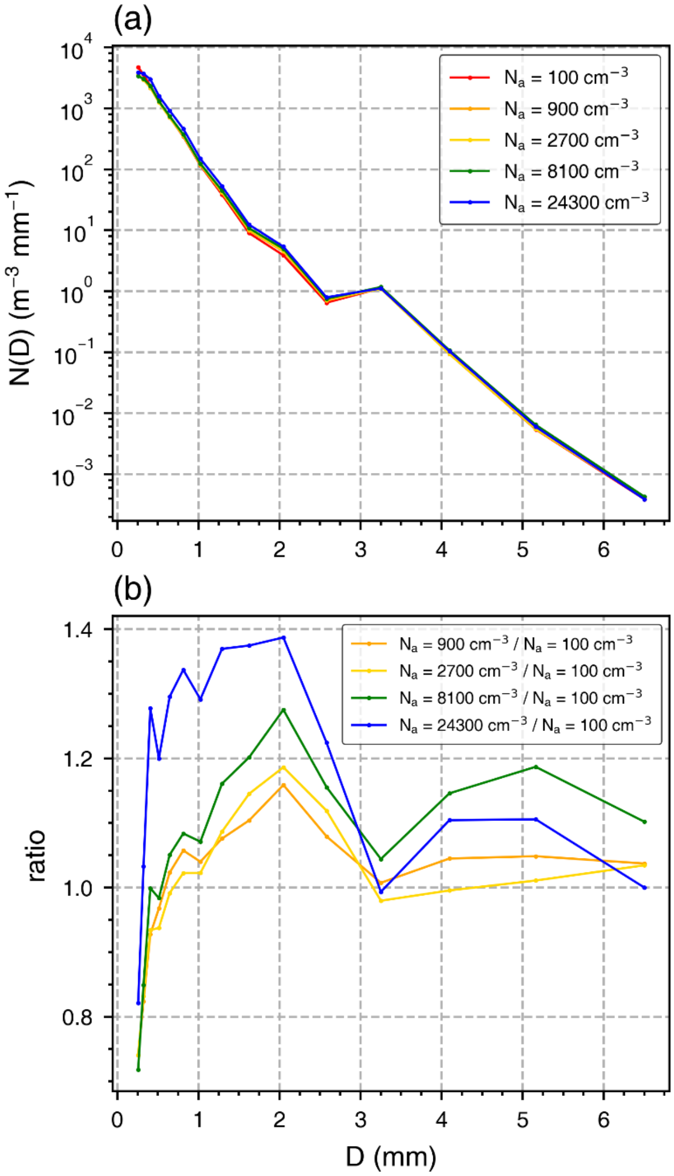

Figure 5.12 As in Fig. 5.9, but for stratiform rain.

6 Summary and conclusions

In Chapter 2, the differences in RSD characteristics among three cities (Seoul, Chuncheon, and Jincheon) in South Korea were examined using disdrometer data for the period from 25 July 2018 to 31 July 2021 and the their possible causes were investigated utilizing the ERA5 reanalysis data. Seoul is the most populated city in South Korea, Chuncheon is a medium-sized city located in a basin, and Jincheon is the least populated and southernmost city among the three cities. The three cities show clear differences in precipitation and RSD characteristics. Jincheon is characterized by the smallest mean rainfall intensity and a relatively high frequency of light rain, which are associated with the smallest D_m and the largest $\log_{10}N_w$. Chuncheon, on the other hand, is characterized by the largest mean rainfall intensity and a relatively high frequency of heavy rain, which are associated with the largest D_m and the smallest $\log_{10}N_w$. The contrasts in RSD characteristics between the two cities can be attributable to the relatively large convective available potential energy, high cloud-top height, and low cloud-base height in Chuncheon compared to those in Jincheon. Seoul is characterized by the intermediate mean rainfall intensity associated with D_m and $\log_{10}N_w$ that are intermediate between those in Jincheon and Chuncheon. In Seoul, extreme rainfall events occurs most frequently and D_m for very heavy rain is relatively large. This can be attributable to the most frequent occurrence of large convective available potential energy.

This study showed that the regional differences in RSD characteristics among the cities can be attributable to the regional differences in thermodynamic and cloud characteristics. Different urban characteristics and geographical characteristics of the cities can cause the differences in thermodynamic and cloud characteristics. Besides, as urban aerosols can serve as cloud condensation nuclei, different aerosol concentrations in the cities can cause differences in cloud microphysics among the cities. How these individual factors contribute to the regional differences in thermodynamical and cloud microphysical characteristics among the cities cannot be revealed under the analysis framework of this study, which is a limitation of this work. This deserves further investigation, in which various types of data such as radar observation data, satellite retrievals of cloud properties, atmospheric sounding data, and aerosol concentration data for each city need to be utilized.

In Chapter 3, the diagnostic relations for the intercept parameter of the exponential raindrop size distribution N_0 for different rain types (stratiform, mixed, and convective) were derived using the disdrometer data and their impacts on precipitation prediction were examined. The disdrometer data observed at four sites (Seoul, Chuncheon, Jincheon, and Boseong) in

South Korea show spatiotemporal variations of N_0. The diagnostic relations derived using three different methods (DNW, DNL, DMM) with and without the rain-type classification are evaluated, and DNW with the rain-type classification, which best reproduces the observed N_0, is selected. DNW is implemented into the WSM6 scheme, and its impacts are investigated through the simulations of summertime precipitation events in South Korea. Compared to the WSM6-O simulation using a constant N_0, the WSM6-L simulation using the diagnostic relation yields better precipitation prediction. The diagnostic relation greatly improves the representation of N_0, which is observed to have a large variability. Also, the WSM6-L simulation predicts N_0 that is on average smaller than the prescribed value in the WSM6-O simulation, which agrees with the observation to some extent. The smaller N_0 in the WSM6-L simulation decreases the rainwater mixing ratio by reducing the accretion of cloud water and the melting of ice hydrometeors and also decreases the rainwater evaporation.

The potential of the use of diagnostic relation for N_0 in a single-moment microphysics scheme for better precipitation prediction was confirmed. However, the advantage of using the diagnostic relation may be more prominent if the dependence of microphysical processes on varying N_0 is well represented in their parameterizations in the single-moment microphysics scheme. For example, when two exponential RSDs have the same rainwater content but different N_0, it is generally expected that the rate of accretion of cloud water is larger for the RSD with smaller N_0 that has a larger number of large-size raindrops and a smaller number of small-size raindrops because the collection efficiency between raindrops and cloud droplets is higher for large raindrops than for small raindrops. However, the accretion rate in the WSM6 microphysics scheme is designed to decrease as N_0 decreases because it uses the collection efficiency that does not depend on the raindrop size. If the dependence of the accretion rate on the RSD properties is represented as in either simple (Thompson et al. 2008) or sophisticated (Ahmed et al. 2020) way, the impact of diagnostic relation may be more pronounced.

The appropriate diagnostic relation for N_0 for one region can be different from that for another region. DNW in this study and DNW of Z08 were derived using the same derivation method, but DNW in this study better reproduced the observed N_0 in South Korea because the relation was derived using the disdrometer data in South Korea. The diagnostic relation of AB12 also showed poor performance in reproducing N_0 in South Korea although it was derived using RSD data from various regions around the world. This indicates that to make the best use of diagnostic relation for N_0 in predicting precipitation in a region, it is encouraged to use the diagnostic relation derived from that region. Ideally, for global weather prediction models, a set of diagnostic relations for different regions can be developed and employed in the model to improve precipitation prediction.

Although the diagnostic relation for N_0 that considers the rain-type classification shows stronger correlation between the estimated and diagnosed N_0 than the diagnostic relation that does not consider the rain-type classification, the correlation coefficient is 0.24, which means that a large part of the N_0 variation is not represented by the rainwater content and the rain type only. It can be expected that RSD can vary depending on the cloud characteristics such as the dominant microphysical process (Dolan et al. 2018) and the stage of cloud development, but it is not easy to establish a sophisticated diagnostic relation for N_0 utilizing those factors because it needs three-dimensional observations of RSD and in-cloud environment for various types of clouds, which is not available for now. In a future study, extensive numerical simulations of various types of clouds using a bin microphysics scheme may be done to obtain reliable three-dimensional RSD data and in-cloud environment data at the same time, which can be used to establish a more sophisticated diagnostic relation for N_0 that better represents the variation of N_0.

In Chapter 4, evaluation for the raindrop size distributions simulated using a bin microphysics scheme was performed through comparison with disdrometer observations, for a precipitation event associated with an extratropical cyclone passing South Korea. The mean RSD is overall well reproduced, but notable overestimations are seen in the small- and large-diameter ranges. The overestimation in large-diameter range is prominent in P1, when stratiform rain is predominant, and it is characterized by the appearance of a local maximum in RSD at D = 3.3 mm, which is not seen in the observed RSDs. This spurious local maximum originates from upper levels, where ice–ice collection generates a local maximum in snow size distribution, which is converted into that in RSD below the melting layer. Insufficient depletion of raindrops through breakup could be another reason for the overestimation of large raindrops in P1. The overestimation in small-diameter range is prominent in P2, when convective rain is largely involved. The warm-rain collision–coalescence is the largest contributor to RSDs in this period, but the RSD comparison shows that this process should have been represented to be stronger in the simulation.

Unlike bulk microphysics schemes that employ typical forms of particle size distributions that are obtained from observations, bin microphysics schemes allow any shape of distributions, which indicates that the particle size distributions in bin microphysics schemes are solely determined by physical processes. As a result, the issues in the representation of each physical process can be more apparently reflected in the simulated size distributions. This is exemplified by the spurious local maximum at D =

3.3 mm simulated in P1 that was found to be originated from the overly active ice–ice collection at upper levels. Consequently, evaluating simulated RSDs of a precipitation event can be an effective way of identifying deficiencies in the parameterizations of specific processes that significantly affect RSDs in the event. Considering together with different RSD characteristics depending on the type of precipitation system (Jwa et al., 2021; Loh et al., 2019), this suggests the need for similar investigations for other types of precipitation systems where other microphysical processes make significant contributions to RSDs.

In Chapter 5, the impacts of aerosols on precipitation and raindrop size distribution in an extratropical cyclone are examined by five simulations with different initial aerosol number concentrations (N_a = 100, 900, 2700, 8100, and 24300 cm^{-3}). When N_a increases, the impacts of aerosols on precipitation and raindrop size distribution differ depending on the rain type. For convective rain, enhanced nucleation process with increasing N_a increases the number of cloud droplets and decreases the mean size of cloud droplets. The decrease in the mean size of cloud droplets results in smaller autoconversion rates due to the reduction in collection efficiency between cloud droplets, while the accretion and riming rates increase due to the increase in the number of small-size cloud droplets. The increases in the number of cloud droplets enable more water vapor to be condensed, resulting in the enhanced latent heat release. The enhanced latent heat release induces stronger updrafts, which is known as warm-phase aerosol invigoration. In addition, the enhanced condensation with increasing N_a consumes more supersaturation in the lower level, resulting in the drier upper level. Due to the drier upper level, there is a strong Wegener-Bergeron-Findeisen process. Despite the stronger ice-related microphysical processes such as riming and Wegener-Bergeron-Findeisen processes in higher N_a simulations, the conversion from snow to rainwater by melting is relatively weak, which may imply the advection of snow to stratiform rain. As a result, the increase in rain rate for convective rain is mainly due to the enhanced accretion process and warm-phase invigoration. One of the reasons for the decrease in the area of convective rain is the degree of organization with different aerosol number concentrations. For stratiform rain, both liquid- and ice-related processes are similarly involved. As in the convective rain, autoconversion decreases and accretion and riming increase. However, the conversion rate of melting is comparable to those of the accretion and riming processes. It seems that a large amount of snow produced in the area of convective rain is advected, which may be attributed to the increase in the area of stratiform rain, and converted to the rainwater. So, the main reason for the increase in rain rate is both large accretion and melting rates.

Both in convective and stratiform rain, accretion increases the number concentration of raindrops in the intermediate diameter range (D = 1–3 mm). In the large diameter range (D > 3 mm), larger melting in stratiform rain makes a more prominent peak at D = 3.3 mm. In Chapter 4, the simulated RSD is overestimated in this range. Considering that N_a = 900–8100 cm^{-3} is the realistic range of aerosol number concentrations, the prescription of a realistic aerosol number concentrations does not reduce the biases in simulated RSDs. This means that the biases in simulated RSDs may be originated from more systematic errors in microphysics parameterizations.

References

Abel, S. J., and I. A. Boutle, 2012: An improved representation of the raindrop size distribution for single-moment microphysics schemes. *Quart. J. Roy. Meteor. Soc.*, **138**, 2151–2162.

Ahmed, T., H.-G. Jin, and J.-J. Baik, 2020: A physically based raindrop–cloud droplet accretion parametrization for use in bulk microphysics schemes. *Quart. J. Roy. Meteor. Soc.*, **146**, 3368–3383.

Angulo-Martínez, M., S. Beguería, B. Latorre, and M. Fernández-Raga, 2018: Comparison of precipitation measurements by OTT Parsivel^2 and Thies LPM optical disdrometers. *Hydrol. Earth Syst. Sci.*, **22**, 2811–2837.

Atlas, D., R. C. Srivastava, and R. S. Sekhon, 1973: Doppler radar characteristics of precipitation at vertical incidence. *Rev. Geophys. Space Phys.*, **11**, 1–35.

Bang, W., S. Kwon, and G. Lee, 2017: Characteristic of raindrop size distribution using two-dimensional video disdrometer data in Daegu, Korea. *J. Korean Earth Sci. Soc.*, **38**, 511–521.

Bretherton, C. S., and S. Park, 2009: A new moist turbulence parameterization in the community atmosphere model. *J. Clim.*, **22**, 3422–3448.

Bringi, V. N., V. Chandrasekar, J. Hubbert, E. Gorgucci, W. L. Randeu, and

M. Schoenhuber, 2003: Raindrop size distribution in different climatic regimes from disdrometer and dual-polarized radar analysis. *J. Atmos. Sci.,* **60**, 354–365.

Bringi, V. N., C. R. Williams, M. Thurai, and P. T. May, 2009: Using dual-polarized radar and dual-frequency profiler for DSD characterization: A case study from Darwin, Australia. *J. Atmos. Ocean. Technol.*, **26**, 2107–2122.

Cao, Q., and G. Zhang, 2009: Errors in estimating raindrop size distribution parameters employing disdrometer and simulated raindrop spectra. *J. Appl. Meteorol. Climatol.*, **48**, 406–425.

Chen, B., Z. Hu, L. Liu, and G. Zhang, 2017: Raindrop size distribution measurements at 4,500 m on the Tibetan Plateau during TIPEX-III. *J. Geophys. Res. Atmos.*, **122**, 11092–11106.

Chen, B., J. Yang, R. Gao, K. Zhu, C. Zou, Y. Gong, and R. Zhang, 2020: Vertical variability of the raindrop size distribution in typhoons observed at the Shenzhen 356-m meteorological tower. *J. Atmos. Sci.*, **77**, 4171–4187.

Chen, G., K. Zhao, H. Huang, Z. Yang, Y. Lu, and J. Yang, 2021: Evaluating simulated raindrop size distributions and ice microphysical processes with polarimetric radar observations in a Meiyu front event over eastern China. *J. Geophys. Res. Atmos.*, **126**, e2020JD034511.

Chen, G., Y. Lu, S. Hua, Q. Liu, K. Zhao, Y. Zheng, M. Wang, S. Zhang, X. Wang, 2023: Evaluating the variability of simulated raindrop size distributions in the “21·7” Henan extremely heavy rainfall event. *Geophys. Res. Lett.*, **50**, e2023GL102849.

Chen, Y., J. Duan, J. An, and H. Liu, 2019: Raindrop size distribution characteristics for tropical cyclones and Meiyu-Baiu fronts impacting Tokyo, Japan. *Atmosphere* **10**, 391.

Dolan, B., B. Fuchs, S. A. Rutledge, E. A. Barnes, and E. J. Thompson, 2018: Primary modes of global drop size distributions. *J. Atmos. Sci.* **75**, 1453–1476.

Dudhia, J., 1989: Numerical study of convection observed during the Winter Monsoon Experiment using a mesoscale two-dimensional model. *J. Atmos. Sci.* **46**, 3077–3107.

Fan, J., Y. Wang, D. Rosenfeld, and X. Liu, 2016: Review of aerosol-cloud interactions: Mechanisms, significance, and challenges. *J. Atmos. Sci.*, **73**, 4221–4252.

Feng, Z., X. Dong, B. Xi, C. Schumacher, P. Minnis, and M. Khaiyer, 2011: Top-of-atmosphere radiation budget of convective core/stratiform rain and anvil clouds from deep convective systems. *J. Geophys. Res. Atmos.* **116**, D23202.

Field, P. R., and R. Wood, 2007: Precipitation and cloud structure in midlatitude cyclones. *J. Clim.*, **20**, 233–254.

Fridlind, A. M., X. Li, D. Wu, M. van Lier-Walqui, A. S. Ackerman, W.-K. Tao, G. McFarquhar, W. Wu, X. Dong, J. Wang, A. Ryzhkov, P. Zhang, M. R. Poellot, A. Neumann, J. M. Tomlinson, 2017: Derivation of aerosol profiles for MC3E convection studies and use in simulations of the 20 May squall line case. *Atmos. Chem. Phys.*, **17**, 5947–5972.

Giangrande, S. E., M. J. Bartholomew, M. Pope, S. Collis, and M. P. Jensen, 2014: A summary of precipitation characteristics from the 2006-11 Northern Australian wet seasons as revealed by ARM disdrometer research facilities (Darwin, Australia). *J. Appl. Meteorol. Climatol*,. **53**, 1213–1231.

Grabowski, W. W., H. Morrison, S. I. Shima, G. C. Abade, P. Dziekan, and H. Pawlowska, 2019: Modeling of cloud microphysics: Can we do better? *Bull. Am. Meteorol. Soc.*, **100**, 655–672.

Han, Y., J. Guo, Y. Yun, J. Li, X. Guo, Y. Lv, D. Wang, L. Li, and Y. Zhang, 2021: Regional variability of summertime raindrop size distribution from a network of disdrometers in Beijing. *Atmos. Res.*, **257**, 105591.

Hernández Pardo, L., L. A. T. Machado, H. Morrison, M. A. Cecchini, M. O. Andreae, C. Pöhlker, U. Pöschl, D. Rosenfeld, E. P. Vendrasco, C. Voigt, M. Wendisch, and M. L. Pöhlker, 2021: Observed and simulated variability of droplet spectral dispersion in convective clouds over the Amazon. *J. Geophys. Res. Atmos.*, **126**, e2021JD035076.

Hersbach, H., B. Bell, P. Berrisford, S. Hirahara, A. Horányi, J. Muñoz-Sabater, J. Nicolas, C. Peubey, R. Radu, D. Schepers, A. Simmons, C. Soci, S. Abdalla, X. Abellan, G. Balsamo, P. Bechtold, G. Biavati, J. Bidlot, M. Bonavita, G. De Chiara, P. Dahlgren, D. Dee, M. Diamantakis, R. Dragani, J. Flemming, R. Forbes, M. Fuentes, A. Geer, L. Haimberger, S. Healy, R. J. Hogan, E. Hólm, M. Janisková, S. Keeley, P. Laloyaux, P. Lopez, C. Lupu, G. Radnoti, P. de Rosnay, I. Rozum, F. Vamborg, S. Villaume, and J. N. Thépaut, 2020: The ERA5 global reanalysis. *Quart. J. Roy. Meteor. Soc.*, **146**, 1999–2049.

Hong, S.-Y., and J.-O. J. Lim, 2006: The WRF single-moment 6-class microphysics scheme (WSM6). *J. Korean Meteorol. Soc.*, **42**, 129–151.

Hong, S.-Y., Y. Noh, and J. Dudhia, 2006: A new vertical diffusion package with an explicit treatment of entrainment processes. *Mon. Weather Rev.*, **134**, 2318–2341.

Houze, R. A., Jr, 2014: *Cloud dynamics* (2nd ed.). Academic Press, 496 pp.

Iguchi, T., T. Matsui, A. Tokay, P. Kollias, and W. K. Tao, 2012: Two distinct modes in one-day rainfall event during MC3E field campaign:

Analyses of disdrometer observations and WRF-SBM simulation. *Geophys. Res. Lett.*, **39**, 1–7.

Iguchi, T., T. Nakajima, A. P. Khain, K. Saito, T. Takemura, H. Okamoto, T. Nishizawa, and W. K. Tao, 2012: Evaluation of cloud microphysics in JMA-NHM simulations using bin or bulk microphysical schemes through comparison with cloud radar observations. *J. Atmos. Sci.*, **69**, 2566–2586.

Jaffrain, J., and A. Berne, 2011: Experimental quantification of the sampling uncertainty associated with measurements from PARSIVEL disdrometers. *J. Hydrometeorol.*, **12**, 352–370.

Janapati, J., B. K. Seela, M. V. Reddy, K. K. Reddy, P.-L. Lin, T. N. Rao, and C.-Y. Liu, 2017: A study on raindrop size distribution variability in before and after landfall precipitations of tropical cyclones observed over southern India. *J. Atmos. Solar-Terrestrial Phys.*, **159**, 23–40.

Jang, J., Y. H. Lee, and S. Joo, 2017: An intercomparison study between optimization algorithms for parameter estimation of microphysics in Unified model: Micro-genetic algorithm and Harmony search algorithm. *J. Korean Inst. Intell. Syst.*, **27**, 79–87.

Jiménez, P. A., J. Dudhia, J. F. González-Rouco, J. Navarro, J. P. Montávez, and E. García-Bustamante, 2012: A revised scheme for the WRF surface layer formulation. *Mon. Weather Rev.*, **140**, 898–918.

Jin, H. G., and J. J. Baik, 2023: Do Double-Moment Microphysics Schemes Make Reliable Predictions on the Raindrop Number Concentration?: A Squall-Line Case Study. *J. Geophys. Res. Atmos.*, **128**, e2022JD038394.

Jwa, M., H.-G. Jin, J. Lee, S. Moon, and J.-J. Baik, 2021: Characteristics of raindrop size distribution in Seoul, South Korea according to rain and weather types. *Asia-Pacific J. Atmos. Sci.*, **57**, 605–617.

Kain, J. S., 2004: The Kain–Fritsch convective parameterization: An update. *J. Appl. Meteorol.*, **43**, 170–181.

Kathiravelu, G., T. Lucke, and P. Nichols, 2016: Rain drop measurement techniques: A review. *Water*, **8,** 29.

Khain, A., M. Ovtchinnikov, M. Pinsky, A. Pokrovsky, and H. Krugliak, 2000: Notes on the state-of-the-art numerical modeling of cloud microphysics. *Atmos. Res.*, **55**, 159–224.

Khain, A., D. Rosenfeld, A. Pokrovsky, U. Blahak, and A. Ryzhkov, 2011: The role of CCN in precipitation and hail in a mid-latitude storm as seen in simulations using a spectral (bin) microphysics model in a 2D dynamic frame. *Atmos. Res.*, **99**, 129–146.

Khain, A. P., K. D. Beheng, A. Heymsfield, A. Korolev, S. O. Krichak, Z. Levin, M. Pinsky, V. Phillips, T. Prabhakaran, and A. Teller, 2015: Representation of microphysical processes in cloud-resolving models: Spectral (bin) microphysics versus bulk parameterization. *Rev. Geophys.*, **53**, 247–322.

Khairoutdinov, M. F., and Y. L. Kogan, 1999: A large eddy simulation model with explicit microphysics: Validation against aircraft observations of a stratocumulus-topped boundary layer. *J. Atmos. Sci.*, **56**, 2115–2131.

Kim, H.-J., K.-O. Lee, C.-H. You, H. Uyeda, and D.-I. Lee, 2019: Microphysical characteristics of a convective precipitation system observed on July 04, 2012, over Mt. Halla in South Korea. *Atmos. Res.*, **222**, 74–87.

Kim, H.-J., W. Jung, S.-H. Suh, D.-I. Lee, and C.-H. You, 2022: The characteristics of raindrop size distribution at windward and leeward side over mountain area. *Remote Sens.*, **14**, 2419.

Lee, H., and J.-J. Baik, 2016: Effects of turbulence-induced collision enhancement on heavy precipitation: The 21 September 2010 case over the Korean Peninsula. *J. Geophys. Res Atmos.*, **121**, 12319–12342.

Lee, H., and J.-J. Baik, 2018: A comparative study of bin and bulk cloud microphysics schemes in simulating a heavy precipitation case. *Atmosphere*, **9**, 475

Lee, M.-T., P.-L. Lin, W.-Y. Chang, B. K. Seela, and J. Janapati, 2019:

Microphysical characteristics and types of precipitation for different seasons over north Taiwan. *J. Meteorol. Soc. Japan*, **97**, 841–865.

Lei, H., J. Guo, D. Chen, and J. Yang, 2020: Systematic bias in the prediction of warm-rain hydrometeors in the WDM6 microphysics scheme and modifications. *J. Geophys. Res. Atmos.*, **125**, e2019JD030756.

Leinonen, J., D. Moisseev, M. Leskinen, and W. A. Petersen, 2012: A climatology of disdrometer measurements of rainfall in Finland over five years with implications for global radar observations. *J. Appl. Meteorol. Climatol.*, **51**, 392–404.

Lim, K. S. S., and S. Y. Hong, 2010: Development of an effective double-moment cloud microphysics scheme with prognostic cloud condensation nuclei (CCN) for weather and climate models. *Mon. Weather Rev.*, **138**, 1587–1612.

Lim, Y. S., J. K. Kim, J. W. Kim, B. I. Park, and M. S. Kim, 2015: Analysis of the relationship between the kinetic energy and intensity of rainfall in Daejeon, Korea. *Quat. Int.*, **384**, 107–117.

Lin, L., H. Yuan, X. Bao, W. Chen, S. Zhang, and F. Xu, 2022: Evaluation of the raindrop size distribution representation of microphysics schemes in typhoon lekima using disdrometer network observations. *Atmos. Res.*, **278**, 106346.

Loh, J. L., D.-I. Lee, and C.-H. You, 2019: Inter-comparison of DSDs between

Jincheon and Miryang at South Korea. *Atmos. Res.*, **227**, 52–65.

Lynn, B., and A. Khain, 2007: Utilization of spectral bin microphysics and bulk parameterization schemes to simulate the cloud structure and precipitation in a mesoscale rain event. *J. Geophys. Res. Atmos.*, **112**, D22205.

Ma, Y., G. Ni, C. V Chandra, F. Tian, and H. Chen, 2019: Statistical characteristics of raindrop size distribution during rainy seasons in the Beijing urban area and implications for radar rainfall estimation. *Hydrol. Earth Syst. Sci.*, **23**, 4153–4170.

Marshall, J. S., and W. M. Palmer, 1948: The distribution of raindrops with size. *J. Meteorol.*, **5**, 165–166.

Marshall, J. S., W. Hitschfeld, K. L. S. Gunn, 1955: Advances in radar weather. *Adv. Geophys.*, **2**, 1–56

Milbrandt, J. A., and M. K. Yau, 2005: A multimoment bulk microphysics parameterization. Part II: A proposed three-moment closure and scheme description. *J. Atmos. Sci.*, **62**, 3065–3081.

Mlawer, E. J., S. J. Taubman, P. D. Brown, M. J. Iacono, and S. A. Clough, 1997: Radiative transfer for inhomogeneous atmospheres: RRTM, a validated correlated-k model for the longwave. *J. Geophys. Res.*, **102**, 16663–16682.

Morrison, H., J. A. Curry, and V. I. Khvorostyanov, 2005: A new double-moment microphysics parameterization for application in cloud and climate models. Part I: Description. *J. Atmos. Sci.* **62**, 1665–1677.

Morrison, H., and J. A. Milbrandt, 2015: Parameterization of cloud microphysics based on the prediction of bulk ice particle properties. Part I: Scheme description and idealized tests. *J. Atmos. Sci.*, **72**, 287–311.

Morrison, H., P. Lawson, and K. K. Chandrakar, 2022: Observed and bin model simulated evolution of drop size distributions in high-based cumulus congestus over the United Arab Emirates. *J. Geophys. Res. Atmos.*, **127**, e2021JD035711.

Murata, F., T. Terao, K. Chakravarty, H. J. Syiemlieh, and L. Cajee, 2020: Characteristics of orographic rain drop-size distribution at Cherrapunji, Northeast India. *Atmosphere*, **11**, 777.

Niu, S., X. Jia, J. Sang, X. Liu, C. Lu, and Y. Liu, 2010: Distributions of raindrop sizes and fall velocities in a semiarid plateau climate: Convective versus stratiform rains. *J. Appl. Meteorol. Climatol.*, **49**, 632–645.

Nzeukou, A., H. Sauvageot, A. D. Ochou, and C. M. F. Kebe, 2004: Raindrop size distribution and radar parameters at Cape Verde. *J. Appl. Meteorol.*, **43**, 90–105.

Pan, Y., M. Xue, and G. Ge, 2016: Incorporating diagnosed intercept parameters and the graupel category within the ARPS cloud analysis system for the initialization of double-moment microphysics: Testing with a squall line over South China. *Mon. Weather Rev.*, **144**, 371–392.

Park, S.-G., H.-L. Kim, Y.-W. Ham, and S.-H. Jung, 2017: Comparative Evaluation of the OTT PARSIVEL^2 Using a Collocated Two-Dimensional Video Disdrometer. *J. Atmos. Ocean. Technol.*, **34**, 2059–2082.

Paukert, M., J. Fan, P. J. Rasch, H. Morrison, J. A. Milbrandt, J. Shpund, and A. Khain, 2019: Three-Moment Representation of Rain in a Bulk Microphysics Model. *J. Adv. Model Earth Syst.*, **11**, 257–277.

Radhakrishna, B., and T. N. Rao, 2009b: Multipeak raindrop size distribution observed by UHF/VHF wind profilers during the passage of a mesoscale convective system. *Mon. Weather Rev.*, **137**, 976–990.

Raupach, T. H., M. Thurai, V. N. Bringi, and A. Berne, 2019: Reconstructing the drizzle mode of the raindrop size distribution using double-moment normalization. *J. Appl. Meteorol. Climatol.*, **58**, 145–164.

Rosenfeld, D., and C. W. Ulbrich, 2003: Cloud microphysical properties, processes, and rainfall estimation opportunities. Radar and atmospheric science: *A collection of essays in honor of David Atlas*. American Meteorological Society, 237–258.

Sauvageot, H., and M. Koffi, 2000: Multimodal raindrop size distributions. *J. Atmos. Sci.*, **57**, 2480–2492.

Seela, B. K., J. Janapati, P. Lin, K. K. Reddy, R. Shirooka, and P. K. Wang, 2017: A comparison study of summer season raindrop size distribution between Palau and Taiwan, two islands in western Pacific. *J. Geophys. Res. Atmos.*, **122**, 11787–11805.

Seela, B. K., J. Janapati, P.-L. Lin, P. K. Wang, and M.-T. Lee, 2018: Raindrop size distribution characteristics of summer and winter season rainfall over north Taiwan. *J. Geophys. Res. Atmos.*, **123**, 11602–11624.

Shpund, J., A. Khain, B. Lynn, J. Fan, B. Han, A. Ryzhkov, J. Snyder, J. Dudhia, D. Gill, 2019: Simulating a ,mesoscale convective system using WRF with a new spectral bin microphysics: 1: Hail vs graupel. *J. Geophys. Res. Atmos.*, **124**, 14072–14101.

Skamarock, W. C., J. B. Klemp, J. Dudhia, D. O. Gill, Z. Liu, J. Berner, W. Wang, J. G. Powers, M. G. Duda, D. M. Barker, and X.-Y. Huang, 2019: A description of the advanced research WRF model version 4 (NCAR technical notes NCAR/TN-556+STR, 145 pp.). Boulder, CO: National Center for Atmospheric Research.

Steiner, M., R. A. Houze Jr, and S. E. Yuter, 1995: Climatological characterization of three-dimensional storm structure from operational radar and rain gauge data. *J. Appl. Meteorol. Climatol.*,

34, 1978–2007.

Suh, S.-H., C.-H. You, and D.-I. Lee, 2016: Climatological characteristics of raindrop size distributions in Busan, Republic of Korea. *Hydrol. Earth Syst. Sci.*, **20**, 193–207.

Suh, S.-H., H.-J. Kim, D.-I. Lee, and T.-H. Kim, 2021: Geographical characteristics of raindrop size distribution in the southern parts of South Korea. *J. Appl. Meteorol. Climatol.*, **60**, 157–169.

Testud, J., S. Oury, R. A. Black, P. Amayenc, and X. Dou, 2001: The concept of “normalized” distribution to describe raindrop spectra: A tool for cloud physics and cloud remote sensing. *J. Appl. Meteorol.*, **40**, 1118–1140.

Tewari, M., F. Chen, W. Wang, J. Dudhia, M. A. LeMone, K. Mitchell, M. Ek, G. Gayno, J. Wegiel, and R. H. Cuenca, 2004: Implementation and verification of the unified Noah land surface model in the WRF model, in: 20th Conference on Weather Analysis and Forecasting/16th Conference on Numerical Weather Prediction. American Meteorological Society, Seattle, WA.

Thompson, E. J., S. A. Rutledge, B. Dolan, and M. Thurai, 2015: Drop size distributions and radar observations of convective and stratiform rain over the equatorial Indian and west Pacific Oceans. *J. Atmos. Sci.*, **72**, 4091–4125.

Thompson, G., P. R. Field, R. M. Rasmussen, and W. D. Hall, 2008: Explicit forecasts of winter precipitation using an improved bulk microphysics scheme. Part II: Implementation of a new snow parameterization. *Mon. Weather Rev.*, **136**, 5095–5115.

Thurai, M., P. N. Gatlin, and V. N. Bringi, 2016: Separating stratiform and convective rain types based on the drop size distribution characteristics using 2D video disdrometer data. *Atmos. Res.*, **169**, 416–423.

Thurai, M., P. Gatlin, V. N. Bringi, W. Petersen, P. Kennedy, B. Notaroš, and L. Carey, 2017: Toward completing the raindrop size spectrum: Case studies involving 2D-video disdrometer, droplet spectrometer, and polarimetric radar measurements. *J. Appl. Meteorol. Climatol.*, **56**, 877–896.

Tokay, A., and D. A. Short, 1996: Evidence from tropical raindrop spectra of the origin of rain from stratiform versus convective clouds. *J. Appl. Meteorol.*, **35**, 355–371.

Tokay, A., D. B. Wolff, and W. A. Petersen, 2014: Evaluation of the new version of the laser-optical disdrometer, OTT Parsivel^2. *J. Atmos. Ocean. Technol.* **31**, 1276–1288.

Twomey, S., 1977: Influence of pollution on shortwave albedo of clouds. *J. Atmos. Sci.*, **34**, 1149–1152.

Uijlenhoet, R., M. Steiner, and J. A. Smith, 2003: Variability of raindrop size distributions in a squall line and implications for radar rainfall estimation. *J. Hydrometeorol.*, **4**, 43–61.

Ulbrich, C. W., 1983: Natural variations in the analytical form of the raindrop size distribution. *J. Clim. Appl. Meteorol.*, **22**, 1764–1775.

Wainwright, C. E., D. T. Dawson, M. Xue, and G. Zhang, 2014: Diagnosing the intercept parameters of the exponential drop size distributions in a single-moment microphysics scheme and impact on supercell storm simulations. *J. Appl. Meteorol. Climatol.*, **53**, 2072–2090.

Waldvogel, A., 1974: The N_0 jump of raindrop spectra. *J. Atmos. Sci.* **31**, 1067–1078.

Walters, D., A. J. Baran, I. Boutle, M. Brooks, P. Earnshaw, J. Edwards, K. Furtado, P. Hill, A. Lock, J. Manners, C. Morcrette, J. Mulcahy, C. Sanchez, C. Smith, R. Stratton, W. Tennant, L. Tomassini, K. Van Weverberg, S. Vosper, M. Willett, J. Browse, A. Bushell, K. Carslaw, M. Dalvi, R. Essery, N. Gedney, S. Hardiman, B. Johnson, C. Johnson, A. Jones, C. Jones, G. Mann, S. Milton, H. Rumbold, A. Sellar, M. Ujiie, M. Whitall, K. Williams, and M. Zerroukat, 2019: The Met Office Unified Model Global Atmosphere 7.0/7.1 and JULES Global Land 7.0 configurations. *Geosci. Model Dev.*, **12**, 1909–1963.

Wang, M., K. Zhao, Y. Pan, and M. Xue, 2020: Evaluation of simulated drop size distributions and microphysical processes using polarimetric radar observations for landfalling Typhoon Matmo (2014). *J. Geophys. Res. Atmos.*, **125**, e2019JD031527.

Wen, L., K. Zhao, G. Zhang, M. Xue, B. Zhou, S. Liu, and X. Chen, 2016: Statistical characteristics of raindrop size distributions observed in East China during the Asian summer monsoon season using 2-D video disdrometer and Micro Rain Radar data. *J. Geophys. Res.*, **121**, 2265–2282.

Witte, M. K., P. Y. Chuang, O. Ayala, L. P. Wang, and G. Feingold, 2019: Comparison of observed and simulated drop size distributions from large-eddy simulations with bin microphysics. *Mon. Weather Rev.*, **147**, 477–493.

Wu, Z., Y. Zhang, L. Zhang, H. Lei, Y. Xie, L. Wen, and J. Yang, 2019: Characteristics of summer season raindrop size distribution in three typical regions of western Pacific. *J. Geophys. Res. Atmos.*, **124**, 4054–4073.

Yang, Q., Q. Dai, D. Han, Y. Chen, and S. Zhang, 2019: Sensitivity analysis of raindrop size distribution parameterizations in WRF rainfall simulation. *Atmos. Res.*, **228**, 1–13.

You, C.-H., and D.-I. Lee, 2015: Decadal variation in raindrop size distributions in Busan, Korea. *Adv. Meteorol.*, **2015**, 329327.

You, C.-H., D.-I. Lee, M.-Y. Kang, and H.-J. Kim, 2016: Classification of rain types using drop size distributions and polarimetric radar: Case study of a 2014 flooding event in Korea. *Atmos. Res.*, **181**, 211–219.

Zea, L. R., S. W. Nesbitt, A. Ladino, J. C. Hardin, and A. Varble, 2021: Raindrop size spectrum in deep convective regions of the americas. *Atmosphere*, **12**, 979.

Zhang, A., J. Hu, S. Chen, D. Hu, Z. Liang, C. Huang, L. Xiao, C. Min, and H. Li, 2019: Statistical characteristics of raindrop size distribution in the monsoon season observed in southern China. *Remote Sens.*, **11**, 432.

Zhang, G., J. Vivekanandan, and E. Brandes, 2001: A method for estimating rain rate and drop size distribution from polarimetric radar measurements. *IEEE Trans. Geosci. Remote Sens.*, **39**, 830–841.

Zhang, G., J. Vivekanandan, E. A. Brandes, R. Meneghini, and T. Kozu, 2003: The shape-slope relation in observed gamma raindrop size distributions: Statistical error or useful information? *J. Atmos. Ocean. Technol.*, **20**, 1106–1119.

Zhang, G., M. Xue, Q. Cao, and D. Dawson, 2008: Diagnosing the intercept parameter for exponential raindrop size distribution based on video disdrometer observations: Model development. *J. Appl. Meteorol.*

Climatol., **47**, 2983–2992.

초 록

2018년 7월 25일부터 2021년 7월 31일까지 관측된 우적계 자료를 이용하여 우리나라 세 도시(서울, 춘천, 진천)에서 나타난 빗방울 크기 분포(RSD) 특징의 지역적 차이를 조사하였다. 세 도시 중 가장 인구가 적고 가장 남쪽에 위치한 도시인 진천은 가장 작은 평균 강수 강도와 약한 강수의 상대적으로 높은 빈도로 특징된다. 이러한 강수 특성은 세 도시 중 가장 작은 질량 가중 평균 지름 D_{m}과 가장 큰 일반화된 절편 모수의 로그값 $\log_{10}N_{\mathrm{w}}$과 관련된다. 이와는 대조적으로 분지에 위치한 중간 규모의 도시인 춘천은 가장 큰 평균 강수 강도와 강한 강수의 상대적으로 높은 빈도로 특징되며 이는 가장 큰 D_{m}과 가장 작은 $\log_{10}N_{\mathrm{w}}$과 관련된다. 진천(춘천)의 상대적으로 작은(큰) 대류 가용 위치 에너지, 낮은(높은) 운정 고도, 높은(낮은) 운저 고도가 두 지점에서 나타난 RSD 특성의 차이에 대한 원인으로 제시되었다. 가장 인구가 많은 도시인 서울은 중간 크기의 강수 강도로 특징되는데 이는 중간 크기의 D_{m}과 $\log_{10}N_{\mathrm{w}}$와 관련된다. 서울에서 극한 강수 사건의 빈도가 가장 많이 나타나며 매우 강한 강수에 대해 상대적으로 큰 D_{m}이 나타났는데 이는 큰 대류 가용 위치 에너지가 가장 자주 발생한 특징과 관련된다.

지상 또는 항공 우적계로부터 관측된 RSD는 구름과 강수의 특성을 이해하기 위해 널리 이용되어 왔다. 그러나 강수 예측 향상을 위해서 RSD의 변동성은 보다 더 연구되고 적절히 고려되어야

할 필요가 있다. 본 연구에서는 우적계 자료를 이용하여 지수 분포 RSD의 절편 모수(N_0)에 대한 진단 관계식을 강수 유형별로 유도하고 그 진단 관계식이 강수 예측에 미친 영향을 조사하였다. 우리나라의 네 지점에서 관측된 우적계 자료는 N_0의 시공간적인 변동성을 보여줬다. 선행 연구에서 제안된 세 가지 다른 유도 방법을 통해 진단 관계식을 유도하였고 관측된 N_0을 가장 잘 재현한 진단 관계식이 선정되었다. 이 진단 관계식은 WRF 모형의 단일 모멘트 방안 중 하나인 WSM6 방안에 접목되었고 우리나라 여름철 강수 사례에 대한 실험을 통해 그 영향이 조사되었다. 상수인 N_0을 사용한 기존 WSM6 방안을 적용한 실험(WSM6-O)과 비교하여, 가장 낮은 고도의 우적 함량을 이용한 진단 관계식을 통해 N_0을 진단한 실험(WSM6-L)은 보다 나은 강수 예측을 보였다. WSM6-L 실험은 N_0의 변동성을 재현했으며 평균적으로 WSM6-O 실험에서 처방된 값보다 작은 N_0을 예측했는데 이는 관측과 어느 정도 일치한 결과였다. WSM6-L 실험의 보다 작은 N_0은 구름 물방울의 결착과 얼음상 수물질의 융해에 의해 빗방울 생성을 감소시켰고 이는 빗방울의 혼합비를 감소시켰다.

Bin 미세물리 방안은 우적계 관측과의 비교를 통해 직접 평가될 수 있는 RSD를 예단한다. 이러한 평가는 bin 미세물리 방안에 의해 모의된 구름 미세물리의 신뢰성에 대한 함의를 제공할 수 있다. 본 연구에서는 우리나라를 지난 온대 저기압과 관련된 강수 사례의 RSD를 bin 미세물리 방안을 이용하여 모의하였고 이를 지상의 우적계를 통해 관측된 RSD와 비교하였다. 모의된 평균 RSD는 관측과 전반적으로 일치했으며 특히 중간 지름 범위에서 잘 일치했

다. 큰 크기의 지름 범위와 작은 크기의 지름 범위에서 뚜렷한 과대 추정이 나타났는데 이는 각각 층운형 강수가 지배적인 기간과 대류형 강수가 크게 관여한 기간에서 기인한 편향성에 의한 것이었다. 층운형 강수가 지배적인 기간에는 눈의 융해가 RSD에 가장 많이 기여했다. 이 기간에 발생한 큰 지름 범위에서의 과대 추정은 상층에서 과도하게 활발한 얼음-얼음 포착 과정과 연관되며 이는 관측에서는 보이지 않던 3.3 mm 지름에서의 극댓값을 생성했다. 대류형 강수가 관여한 기간에는 충돌-병합이 RSD에 가장 많이 기여했다. 작은 지름 범위에서의 과대 추정과 큰 지름 범위에서의 과소 추정은 빗방울간 충돌에 의한 성장이 현실보다 약하게 모의되었음을 시사한다. 본 연구는 bin 미세물리 방안을 이용하여 모의한 RSD가 몇몇 미세물리 과정을 잘못 반영한 것에서 기인한 구조적인 편향성을 가지고 있다는 것을 보였다.

두 다른 강수 유형(층운형과 대류형 강수)에 대해 에어로졸이 강수와 RSD에 미친 영향을 조사하였다. 초기 에어로졸 수농도(N_a)를 다르게 한 5개의 실험이 수행되었다. 층운형 강수와 대류형 강수 모두에서 N_a의 증가는 핵화 과정을 강화시켰고 이는 구름 물방울의 수는 증가시키고 평균 크기는 감소시켰다. 이는 결과적으로 결착, 상고대화, 응결 과정을 강화시켰다. 대류형 강수의 경우, N_a 증가로 강화된 응결 과정은 증가된 잠열 방출을 통해 더 강한 상승류를 발생시켰고 더 많은 수증기를 소모하여 상층을 더 건조하게 만들었다. 건조해진 상층으로 인해 Wegener-Bergeron-Findeisen 과정이 더 활발해졌다. 얼음 관련 미세물리 과정이 활발하게 발생했음에도 낮은 융해율로 인해 얼음 관련 미세물리 과정의 강수에 대한

기여도는 상대적으로 약했다. 결과적으로 보다 활발한 결착 및 상고대화 과정이 대류형 강수의 강수율과 중간 지름 범위의 빗방울 수농도를 증가시켰다. 층운형 강수에서는 융해 과정이 결착 및 상고대화 과정과 비슷하게 발생했다. 이는 대류형 강수 지역에서 이류된 많은 양의 눈에 의한 영향에 의한 것으로 나타났다. 층운형 강수에서의 보다 활발한 융해 과정은 결과적으로 결착 및 상고대화 과정과 함께 층운형 강수의 강수율을 증가시켰고 큰 지름 범위에서의 빗방울 수농도를 증가시켰다.

주요어: 빗방울 크기 분포, 우적계, bulk 구름 미세물리 방안, bin 구름 미세물리 방안, 강수, 에어로졸-구름-강수 상호작용

학 번: 2017-20135